Advanced Molecular Modelling Techniques To Determine Structures And Reaction Mechanisms Of Catalytic Processes At The Atomic Level

Cameron Beevers

January 2021

Acknowledgements

I would like to acknowledge the support of the Supercomputing Wales project, which is part-funded by the European Regional Development Fund (ERDF) via Welsh Government. Via our membership of the UK's HECMaterials Chemistry Consortium, which is funded by EPSRC (EP/L000202), this work also used the UK Materials and Molecular Modelling Hub for computational resources, which is partially funded by EPSRC (EP/P020194).

I would like to thank all those that have provided support, friendship, guidance, and advice during the course of these projects. I would like to acknowledge all the colleagues and collaborators who have provided support, advice, and guidance, with a special mention of Drs Ali Nasrallah, Julien Engel, Matthew Quesne, Samantha Francis, Andrew Logsdail, and Peter Knowles. I would also like to thank my parents and grandmother, all of whom have provided support and shown an enormous tolerance for my endless words upon the nuances of molecular symmetry and quantum chemistry.

I would especially like to express my gratitude to my supervisor Dr Alberto Roldan, whose guidance, kindness, support, and training have improved me as an academic.

Finally, my greatest gratitude goes to Grace Owen, her unwavering faith, kindness, and support made all of this possible.

Contents

Publications

1) **DFT-assisted Spectroscopic Studies on the Coordination of Small Ligands to Palladium: From Isolated Ions to Nanoparticles** — S. Campisi, C. Beevers, A. Nasrallah, C. R. A. Catlow, C. E. Chan-Thaw, M. Manzoli, N. Dimitratos, D. J. Willock, A. Roldan and A. Villa, *J. Phys. Chem. C*, 2020, DOI:10.1021/acs.jpcc.9b09791.

Summary

This thesis focuses upon an examination of small nanoparticles of particular relevance to catalytic processes. The first chapter provides an introduction to the topics discussed throughout this work. The second chapter contains a discussion of the theoretical underpinnings of the computational chemistry techniques that have been applied throughout the work.

An examination of the modelling of palladium nanoparticle seed solutions using atom-centred density functional theory and time-dependent density functional theory is presented within the third chapter. The fourth chapter introduces a case study upon the electronic properties of Au_{19} which utilises various descriptor functions to examine and characterise the electronic structure of Au_{19} and proposes a machine-learning derived method for examining and approximating tensor properties, with a particular application demonstrated in the calculation of the elasticity of Au_{19}.

The work in the fifth chapter introduces a range of novel methodologies based upon a unique approach to continuous symmetry measurement and a software code developed to implement these measurement techniques. This symmetry measurement is then applied to the characterisation of nanoparticle structures, as well as a diverse range of molecular species.

Chapter six analyses the work as a whole and draws conclusions based upon the results of each section.

Chapter 1

Introduction

This thesis focuses upon characterisation and the development of investigative methodologies, so as to better understand less examined aspects of the chemistry of small metal nanoparticles and their precursors. These species in particular are of interest as they are commonly recognised for their diverse utility and high reactivity and catalytic activity. Small metal nano-clusters exhibit properties that are significantly different to the bulk metals; their properties vary significantly with changes in size or morphology. Understanding the behaviour and structure of these small particles, as well as developing methodologies for their theoretical characterisation and examination, provides significant insight into both understanding their properties and how they can best be stabilised or synthesised.

The unique characteristics of small metal nanoparticles are often attributed to their band structures, which can form discrete pseudo-orbitals and allow for nanoparticles to behave as super-atoms.[1–3] In contrast to the continuous metallic band structure of large particles and bulk metals, the super-atom model of cluster cores predicts that the delocalised orbitals form supershells with stable closed subshells that mimic the electronic structure of individual atoms.[2–5] As is described by the work of Bakr *et al.* superatom clusters can exhibit reactivities and interactions that are analogous to other elements or clusters.[6] The super-atom electronic structure also causes small noble metal nanoparticles to significantly change behaviour based upon ligands, solvent environment, and size.[7–9]

As well as the characteristics of super-atoms, nanoparticles can exhibit quantum size effects. These can cause the properties of small particles to deviate significantly

from the expected trend in properties towards that of the bulk material as particle size is increased.[4,7,10] As the bulk material is more energetically favourable than the equivalent nanoparticle systems, processes of growth, attrition, and coalescence cause a gradual increase in the average size of nanoparticles.[11] This causes mono-dispersed nanoparticle materials to be difficult to synthesise and stabilise, as the processes causing the formation of nanoparticles also lead to further growth beyond the target size.

1.1 Palladium precursors and seed solution

The utility in examining the synthesis and growth of small nanoparticles is encapsulated in the work of Jana and Pal, which demonstrates that palladium nanoparticles during the growth phase show increased catalytic activity in comparison to the stabilised final particles when applied to the reduction of dye molecules.[12–14] As certain sizes of particle may show increased activity for certain reactions, the issue of stabilising catalytically active particles of a specific size is a common problem within nanoparticle synthesis.[15] An example of this is shown in the work of Rahaman *et al*, who demonstrated the size dependent activity of palladium nanoparticles in the reduction of carbon dioxide to formate.[16] Their work showed significant differences in the rate of reduction which was determined by the size of the nanoparticles that were formed. This required them to carefully control the capping agent concentration and reaction temperature in order to produce relatively monodispersed Pd nanoparticles. However, these were still larger cluster sizes, ranging from 3.8—10.7 nm. For applications where smaller clusters sizes are more active, it is essential to develop an understanding of the synthesis and seeding of nanoparticles. Chapter 3 of this thesis presents a collaborative theoretical and experimental investigation that seeks to characterise a simple palladium nanoparticle seed solution and examine the interaction of a ligand that goes on to become a capping agent of the formed nanoparticle system. Although this was not a mechanistic study, by examining the reaction conditions and characterising the species present in the seed solutions, this work provides a foundation upon which future mechanistic studies of palladium nanoparticle seeding can be based.

Palladium nanoparticles are frequently utilised within catalysis and have been found to have applications in such reactions as the oxidation of aliphatic hydrocarbons, hy-

drogenation of alkynes, and in carbon—carbon coupling reactions.[17–20] The homogeneous Pd(0) nanoparticles are often readily formed by the reduction of Pd(II) and are well-stabilised by a diverse range of capping agents.[17] Nanocrystalline palladium shows strong interactions with capping agents that contain hetero-atoms, with particularly strong stabilisation being provided by sulphur and nitrogen containing species.[21] Bulk palladium favours an fcc crystal structure, and this is found to be reflected in the nanoparticle structure where the Pd(100) and Pd(111) surfaces of the fcc lattice are the favoured surfaces exposed within nanoparticle structure.[22] The morphology of palladium nanostructures has been found to be significantly influenced by the environmental factors within the synthesis reaction mixture.[22,23]

1.2 Small gold particle characterisation

As well as examining the seeding of nanoparticle systems, characterisation of the properties of small nanoparticles is also useful in understanding how these species behave in realistic environments. To this end, chapter 4 of this thesis presents a comparative examination of the bonding in Au_6, a molecular gold species, and Au_{19}, a small nanoparticle. Bulk gold exhibits a face-centred cubic crystal (fcc) packing of the ideal unit cell, and larger ideal nanostructures conform to this crystal structure, with the three common geometries for larger gold nanoparticles being truncated decahedra, icosahedra, and cuboctohedra.[24] In contrast to the crystalline structure of large gold clusters, small gold clusters and molecular gold species, particularly Au_N where $6 < N < 19$, show a unique divergence from the clusters of other noble or coinage metals.[4]

Small gold nanoparticles have particularly unusual characteristics due to the relativistic contraction of the 6S orbital.[4] This contraction results in shorter inter-atomic distances and a greater amount of orbital overlap than is found in the other metals, causing planar structures to be more stable for small gold species, rather than the 3-dimensional geometries adopted by clusters of the equivalent atom number for similar metals such as Ag, Cu, Pd, and Pt.[4] The relativistic contraction of the 6S orbital also contributes an electron volt to the electron affinity of Au, increasing it far above both Ag and Cu.[25–27] For these reasons, relativistic effects must be included in any theoretical models of gold chemistry.[28]

To better examine the difference in properties between molecular gold and small nanoparticles, chapter 4 focusses upon examining bonding using Bader's atoms in molecules analysis and various descriptors that, in combination, develop a qualitative and quantitative characterisation of the differences in electronic structure between the molecular gold species and the nanoparticle. The descriptors utilised in this study were measures of electron and orbital localisation and kinetic energy, metallicity, and non-covalent interactions. These provide insight into the character of the electron density, the distribution of the band structure within the molecule and cluster, and also the surface properties and bonding.

As part of the discussion of properties and bonding, a methodology for the determination of nanoparticle elasticity will also be introduced. Nanoparticle elasticity has been shown to be a property of interest in the utilisation of nanoparticles within biological systems and also has utility in the examination of the behaviour of nanoparticles during adsorption upon surfaces, which is relevant to the synthesis of heterogeneous nanoscale materials upon support structures.[29–32] Small distortions in geometry due to external forces can be described through stress and elastic deformation.[32] However, calculation of elastic constants for inhomogeneous materials is a challenging process. This work proposes a methodology for determining nanoparticle elasticity through the application of a neural network as a non-linear solver and the determination of a local, bond-aligned elastic tensor.

1.3 Symmetry measurement

A novel approach to the characterisation methodology of continuous symmetry measurement is presented within chapter 5. The most relevant symmetries to chemistry are that of the point groups and space groups, with the latter used mainly for the purposes of describing periodic crystal symmetries. Point groups are defined as symmetries that keep a single point fixed, generally the origin of the system. Point groups are by definition discrete categorisations and provide significant utility; the character of a point group can be used to provide insight into the form of the wavefunction and observables derived thereof.[33,34]

Symmetry, as is relevant to chemical systems, is generally applied in terms of group theory and underpins much of quantum mechanics. Playing a role in everything from the Aufbau principle and the electronic wavefunction to the combination of orbitals and minimisation of crystal lattice energies.[35–37] Even the fundamental structure of the periodic table can be partially attributed to the symmetries within quantum mechanical systems.[38] However, despite the utility of this description, symmetry need not be categorised solely based upon theoretical perfect symmetries that rarely actually occur within this form in nature. Thermal vibrations, zero point energy, and imperfections are all aspects of chemical systems that can cause the perfect mathematical model of group theory to become an approximation or average of the observed reality.

In order to better characterise and describe real systems, continuous symmetry measures were created and these provide unique methods for capturing the symmetry of real systems, usually as a measure of deviation from perfect symmetry.[39–41] However, as will be discussed further in chapter 5, these measures are not without limitations. Although these measures are designed to increase comparability between geometries by inclusion of radial or size-dependent scaling factors, this introduces size dependencies that can lead to incorrect categorisations and incomparability between symmetrically similar geometries of different sizes. Two arguments against the scaling factors used in the two symmetry analysis algorithms are presented. This work seeks to provide a new measure of symmetry suitable for applications such as analysing the symmetry of nanoparticles and also several other novel methods of examining symmetry, which expand the field of symmetry measurement.

This also includes a mathematical framework for integrating the symmetries familiarly described group theory and the continuous symmetry that is found using continuous symmetry measures. This allows for both to be described under one consistent formalism and also provides a foundation for novel visualisations of symmetry.

1.4 Summary

The goals of the thesis are to provide an examination of the role of capping agents as ligands in the precursor molecules to nanoparticle synthesis, to examine the character of internal bonding in small gold nanoparticles through a comparative study of the

small nanoparticle Au_{19} and the molecular gold species Au_6, to develop a method for examining the elasticity of nanoparticles and other discrete inhomogeneous systems, and to develop a reliable symmetry analysis methodology that can be applied to the classification and examination of nanoparticle systems. The aim of this work is not just to provide analysis but to also develop novel methodologies for examining the properties of small metal nanoparticle species, with potential applications beyond the scope of this study.

Chapter 2

Methodologies

2.1 Quantum Mechanics

Quantum mechanics is a necessary tool in describing chemistry at a fundamental level. Electrons, which are the primary focus of chemistry, are quantum objects that cannot be correctly described by classical physics. The equation that underpins much of quantum mechanics is the Schrödinger equation, which applies the Hamiltonian operator, $\hat{H}$, to the wavefunction, ψ in order to evaluate the energy, E, of a system described by a specific wavefunction. Where $V(x)$ is the potential energy of the system:

$$\hat{H}\psi(x) = E\psi(x) \tag{2.1}$$

$$\text{Where: } \hat{H} = -\frac{\hbar^2}{2m}\frac{\partial^2}{\partial x^2} + V(x) \tag{2.2}$$

Quantum systems larger than single electron hydrogenic atoms present an example of the many body problem, for this reason the Schrödinger equation is unsolvable for many electron systems and so approximations are employed to allow for the approximate calculation of electronic structures relevant to chemistry. Of the available methodologies, the one selected for use in this study was density functional theory (DFT), as it provides relatively inexpensive and accurate results for chemical systems.

2.1.1 Density functional theory

Density functional theory avoids the issue of solving the Schrödinger equation by modelling electronic structure through electron density, which was demonstrated to provide access to all electronic properties by the works of Hohenberg and Kohn.[42] Ho-

henberg and Kohn used the concept of a homogeneous electron gas, jellium, and an inhomogeneous, slowly varying electron gas to provide the fundamental proofs that underpin density functional theory; these being namely that the energy of an electronic system is a unique functional of the density and that the functional that gives the ground state energy of the system does so only if the electron density is also in the ground state.[42,43] These theorems therefore allow for systems of electrons to be modelled by their densities, ρ, provided the universal functional, $F_{HK}[\rho]$, is known.

The form of the energy functional of the ground state density, $E_0[\rho_0(\vec{r})]$, is given by equation 2.3.

$$E_0[\rho_0(\vec{r})] = T[\rho_0(\vec{r})] + E_{Ne}[\rho_0(\vec{r})] + E_{ee}[\rho_0(\vec{r})] \tag{2.3}$$

Where the functionals T, E_{Ne}, and E_{ee} respectively determine the contributions to the total energy from the kinetic energy, the nucleus—electron interaction, and the electron—electron interaction. This again can be transformed such that the electron—electron interaction is expressed by application of the Hohenberg-Kohn universal functional to the density and the nuclear—electron interaction is given by the external potential, V_{Ne}, as shown in equation 2.4.

$$E_0[\rho_0(\vec{r})] = \int \rho_0(\vec{r}) V_{Ne} dr + F_{HK}[\rho_0(\vec{r})] \tag{2.4}$$

$$\text{Where: } F_{HK}[\rho_0(\vec{r})] = E_{ee}[\rho_0(\vec{r})] + T[\rho_0(\vec{r})] \tag{2.5}$$

From 2.5 it can be seen that the universal functional contains terms for the interactions between electrons and the kinetic energy and the external potential of the nuclear electron interactions, V_{Ne}, that shapes the ground-state electron density, ρ_0. However, despite our knowledge of this form of the universal function, the precise terms of E_{ee} and T are unknown.[43] As shown in equation 2.6, the contributions to the energy of electron—electron interactions can be further refined by including the classical components of the interaction, namely the Coulombic repulsion between electrons, leaving the unknown non-classical interaction term E_{ncl}.

$$E_{ee}[\rho(r)] = \frac{1}{2} \int \int \frac{\rho(\vec{r_1})\rho(\vec{r_2})}{\vec{r_{12}}} d\vec{r_1} d\vec{r_2} + E_{ncl}[\rho] \tag{2.6}$$

Where $\vec{r_{12}}$ is the displacement between $\vec{r_1}$ and $\vec{r_2}$.

However, whilst this refines the unknowns of the Schrödinger equation into a more precisely defined form, namely the terms $T[\rho]$ and $E_{ncl}[\rho]$, the functional presented in equation 2.6 remains unsolved and, as such, it took the work of Kohn and Sham on modelling non-interacting electron densities to address this problem.[44] Kohn and Sham describe a model for the non-interacting system where spin orbitals, ϕ, are given by Slater determinants and the energy is defined by the Kohn-Sham operator, $\hat{f^{ks}}$, as shown in equation 2.7.[45]

$$\hat{f^{ks}} = -\frac{1}{2}\nabla^2 + V_s(\vec{r}) \tag{2.7}$$

Where ∇^2 is the second derivative of 3-dimensional differential operator.

This elegantly provides a possible solution for the issues of density functional theory, as the Kohn-Sham operator may be selected such that the potential, V_s, causes the density of the non-interacting electronic system to match that of the ground state of the fully interacting electronic structure.[45] This further refines the functional form to include the majority of the contributions to kinetic energy, T_c and as such reduces the unknowns in the functional to a single term composed of the unknown aspects of the kinetic energy, T_u and the non-classical contributions to the electron—electron interaction. These energy contributions, defined as electron exchange and correlation, E_{XC}, are approximated in density functional theory through application of the density functional. The equation for the energy functional is, therefore, consistent with the form shown in equations 2.8 and 2.9.[43]

$$E[\rho_o] = T_c[\rho] + E_{XC}[\rho(\hat{r})] + E_{Ne}[\rho(\hat{r})] \tag{2.8}$$

$$\text{Where: } E_{XC}[\rho(\hat{r})] = T_u[\rho] + E_{ncl}[\rho] \tag{2.9}$$

2.1.1.1 Density Functionals

Incorporation of the exchange correlation term in density functional theory is achieved through application of exchange correlation functionals. This does, however, include the caveat that the lower bound of the energy is no-longer consistent with the ground state of the system, the variational principle established by Hohenberg-Kohn cannot be applied, as the ground state density may not be given by the lowest energy. The

simplest of the exchange correlation functionals are the Local Density Approximation, LDA, and Local Spin Density, LSD, which provide an approximation of exchange correlation based upon, respectively, the density and spin densities at a given point. However, LDA has been superseded by functionals that provide a better representation of exchange-correlation interactions. In particular, the generalised gradient approximation, GGA. GGA functionals, unlike LDA, do not account for only the density at a given point but also incorporate the gradient of the density, $\nabla\rho(\hat{r})$.[43]

GGA functionals build upon the LDA, which is treated as the first term of the Taylor expansion, and include a second term as part of the Gradient Expansion Approximation, GEA, as shown by equation 2.10.

$$E_{XC}^{GEA}[\rho_\alpha, \rho_\beta] = \int \rho\epsilon_{XC}(\rho_\alpha, \rho_\beta))d\hat{r} + \sum_{\sigma,\sigma'} \int C_{XC}^{\sigma,\sigma'} \frac{\nabla\rho_\sigma}{\rho_\sigma^{2/3}} \frac{\nabla\rho_{\sigma'}}{\rho_{\sigma'}^{2/3}} \tag{2.10}$$

The precise form of $C_{XC}^{\sigma,\sigma'}$ varies between GGA functionals and, due to this, it will not be discussed further here.[43,46] Other functional forms, such as meta-GGAs and Hybrid functionals are also frequently employed, for a full discussion upon functional forms the author recommends referral to the discussion of Jacob's Ladder of density functional theory by Perdew and Schmidt.[47]

Generalised Gradient Approximation (GGA) functionals exhibit a tendency for the overestimation of the covalent character of the metal-ligand bonds in transition metal complexes. However, when compared to hybrid functionals, GGAs can provide a more accurate description of the metal-metal bonding that is present in nanoparticle systems; although the hybrid functional PBE0 has been shown to provide a more accurate model of third row transition metal complexes.[48–50] PBE does exhibit an accuracy comparable to the hybrids B3LYP and TPSS and provides comparability with periodic methods that must be used for larger cluster sizes.[46,50] Due to these factors, unless stated otherwise, PBE was the functional of choice throughout this study.

2.1.2 Basis sets

Atom-centred Basis sets

As discussed above, the Kohn-Sham orbitals are best modelled through application of single electron atomic orbitals, however, as these prove computationally expensive for integration and manipulation, Gaussian Type Orbitals (GTOs), are commonly employed in atom-centred density functional theory, as these are computationally inexpensive. These GTOs approximate the form of Slater-Type orbitals (STOs) through the fitting of several Gaussian functions and are then combined such that they provide a representative electronic structure for each atom. These combined basis functions create a basis set, which are then combined to create the search space utilised in solving the molecular electronic structure within density functional theory.

A basis set becomes more costly to utilise as the number of functions and their extent, or diffuseness, increase. Throughout this study the selected basis sets were triple or quadruple zeta and contained functions that allow for the correct representation of valence electrons and electron polarisation. The ORCA implementation of the Karlsruhe basis sets were utilised for non-relativistic systems, those where relativistic effects are unnecessary to model, and the segmented all-electron relativistically contracted (SARC) basis sets were employed where this approximation would have introduced significant error.[51] The specific basis sets utilised in each section will be detailed in the computational methodologies of the respective chapter.

Plane-wave Basis sets

Plane-wave basis sets are utilised within periodic quantum chemistry codes to provide models of the electron density over systems of infinite extent. This can be achieved by defining a unit cell where repetition of the cell mimics the bulk or extended surface properties of the systems. The form of these functions is given as wave equation, ψ, as shown in equation 2.11

$$\psi(x) = Ae^{ikx} + Be^{-ikx} \tag{2.11}$$

Where A and B are the amplitudes of the real and imaginary components of the wave equation and k is the wave vector.

The physicality of the descriptions produced by plane wave basis sets is supported

by Bloch's theorem, which states that for any translation of a wavefunction, ψ, within an infinite system, there exists a phase factor that fulfils equation 2.12.

$$\psi(k, r + T) = e^{ikT}\psi(k, r) \tag{2.12}$$

where k is the wave-vector of inverse length and T is the transformation vector of the lattice. These basis functions are generally mathematically manipulated through the reciprocal or momentum space form, which is interconvertible with the position space representation through application of a Fourier transform. As such the size of these basis sets is restricted by an energy cutoff, where functions of a higher than necessary frequency are excluded from the calculation and instead their influence is represented by fixed pseudopotentials. In practice this occurs around nuclei and so these are represented by benchmarked pseudopotentials that provide a relatively accurate model of the core electronic structure.

The particular pseudopotentials used in this study are defined through the Projector Augmented Wave method (PAW). The PAW pseudopotentials incorporate the nodal region around the nuclei with a good accuracy but significantly decrease the computational cost in comparison to representing them through plane-wave basis functions. The PAW pseudopotentials used in this study were implemented within the Vienna Ab initio Simulation Package (VASP).[52–55]

The energy cut-offs that have been utilised in this study for the gold and palladium systems were benchmarked to determine stability of the energy of the system.

2.1.3 Relativistic Effects

For larger atoms, electronic behaviour cannot be sufficiently characterised through the Schrödinger equation alone but must also include relativistic effects that can only be described by the Dirac equation.[56] Manifestation of this effect include various macroscopic properties, for example the liquidity of mercury and the colouration of bulk gold, as well as many trends in properties found in the periodic table, such as the lanthanide contraction. However, as with the Schrödinger equation, the Dirac equation introduces a many-body problem that is unsolvable by current methods. In order to incorporate these effects within quantum mechanical simulations, various approxima-

tions have been developed that derive from the Dirac or relativistic Hamiltonian, with the two most popular being the Zero Order Regular Approximation (ZORA) and the Douglas-Kroll-Hess (DKH) approach.[57–60]

Throughout this study, whenever relativistic corrections have been necessary during atom-centred DFT calculations, the ZORA form of the Hamiltonian has been applied as is implemented within the ORCA software package.[51] This involves a transformation of the Dirac Hamiltonian to produce two effective Hamiltonians which are sufficient, when taken to the zeroth order, to be able to incorporate significant relativistic effects such as spin orbit coupling.[58]

The basis sets used with ZORA for elements smaller than Xe are the relativistically recontracted Karlsruhe triple zeta with valence and polarisation functions, ZORA-def2-TZVP, and the segmented all-electron relativistically contracted (SARC) ZORA basis set, SARC-ZORA-TZVP, is used for elements beyond Xe.[61] The use of these functionals and the relativistic corrections was benchmarked against the equivalent Karlsruhe basis set without relativistic recontraction and using Stuttgart-Dresden effective core potentials to reduce the cost of calculation.[62] However, for molecular gold systems the removal of relativistic effects was found to result in geometries that were inconsistent with the relativistically corrected calculations. For this reason the relativistic corrections and Hamiltonian approximations were employed for all atom-centred modelling of systems containing gold atoms. These were found to be consistent with the geometries determined by plane wave calculations and also to produce equivalent density of states.

2.1.4 Time Dependent - Density Functional Theory

Density functional theory, by definition, is a ground state methodology and cannot be reliably used to determine excited state electronic configurations. However, these excited states are necessary to characterise the electronic transitions that cause the formation of spectra in the ultra-violet—visible region of the electromagnetic spectrum.[63] Much like the relativistic corrections, this issue is resolved by changing the form of the Hamiltonian used to examine the energies of the systems. However, rather than approximations of the Dirac Hamiltonian, the time-dependent Hamiltonian must be employed, the form of which is shown in equation 2.13.[63]

$$\hat{H}(t) = \hat{T} + \hat{V}(t) + \hat{W} \tag{2.13}$$

Where the operators for kinetic energy, potential, and particle—particle interaction are given, respectively, by equations 2.14, 2.15, and 2.16.

$$\hat{T} = \sum_{j=1}^{N} -\frac{\nabla_j^2}{2} \tag{2.14}$$

$$\hat{V}(t) = \sum_{j=1}^{N} v(r_j, t) \tag{2.15}$$

$$\hat{W} = \frac{1}{2} \sum_{j,k;j\neq k}^{N} w(|r_j - rk|) \tag{2.16}$$

In order to obtain densities, a time-evolution operator $\hat{U}$ is also employed.

$$\Psi(t) = \hat{U}(t, t_0)\Psi(0) \tag{2.17}$$

The process of determining absorption frequencies using time dependent density functional theory is greatly simplified by linear response TD-DFT, as was utilised in this study. Linear response TD-DFT works upon the assumption that the excitation of the system does not cause significant deviation from the ground-state density.[63]

Rather than using the time-dependent Hamiltonian, a partitioned Hamiltonian, H_p, is employed. This is composed of a time-dependent external potential, $V_{ext(r,t)}$ and the time-independent Hamiltonian of the unperturbed system.

$$H_p = H_0 + V_{ext} \tag{2.18}$$

Where: $V_{ext} = \int \rho(r) V_{ext}(r, t) dr$

The time-dependent Schrodinger equation is then utilised, as shown in equation 2.19.

$$i\frac{d}{dt}|\Psi(t)_I\rangle = V_I|\Psi(t)_I\rangle \tag{2.19}$$

Where: $V_I = e^{iH_0t}V_{ext}e^{iH_0t} = \int dr \rho_I(r) V_{ext}(r, t)$ and $\rho_I(r) = e^{iH_0t}\rho(r)e^{iH_0t}$

A first order approximation is then employed to give equation 2.20.

$$|\Psi(t)_I\rangle \approx |\Psi(0)\rangle - i\int_{-\infty}^{0} dt' V_I(t')|\Psi(0)\rangle \tag{2.20}$$

The change in external potential can therefore be examined as a change in density from the ground-state, which allows for the absorbance spectra to be resolved from the ground state density. A response function, $\chi(r,t,r',t')$, is then given by equation 2.21 and can be used to calculate the change in an observable, $\delta\langle O\rangle$, as shown by equation 2.22.[63]

$$\chi(r,t,r',t') = \lim_{\eta\to 0} -i\theta(t-t')\langle\Psi(0)|[\rho_I(r,0),\rho_I(r',t'-t)]\,|\Psi(0)\rangle e^{\eta(t'-t)} \tag{2.21}$$

Where $\theta(t-t')$ is a step function where $t-t' < 0$, $\theta = 0$ and $\theta = 1$ for values greater than zero.

$$\delta\langle O\rangle = \int_{-\infty}^{\infty} dt' \int dr' \chi(r,t,r',t') V_{ext}(r',t') \tag{2.22}$$

Through application of the Fourier transform to change between time and frequency domain equations, the change in the expectation value of density, $\delta\langle\rho(r,\omega)\rangle$ under the perturbation introduced by light of frequency ω can then be examined, shown in equation 2.23. The poles of the response function then correspond with the excitation frequencies that give the spectral representation.[63]

$$\delta\langle\rho(r,\omega)\rangle = \int dr' \chi(r,r',\omega) V_{ext}(r',\omega) \tag{2.23}$$

Where $\chi(r,r',\omega)$ is given by equation 2.24 and $V_{ext}(r',\omega)$ is given by equation 2.25.[63]

$$\chi(r,r',\omega) = \lim_{\eta\to 0} -i\int_{-\infty}^{0} d\tau\langle\Psi(0)|[\rho_I(r,0),\rho_I(r',\tau)]\,|\Psi(0)\rangle e^{-(i\omega-\eta)\tau} \tag{2.24}$$

$$V_{ext}(r',\omega) = \int_{-\infty}^{\infty} V_{ext}(r',t') e^{i\omega t'} dt' \tag{2.25}$$

2.1.5 Atoms In Molecules

Bader's theory of atoms in molecules (AIM) examines the natural partitioning of a molecule based upon the gradient of the electron density.[64,65] For the purposes of this study, focus is placed upon the stationary points in the gradient of the electron density. The second derivative of the gradient at these points has been found to provide insight into the character of the electron density in the region around them.

The curvature at a stationary or critical point is characterised by the second derivative, which is determined in the form of the Hessian matrix.[66] When diagonalised at a topologically stable stationary point, the three eigenvalues that form the diagonal of the Hessian matrix correspond with the axes of maximum curvature. The rank, ω, and signature, σ, of the diagonalised Hessian matrix can be used to determine whether a critical point, labelled (ω, σ), is at a maximum, minimum, or saddle-point with positive or negative curvature, as shown in figure 2.1.[66]

- (3, -3) — Nuclear critical points. Maxima, where the gradient is characterised by three negative curvatures.
- (3, -1) — Bond critical points. Saddle points in the gradient where there are two negative curvatures.
- (3, +1) — Ring critical points. Saddle points with two positive curvatures and a negative curvature.
- (3, +3) — Cage critical points. Minima with three positive curvatures.

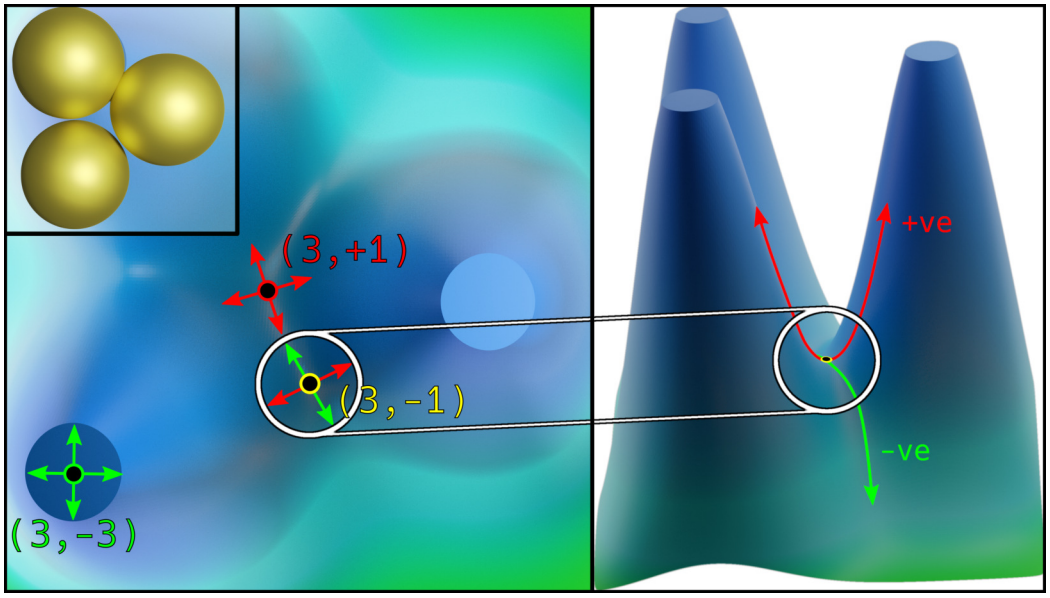

Figure 2.1: Truncated electron density in the plane of the Au_3 molecule, structure shown inset, with nuclear (3,-3), ring (3,+1), and bond (3,-1) critical points indicated (right). Side view of the (3,-1) bond critical point (left).

2.1.6 Software

The quantum mechanical codes used throughout this thesis were ORCA[51] and the Vienna Ab initio Simulation Package (VASP).[52–55] For both software packages, dispersion effects are modelled through Grimme's D3 dispersion correction with Becke-Johnson damping.[67–69]

2.1.6.1 ORCA

ORCA is an atom-centred code which implements, amongst other techniques, the density functional theory and time dependent density functional theory utilised in this work. It also provides basis sets and implementations of exchange-correlation functionals.[51] Analytical frequency analysis was used to establish that optimised geometries were within minima, as the frequencies obtained showed no imaginary modes.

By default within ORCA the Kohn-Sham orbitals are converged to self-consistency using Direct Inversion in Iterative Subspace (DIIS) algorithm, although the approximate Second Order Self Consistent Fields (SOSCF) can also be invoked. An ORCA input file used for a relativistic DFT optimisation is shown in the Example Input File 2.1.

The ORCA package ORCA2MKL and ORCA2WFN was also used to convert outputs to the molden and wfn file formats to enable analysis with the Multiwfn software package. This enables analysis of the electron density, interpretation of spectra, and also application of methodologies such as the Localized Orbital Locator, Metallicity measures, and Average Local Ionisation Energy.[70]

```
#Au19 Geometry Optimisation
! DFT RKS PBE ZORA TightOpt ZORA-def2-TZVP SARC/J  NormalPrint Grid7
    NoFinalGrid  D3BJ TIGHTSCF SlowCONV CPCM(water) XYZFILE

!FrozenCore

%scf
MAXITER = 6000
end

%method
IntAcc 7.0 # Increasing the radical grid from 5.67 (Grid7 setting) to 7.0.
end

%rel
picturechange  true
end

%basis
NewGTO Au "SARC-ZORA-TZVP" end
end

%pal
nprocs 144
end

*xyz 0 1
Au      -0.091394651      3.156644624      0.402096343
...
*

```

Input File Example 2.1: Extract from the Au_{19} ORCA input file.

2.1.6.2 Vienna Ab initio Simulation Package

The VASP code operates with periodic basis sets and pseudopotentials, as discussed above.[52–55] Similarly to ORCA, it also converges using a version of the DIIS algorithm, RMM-DIIS or Residual Minimisation / Direct Inversion of the Iterative Subspace.[71,72]

```
PREC = Accurate
ICHARG = 0      # Initiate charge as superposition of atomic charges
GGA = PE        # Use the PBE functional
##ISPIN = 2     # Restricted Kohn Sham
NPAR = 4        # Set Number of Cores
## Dispersion corrections
IVDW = 11       # Apply D3BJ Dispersion Corrections

## Electronic Relaxation
ENCUT = 400     # Set planewave cutoff to provide sufficient accuracy for Gold
EDIFF = 1E-6    # Electronic relaxation threshold, 1E-4 is default
LREAL = AUTO    # evaluate projection operators in real space
NELM = 250      # Set maximum number of SCF steps
ALGO = FAST     # RMM DIIS algorithm for convergence
LASPH    =  .TRUE.       ## includes non spherical contributions from the
    gradient corrections inside the PAW sphere

## Ionic Relaxation
EDIFFG= -1E-2  # Electronic relaxation threshold, 1E-3 is default, negative
    implies use forces rather than energy change
IBRION = 2      # Conjugate gradient ionic relaxation
NSW = 3000      # Maximum number of ionic steps
POTIM = 0.20    # Time step for optimisation
ISYM = 0        # Switch off symmetry

## DOS values
ISMEAR   =  0  # Insulators, DOS =-5 ; 1 k-point =0 ; metals =1
SIGMA    =  0.01 # Width of smearing

```

Input File Example 2.2: Extract from the Au_{19} VASP INCAR file.

A more specific detailing of the precise parameters used for each calculated is presented within the computational details section of each chapter.

Chapter 3

Seeding and Growth Processes

3.1 Seeding of Palladium Nanoparticles

Author's Note

This chapter discusses the stabilisation of the seeding process of Pd nanoparticles, it is the result of a collaboration between computational and experimental groups, respectively located at Cardiff University and Università degli Studi di Milano. Computational contributions were divided between atom-centred DFT and time-dependent DFT, performed by the author, and periodic plane wave DFT examinations of surfaces, performed by Dr Ali Nasrallah. In order to ensure completeness and contextualisation, experimental and plane-wave studies have been included and the results of these will be discussed alongside the atom-centred studies. The results and an analysis within this work have been previously published in the Journal of Physical Chemistry C.[73]

3.2 Introduction

As discussed within chapter 1, nanoparticle seeding is a crucial stage in directing the growth and morphology of the resultant species. The resultant species can show significantly distinct activities and properties based upon the initial reaction conditions and how capping agents and ligand species bind with the cluster. This study presents a combination of experimental investigation and theoretical interpretation applied to the process of synthesising palladium nanoparticles. This study employs a combination of experimental synthesis and spectroscopy and computational chemistry. Atom-centred DFT and TD-DFT, undertaken by the author, is applied to determine the struc-

ture of precursor species and periodic DFT, undertaken by Dr Nasrallah, is then used to determine the capping of the resultant nanoparticles.

3.3 Computational Methodologies

Atom-centred Density Functional Theory

Atom-centred density functional theory, as implemented in the ORCA quantum chemistry package was utilised to model the precursor molecules and capping agents present in solution during the synthesis of palladium nanoparticles.[51] The ORCA implementation of Karlsruhe quadruple zeta with valence and polarization function basis set (def2-QZVP), with an auxiliary Weigend basis set (def2/J), and Stuttgart–Dresden effective core potentials were employed to reduce the computational cost of the calculations.[74,62] Benchmarking tests were carried out using the Perdew–Burke–Ernzerhof (PBE), Burke-Perdew-86 (BP86), and Becke-3-Lee-Yang-Parr (B3LYP) exchange-correlation functionals, where the PBE functional was found to be a reasonable compromise between cost and accuracy for the second-row transition metals to be modelled in this study.[46,75–81] PBE also allowed for consistency between the periodic and atom-centred DFT methodologies. As with the functional, both methodologies also employed Grimme's empirical DFT-D3 to model dispersive interactions.[67] A further refinement of DFT-D3, DFT-D3BJ with Becke–Johnson damping, was used to improve the accuracy of the models examined in the atom-centred calculations, as the damping prevents artificial short-range repulsive interactions that can otherwise be introduced by the D3 corrections.[68,82,83]

Optimisation of the candidate structures was performed using analytical frequency calculations, which allowed for utilisation of the unapproximated Hessian during the optimisation process. These were also performed to optimize and confirm the geometry of the aminopropanol ligand. The convergence criteria for these calculations were an energy change of 2.72×10^{-5} eV with a maximum gradient of 5.14×10^{-3} eV Å^{-1} and a maximum displacement 5.29×10^{-4}Å.

The species present in the reaction solutions have also been examined through comparison of experimental and computational spectra. Computational UV–vis spectra were initially calculated using the computationally inexpensive simplified Tamm-

Dancoff approximation of time-dependent DFT (sTDA-DFT) where employment of the RIJCOSX approximation of the Coulomb and exchange integrals was used to further increase the efficiency of calculation.[84] sTDA-DFT has been shown to give good agreement with TD-DFT for the electronic transition energies, although it is known that intensities calculated using this method are less reliable.[84] Structures showing transitions in the sTDA-DFT spectrum, that were consistent with the wavelength of experimentally observed bands, were also calculated using the more demanding TD-DFT with the RIJCOSX integral approximation. TD-DFT spectra were examined using the Multiwfn software package, which applies Gaussian curve broadening.[70] Calculated excitations and orbital compositions were determined using the Mulliken method.[85] In order to examine the ligand bonding and oxidation state of the Pd atoms in the NP precursor molecule localized orbital centroid analysis was also undertaken using the methodology described by Vidossich and Lledos.[86] This utilized the ORCA software package's implementation of the Pipek-Mezey population-localisation methodology to project the more diffuse molecular orbitals onto localised orbitals which accurately describe the density found in the DFT-calculated electronic structure.[87,88] The gas-phase energy changes of reaction, ΔE_r, were calculated using equation 3.1.

$$\Delta E_r = \sum E_{\text{products}} - \sum E_{\text{reactants}} \tag{3.1}$$

Plane Wave Density Functional Theory

The work performed by Dr Ali Nasrallah on the extended surfaces of palladium utilised the VASP (Vienna *Ab initio* Software Package) code to model the experimentally formed NPs, which were modeled as extended periodic surfaces.[52–55] The valence electrons were modelled using a plane-wave basis-set and the projector augmented-wave method was used to represent atomic core.

The Brillouin zone was sampled using a Monkhorst–Pack grid with a k-point grid of $7 \times 7 \times 7$ for bulk optimisation of the Pd fcc unit cell, $7 \times 7 \times 1$ for surface optimisation, and $3 \times 3 \times 1$ k-points for all surface calculations following the optimisation.[89] Two surfaces were used for adsorption calculations, the (111), a 5 atom thick slab in a p$(4 \times 4 \times 1)$ supercell, and the (100), a c$(3 \times 3 \times 1)$ supercell of the 5 layer surface. During optimisation the lowermost three layers were constrained to the optimised bulk geometry and all other atoms were allowed to relax during the optimisation process. A 20 Å vacuum gap was utilised to separate the surfaces along the z-axis and, due to

this, dipole corrections in the z-direction were also employed. Kinetic energy cut-offs for the plane waves were set to 400 eV. The calculations were deemed to have sufficiently converged when the forces were less than 0.02 eV $Å^{-1}$. Adsorption energies were calculated using equation 3.2.

$$E_{\text{ads}} = E_{\text{ads +sl}} - E_{\text{ade}} - E_{\text{sl}} \tag{3.2}$$

where $E_{\text{ads +sl}}$ is the energy of the adsorbate adsorbed on the slab, E_{sl} is the energy of the naked slab, and E_{ade} is the energy of the adsorbate in the gas phase.

3.4 Results and Discussion

Solutions of aqueous Na_2PdCl_4 were prepared with 3-aminopropanol and 1,3-propanediol and analysed using both UV−vis and FT-IR spectroscopies. The analytics were performed as the solutions were reduced with $NaBH_4$ to produce a sol of capped palladium nanoparticles. These particular capping agents, 3-aminopropanol (AP) and 1,3-propanediol (PD), were selected for study as they are structurally similar to the monomeric units of the polymer species that are commonly utilised in the stabilisation of nanoparticle systems.

Solvation of the Na_2PdCl_4 has been shown by Elding and the work of Freund *et al.* to produce $PdCl_4^{2-}$ and $[PdCl_3(H_2O)]^-$ as the predominant species found following dissolution in an aqueous acidic environment.[90–92] Within these solutions, Grogan and Nakamoto demonstrated that dimeric species, such as the Pd analogue to the Pt salt Zeise's dimer, can also form.[93] As such, precisely identifying the molecules found within the precursor solution is itself challenging, to assist with this characterisation time-dependent density functional theory calculations were employed in order to predict the UV-vis spectra of candidate species. These structures were first screened using sTDA-DFT and then structures showing potential for absorbance in the correct spectral regions were more accurately characterised using TD-DFT, shown in figure 3.1. Of the potential species examined, only $PdCl_4^{2-}$, $[PdCl_3(H_2O)]^-$, and $Pd_2Cl_6^{2-}$ were found to be potentially consistent with the experimentally observed UV-vis spectrum. The computed data for the chlorine-bridged dimer indicate that the characteristic 420 nm band in the experimental spectra is due to Cl p — Pd s transition. However, the breadth of this band is likely due to the contributions of the 470 nm transition, indicating a predominantly Pd d — Pd p excitation involving both palladium ions of the dimer, and a 388 nm transition observed in the computed spectrum of $PdCl_4^{2-}$, attributable to a predominantly p — p excitation from chlorine to palladium.

The broad band present at 425 nm was therefore determined to be likely composed of a combination of peaks caused by contributions primarily from three of the computationally modelled structures. Furthermore, the shoulder observed in the experimental spectrum at 310 nm is consistent with the computed spectrum of the dimer shown in figure 1B. The experimental band centered at 418 nm could include all the contributions predicted by the model systems. The agreement of these computed excitations with experimental spectra suggests that the solution is an equilibrium mix-

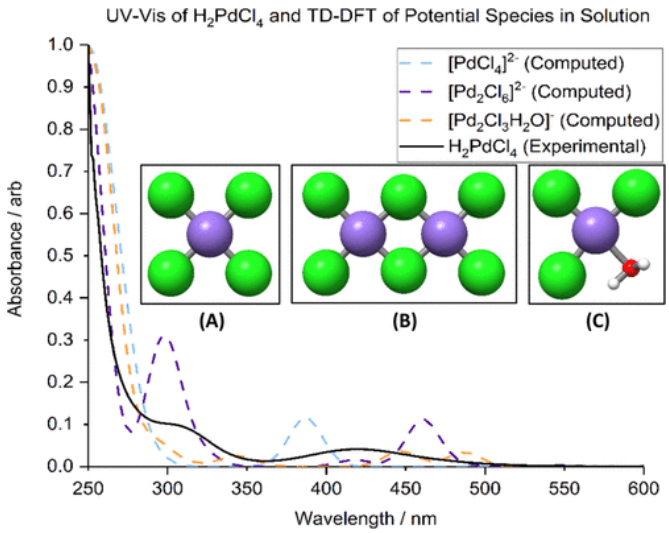

Figure 3.1: UV-Vis spectrum of H_2PdCl_4(Aq) and TD-DFT spectra of candidate seed solution species, structures of candidate molecules $PdCl_4^{2-}$, $Pd_2Cl_6^{2-}$, and $[PdCl_3(H_2O)]^-$ shown inset as, respectively, A, B, and C.

ture of $Pd_2Cl_6^{2-}$, $PdCl_4^{2-}$, and $[PdCl_3(H_2O)]^-$. The existence of these species is also supported by the calculation of the energies of reaction for the formation of $Pd_2Cl_6^{2-}$ and $[PdCl_3(H_2O)]^-$ from $PdCl_4^{2-}$, shown in table 3.1. These values indicate that the formation of the dimer and the water-containing complex are both exothermic processes with the dimer being the most energetically favourable of the three.

Product	ΔE_r / kJmol^{-1}
$Pd_2Cl_6^{2-}$	-252
$[PdCl_3(H_2O)]^-$	-215

Table 3.1: Energy change of reaction, ΔE_r, for the formation of $Pd_2Cl_6^{2-}$ and $[PdCl_3(H_2O)]^-$ from $PdCl_4$.

The addition of the PD capping agent to the Pd^{2+} solution led to no significant changes in the observed spectrum of the solution (cyan dotted line vs blue line in figure 3.2). Conversely, upon reduction with $NaBH_4$ (black line), the band at 418 nm was not evident, however, an increased background absorption together with an increase in the absorbance at short wavelengths, with a maximum absorption at 285 nm, were observed.

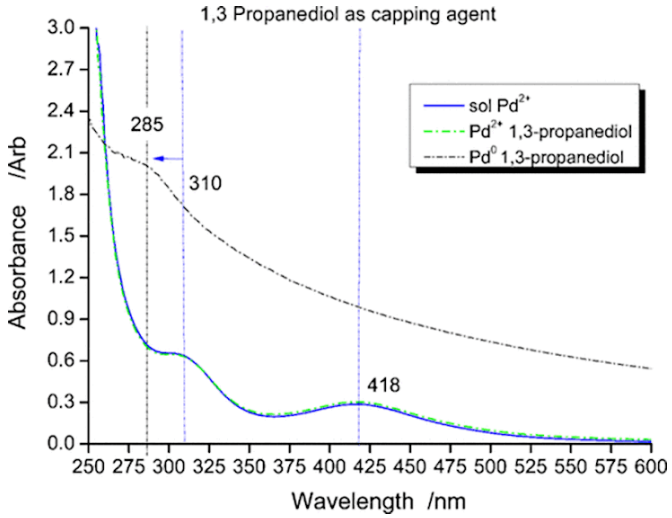

Figure 3.2: UV−vis spectra of H_2PdCl_4 in solution (blue) in the presence of the capping agent PD (green), Pd with PD reduced (black).

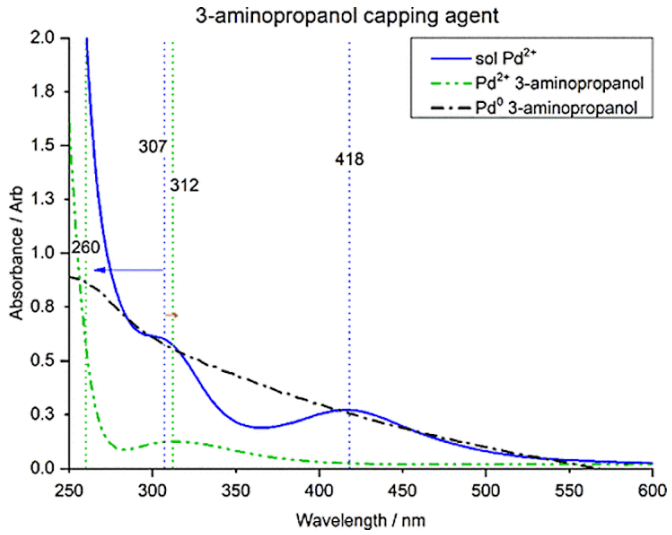

Figure 3.3: UV−vis spectra of H_2PdCl_4 in solution (blue), in the presence of the capping agent AP (green), Pd with AP reduced (black).

With both the PD capping agents, the observed increase in the background intensity can be attributed to the scattering induced by the formation of colloidal palladium particles and this could be responsible for the decrease of the band at 418 nm. The blue shift of the CT band could be correlated to the increase of pH because of the $NaBH_4$ addition. However, the exact assignment of the observed band at 285 nm is still undetermined. According to Klasovsky et al., this peak relates to plasmon excitation in the colloidal particles.[90] However, Boily argued that it is also compatible with a CT transition of Pd chloro−hydroxo complexes, $PdCl_x(OH)_y^{n-}$, which are stable solution

species under our experimental conditions according to the hydrolysis equilibrium.[94]

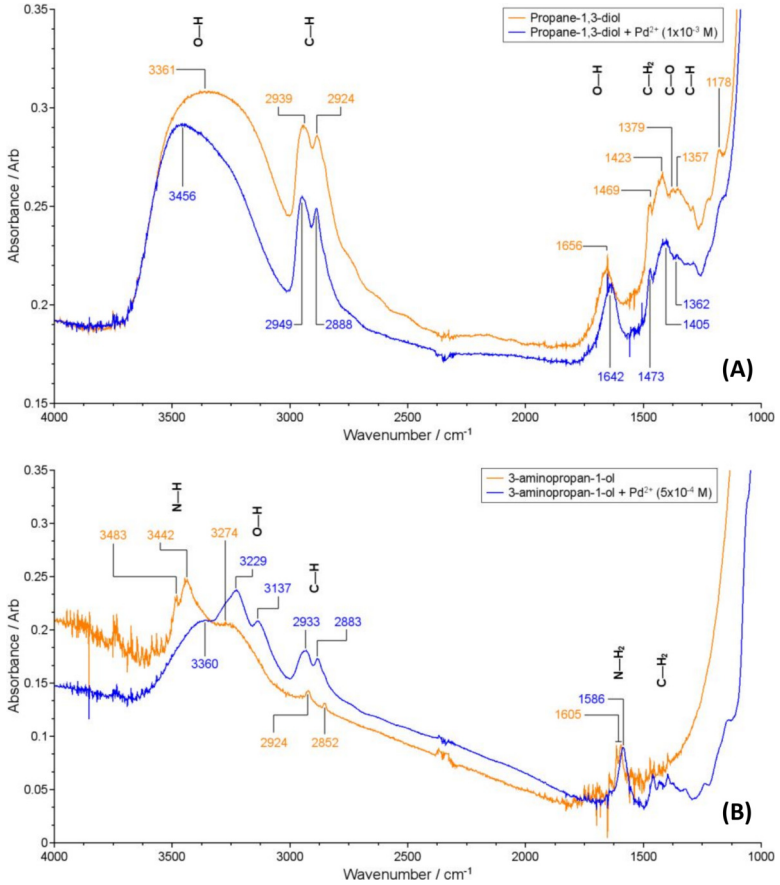

Figure 3.4: (A) FT-IR spectra of PD and Pd−PD (top). (B) FT-IR spectra of AP and Pd−AP (bottom).

The effect of adding the AP capping agent to the sol Pd^{2+} with subsequent metal reduction is shown in figure 3.3. As expected, the initial UV−vis spectrum of Pd(II) (blue line) is consistent with that of figure 3.1, further pointing out the reproducibility of the experimental procedure. Upon addition of AP (green line), the broad band centered at 418 nm is reduced, and the decrease in intensity of the shoulder at 307 nm is accompanied by a broadening and a shift of the peak to 317 nm. These significant changes are a consequence of the chlorine ligand substitution by the AP capping agent. These results are consistent with the computational analysis; the TD-DFT spectrum of the most favourable product, $[PdCl_3AP]^-$, (figure 3.3, dashed blue line) was also found to be consistent with the experimental results. The energies of reaction for the formation of aminopropanol ligand complexes from $PdCl_4$ are shown in table

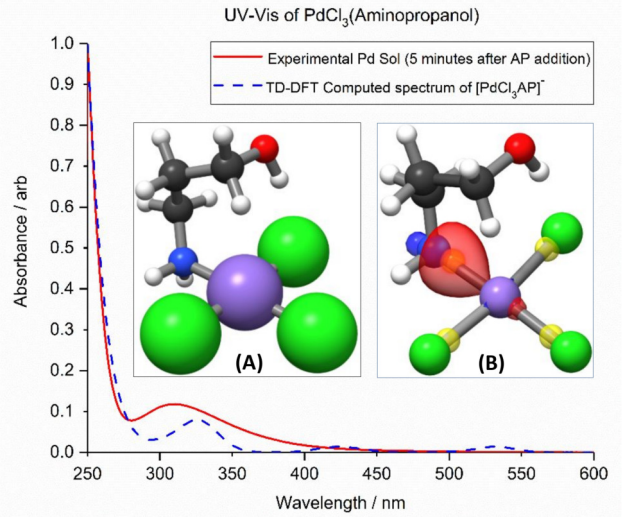

Figure 3.5: UV−vis spectra of $PdCl_4^{2-}$ sol in the presence of the capping agent AP (green) and computed TD-DFT spectrum of $PdCl_3AP^-$ (blue dashed). Inset: (A), $PdCl_3AP^-$ lowest energy geometry; (B), $[PdCl_3AP]^-$ with the Pd—N localized bonding orbital and the centroids for the Pd—N and Pd—Cl bonds. Color code: Pd: lilac; Cl: green; O: red; N: blue; C: dark gray; H: white; and localized orbital centroids: translucent yellow.

3.1. The peak observed at 334 nm in the computational spectrum shows an excitation from a hybrid Pd d−Cl p orbital to a molecular orbital composed from the palladium sp and a hybridization of orbitals in the aminopropanol ligand. This agreement with the experimental spectrum strongly suggests that the aminopropanol is directly attached to a Pd^{2+} species in a structure consistent with the computational predictions. A similar suggestion was reported by Groppo *et al*. who compared the diffuse reflectance UV−vis spectra of bulk $Pd(OAc)_2$ diluted in SiO_2 and in pyridine.[95] The bulk $Pd(OAc)_2$ in silica exhibited a band maximum at 400 nm, whilst the one diluted in pyridine revealed a peak centred around 330 nm. As a possible explanation, the authors suggested that one or two acetate ligands were substituted using pyridine units. This interaction between the NH group and the Pd^{2+} ions involves a strong interaction between the electron-rich amino group and the metal ion, which could induce a change in the actual oxidation state of the metal by partial reduction. For this reason, centroid analysis of the Pipek−Mezey localised orbitals was utilized to examine the oxidation state of Pd and the character of the AP−metal bond, figure 3.5B. The localized two-centred bonding orbitals indicated that the Pd−AP bond was largely dative in character with the electrons in the bonding orbital being biased toward the more electronegative ni-

trogen. Analysis of the single atom orbitals showed the electronic configuration of the Pd atom to be consistent with Pd(II), 4s2 4p6 4d8 because of the presence of eight centroids centred upon the Pd atom and the bonding orbital centroids being biased toward the ligands. Coordination of the ligand does not therefore involve a redox process. Upon reduction with $NaBH_4$, the UV−vis spectrum (Figure 3.3, red line) assumed a very broad profile, where it is difficult to uniquely identify defined features or any eventual shifts. A significant increase in the background absorbance was indeed observed, which, as in the case of PD, was attributed to Willis−Tyndall scattering which is characteristic for the formation of particles.

In order to obtain more information on the coordination of PD and AP to Pd^{2+} ions, FT-IR spectra of the Pd(II) complexes were recorded and compared to the FT-IR spectra of the pure ligand molecules, as shown in figure 3.4. In the case of 1,3-propanediol, figure 3.4A, the interaction with Pd^{2+} ions seems to provoke negligible perturbations in the molecular structure of the ligand. Indeed, in addition to an overall decrease in intensity upon Pd^{2+} addition, only an erosion of the broad peak at 3361 cm^{-1} because of the stretching of −OH groups, together with a shift of the peak related to the −OH bending mode from 1656 to 1647 cm^{-1} are observed, which indicates that the presence of the Pd^{2+} ions perturbed these groups. This spectroscopic feature points out that the interaction between the metal ions and the 1,3-propanediol ligand occurs through the −OH groups. Conversely, more significant changes were observed in the FT-IR spectrum of AP after interaction with Pd^{2+} ions (Figure 3.4B). The peaks observed at 3483 and 3442 cm^{-1} , related to the symmetric and antisymmetric stretching modes of the −NH group, are decreased and new bands at 3229 and 3137 cm^{-1} are produced immediately upon the addition of Pd^{2+}. Moreover, the −N−H bending mode observed at 1605 cm^{-1} is shifted to 1586 cm^{-1}. To rationalize these differences, in particular, to understand if the peaks at 3229 and 3137 cm^{-1} are the result of a marked shift of the symmetric and antisymmetric stretching modes of the −NH group or of a strong perturbation of the −OH group, frequency calculations were performed in order to simulate FT-IR spectra for the most stable conformations of the Pd(II)−AP complex.

Favourable configurations of the 1,3-aminopropanol were optimized in the gas phase with both plane-wave and atom-centred methodologies, the two most stable configurations were found to be a straight chain configuration and a conformation with an internal hydrogen bond between the hydroxyl oxygen and the amino nitrogen, as is

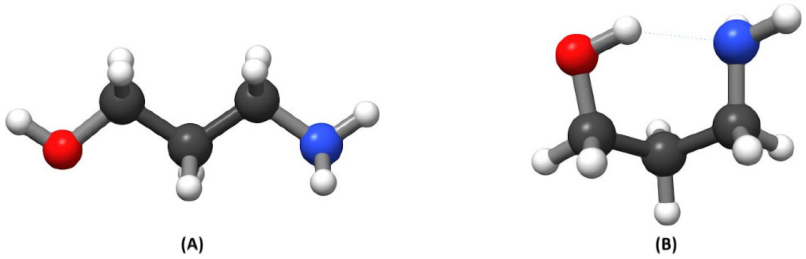

Figure 3.6: Optimization of two different conformations of the AP adsorbate in the gas phase: (A) all *trans*, (B) conformation with internal H-bond.

shown in figure 3.6, with the latter being the most stable. The H-bonded conformation was found to have an electronic energy ≈ 0.8 eV lower than that of the other structure, which was also consistent with results obtained using an atom-centered basis set. These results confirmed the former hypothesis coming from the FT-IR discussion, indicating that the interaction between the metal ions and the AP ligand occurs through the $-NH_2$ group. The complete assignments of the FT-IR bands are summarized in table 3.3. For this reason, the interaction of the AP molecule with metallic Pd surfaces was also investigated. The most stable configuration of AP was then adsorbed on the two low index surfaces of palladium metal: Pd(111) and Pd(100). Structures with AP bound to the surface through the oxygen atom or the nitrogen atom were investigated. It was found that those in which both the oxygen and the nitrogen atom bind to the surface at the same time were unstable because of internal strain within the AP. In the case with AP adsorbed through the amine nitrogen atom, hydroxyl hydrogen is also attracted toward the surface. Table 3.2 and figures 3.7 — 3.10 summarize the results obtained.

The conformation of aminopropanol where the amine moiety was binding with the Pd(111) and Pd(100) surfaces was found to be the most favourable of all configurations, showing similar preferential N—Pd binding to that of molecular precursor. The relative energies of the adsorption on the Pd(100) and Pd(111) suggest that there is a small favourability for AP adsorption upon the Pd(100). Reduced accessibility of the Pd(100) facets through preferential adsorption would favour nanoparticle growth on the Pd(111) facets, resulting in greater surface area for Pd(100) facets. However, this energetic difference is relatively small, 4 $kjmol^{-1}$, and close in magnitude to the potential error introduced by the approximations of the DFT methodology. As a result of this, whilst these energies appear to indicate that the capping agent will be adsorbed

Pd(111) surface		
Configuration	Energy of adsorption / kJ mol^{-1}	N−Pd or O−Pd distance / Å
Nitrogen binding	−145	2.15
Oxygen binding	−95	2.34
Pd(100) surface		
Configuration	Energy of adsorption/kJ mol^{-1}	N−Pd or O−Pd distance/Å
Nitrogen binding (O up)	−127	2.16
Nitrogen binding (O down)	−149	2.15
Oxygen binding	−86	2.32

Table 3.2: Adsorption energies of the different configurations of 3-Aminopropan-1-ol on Pd(100) and Pd(111) surfaces.

preferentially on Pd(100) facets, this cannot be specified with certainty. These findings do emphasise that the effects of preferential blocking of the Pd(100) surface should be considered and quantified for other amine moiety containing adsorbates and capping agents.

In order to support that the nitrogen-binding model is consistent with the observed experimental results, frequency calculations on the most stable configurations were performed in order to obtain infrared spectra for the most favourable nitrogen and oxygen binding configurations upon both the Pd(100) and Pd(111) facets, shown in figure 3.11. The correlation between the experimental IR spectrum and the computed spectra show good agreement with the amino—Pd binding configurations. Examination of the oxygen-binding spectra also shows that the expected O—H vibrational modes would be less infrared active than the nitrogen-binding O—H modes, which are observed in both the experimental and computed nitrogen binding spectra. Combined with the energies calculated above, this suggests that the aminopropanol caps the NP surfaces and that it bonds preferentially through the nitrogen containing group.

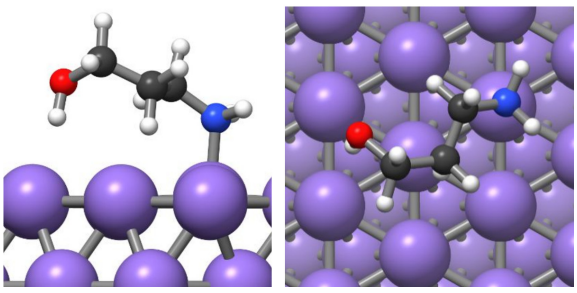

Figure 3.7: Adsorption of the AP adsorbate on the Pd(111) surface with the nitrogen binding to the surface.

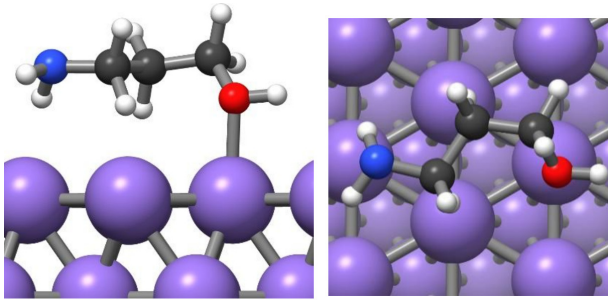

Figure 3.8: Adsorption of the AP adsorbate on the Pd(111) with the oxygen binding to the surface.

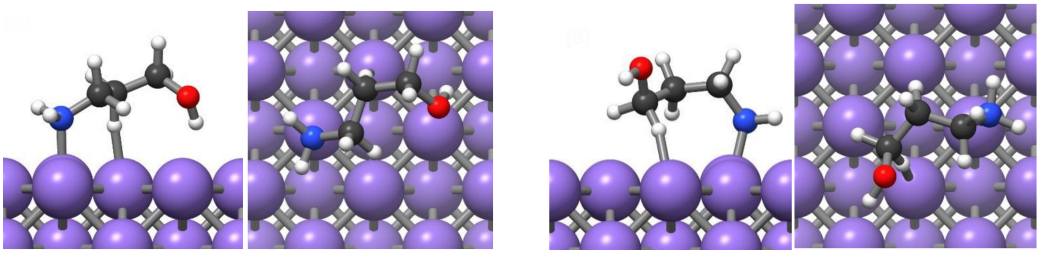

(a) (b)

Figure 3.9: Adsorption of the AP adsorbate on Pd(100) with the nitrogen binding to the surface and (a) oxygen pointing downward and (b) oxygen pointing upward.

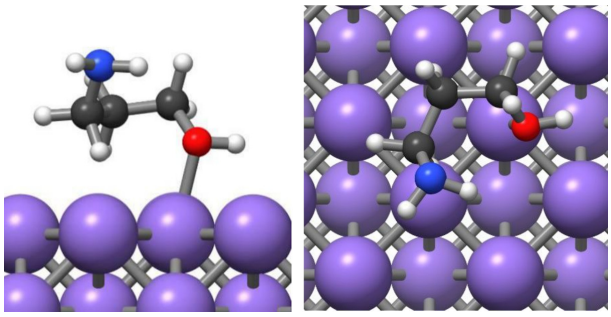

Figure 3.10: Adsorption of the AP adsorbate on Pd(100) with the oxygen binding to the surface.

Bands observed for 1,3-propanediol	
Vibrational frequency / cm^{-1}	Assignment (vibrational mode)
3361	–OH stretching
2939 and 2924	–CH symm and asymm stretchings
1656	–OH bending
1469	–CH2 bending
1423	C-O stretching
1379	C–H bending
Bands observed for Pd-1,3-propanediol	
Vibrational frequency / cm^{-1}	Assignment (vibrational mode)
3456	-OH stretching
2949 and 2888	–CH symm and asymm stretchings
1642	–OH bending
1473	–CH2 bending
1405	C-O stretching
1362	C–H bending
Bands observed for 3-aminopropanol	
Vibrational frequency / cm^{-1}	Assignment (vibrational mode)
3483 and 3442	–NH symm and asymm stretching
3274	–OH stretching
2924 and 2852	–CH symm and asymm stretchinge
1605	–OH bending
Bands observed for Pd-3-aminopropanol	
Vibrational frequency / cm^{-1}	Assignment (vibrational mode)
3360	–OH stretching
3229 and 3137	–NH symm and asymm stretching
2933 and 2883	–CH symm and asymm stretching
1586	–OH bending

Table 3.3: Calculated vibrational frequencies and assignments of the FT-IR bands.

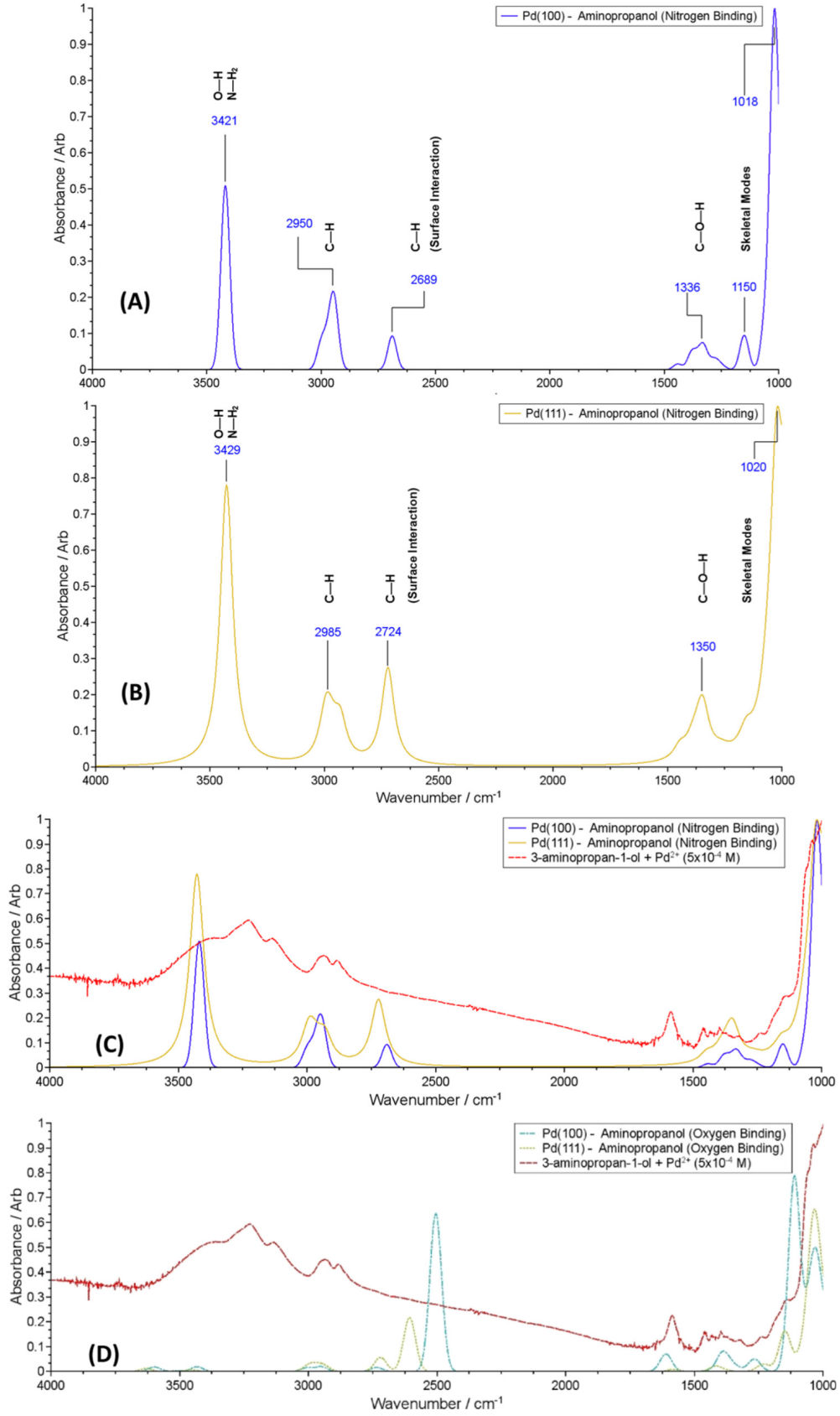

Figure 3.11: (A) FT-IR spectra of PD and Pd−PD (top). (B) FT-IR spectra of AP and Pd−AP (bottom).

3.5 Conclusions

The supportive combination of experimental spectroscopy, DFT, and TD-DFT modelling allowed for the determination of the coordination structures of small ligands to Pd species during the metal nanoparticle formation process. Despite these capping agents being model systems, the difference in adsorption for the propanediol and aminopropanol provides some insight into the interaction of larger capping agents and palladium surfaces. The preferential interaction of the amine moiety, in comparison to the alcohol moiety, suggests the interaction of amine and alcohol containing capping agents will show a preference for amine—Pd interaction. However, as these model systems are small and therefore do not show the steric interactions and surface packing of real capping agents, this does limit the strength of conclusions that can be drawn upon this basis. Whilst these model systems help to develop an understanding of the phenomena at the interface between the metal surface and the ligand layer, further study of real capping agents and realistic surface loadings are necessary before specific insight into those systems can be provided. Differences were experimentally observed for the O- and N-containing ligands. It was also shown that 1,3-aminopropanol reacts with the molecular precursors to form a Pd(II)Cl_3AP complex prior to nanoparticle formation and it is suggested that, by forming this species, AP is potentially able to influence the growth processes during the subsequent reduction. AP also shows some differences in preferential binding with the Pd surfaces, although for these are small and close to the limit of theoretical accuracy. This suggests that nitrogen-binding capping agents may have the potential to preferentially influence growth processes to favour expansion of the Pd(100) facets but this cannot be conclusively determined by this study. These data will also provide a stimulus to a deeper investigation on the role of the capping agent in metal NP synthesis and in their catalytic behaviour.

Chapter 4

Bonding Within Nanoparticles

4.1 Introduction

The catalytic utility of noble metal nanoparticles is widely acknowledged and frequently observed to shows a range of properties that are entirely distinct from those observed in the bulk forms of the material. Smaller particles generally display greater activity and, in order to better understand how small, highly-catalytically active nanoparticles develop properties distinct from either bulk or molecular materials, a comparative case-study of Au_{19} and various molecular gold species will be undertaken. As particle size increases, the electronic structure of the gold nanoparticles approaches that of the bulk. However, for smaller particles, a larger change in electronic structure can be achieved through smaller changes in size. This can lead to quantum size effects, which have been attributed to a range of phenomena including super-atoms being formed by nanoparticle species.[5,9]

Figure 4.1: Au_{19} nano-crystallite.

Nanoparticles often present a unique challenge in the characterisation and understanding of their physical properties, as they lack the periodic symmetry of larger crystallites but often are more complex than smaller molecular species. The changes in morphology, symmetry, and composition of nanoparticles can be considered as being components that determine their macroscopic behaviour and interactions with other

species. As well as a characterisation of the electronic structure using descriptors, a novel method for characterising tensor properties derived from electronics will also be introduced. In particular, this generalisable method will be applied to approximating the elasticity of the Au_{19} nanoparticle. Elasticity, which results from the concerted influence of the fundamental electronic structure, will be described in this chapter, are often non-linear and predicting, measuring, or characterising them for nano-scale systems can be challenging but also provide significant insight into how these structures behave under changing conditions or whilst undergoing reactions.

4.1.0.1 Nanoparticle Elasticity

Elasticity is a measure of the relationship between the restorative force, stress, produced under deformations, strains, that lie within the elastic limit for a structure.[96] Once the deformation exceeds the elastic limit, bonds are broken and the structure deforms irreversibly within the plastic domain.[97] Stress and strain are related through elastic tensors, an example of which is the elastic compliance, c, as is shown in equation 4.1. Strain and stress, both of which are tensor properties, depend upon the orientation and strength of the bonds that form the molecular structure and as such can be difficult to examine for nanoparticle systems, which lack the periodic symmetry and homogeneity of surface or bulk systems.[32,96,98]

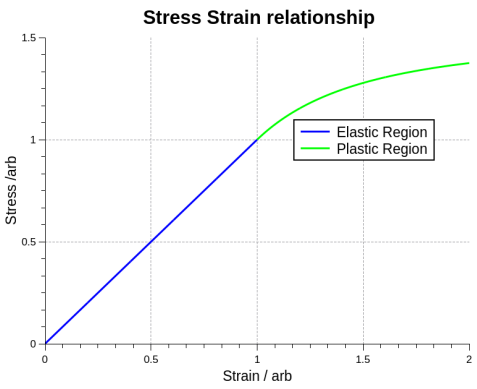

Figure 4.2: Stress-strain plot showing a one-dimensional linear elastic region (blue) and a non-linear plastic deformation (green).

$$\sigma = c\epsilon \tag{4.1}$$

Where σ is stress, ϵ is strain, and c is elastic compliance.

The elasticity of nanoparticles has been found to have significant effects upon the interaction with biological systems. Recent examinations of the effects of nanoparticle elasticity upon the interactions with biological systems have demonstrated that

it has effects upon rates of phagocytosis and endocytosis, blood persistence, and the specificity of tissue-targeting.[29,30,99] For these reasons, characterising the elasticity of nanoparticles has been demonstrated to be a crucial element in the design of effective nano-platforms for drug delivery. The determination of the elastic behaviour when particles are adsorbed upon surfaces also presents an interesting application, where elasticity can help to understand the interface.

The observed utility of understanding the elasticity of nanoparticles has led to experimental measurements of nanoparticle elasticity becoming common. These are usually performed using methods such as atomic force microscopy, by which the Young's modulus of the structure can be determined. However, despite the importance of elasticity to predicting the suitability of nanoparticles for various applications, theoretical calculations are relatively uncommon.

A method commonly utilised in the determination of elastic constants for bulk materials is that presented by Theodorou and Suter in their work upon the calculation of elastic constants in polymeric glasses.[100,101] This work uses small deformations and position rescaling to calculate elastic constants but, as part of that methodology, explicitly neglects entropic contributions and fixes bond lengths and bond angles as constant. These assumptions and approximations cannot necessarily be applied to the characterisation of nanoparticles. Entropic effects upon the elastic constants can occur due to the effective surface restructuring during elastic deformation. Similarly application of position rescaling is non-trivial without a unit cell and cannot necessarily capture the changes in bond angle and length that do occur during nanoparticle deformation.

The widely utilised fluctuation formula derived by Rahman and Parinello presents a different approach to elasticity, where elastic constants for a material are calculated from the stresses that occur during a molecular dynamics trajectory, which was improved upon again by the work of Gusev et al.[102–106] Whilst this methodology works well for the determination of elastic constants of solid materials, in order to apply it to nanoparticle systems the average volume of the system or a system of constant volume is required. This is non-trivially defined for nanoparticle species, in comparison to crystalline structures where it can be easily determined.

In the calculation of stress and strain for crystal structures, the symmetry and homogeneity of the crystal structures can be used to reduce the complexity of the problem. Similarly, for inhomogeneous solid-state materials, the volume and fluctuations can be utilised. However, for a nanoparticle system none of these properties can be readily determined or assumed. Extended periodic structure allows for the terminations to be neglected, as their effects are negligible in comparison to the bulk.[96]

For nanoparticle systems, the imperfect crystal-like structure does not necessarily guarantee the symmetry of the tensor, as these systems can be of low symmetry or show significant deformations in realistic environments. Surface terminations, differing coordination environments, and aperiodic exclusions and inclusions cause inhomogeneities that combine with indeterminate volumes to make nanoparticle elasticity characterisation a non-trivial problem to solve. As the size of the structure decreases, the elastic constants also do not correspond well with the classical elasticity theory that is used to represent the homogeneous crystal structure or bulk material.[107]

The utilisation of locally resolved elastic constants has found success in characterising inhomogeneous materials. By defining stress and strain with respect to localised regions with an inhomogeneous system, the elasticity of these materials have been effectively characterised.[105,108–110] Similar to the locally resolved elastic constants that have shown success in inhomogeneous materials, this work proposes a bond-localised examination of stress and strain, where bonds are categorised according to the coordination environment of the atoms at either end. This chapter sets out a protocol for applying a machine learning derived methodology as a non-linear solver for resolving the bond-localised elastic constants and demonstrates the application of this approach using a case-study of the elastic tensor of Au_{19} system.

This chapter examines the character of the surfaces and bonds within the Au_{19} nanoparticle and introduces a novel method for applying machine-learning methodologies in the determination of tensor properties, specifically applied to the elasticity of Au_{19}.

4.2 Methodology

4.2.1 Computational Details

Au_3 and Au_{19} nanoparticle structures were optimised using atom-centred density functional theory, as implemented within the ORCA software package.[51] Segmented all-electron relativistic corrections, SARC-ZORA-TZVP and the ZORA corrections to the Hamiltonian were applied to introduce the relativistic corrections necessary for accurately characterising the electronic structure of gold containing molecules with a frozen core approximation applied in the case of Au_{19} in order to reduce the computational expense.[57–59,61] The convergence criteria for these calculations were an energy change of 2.72×10^{-5} eV with a maximum gradient of 5.14×10^{-3} eV $Å^{-1}$ and a maximum displacement 5.29×10^{-4} Å.

The PBE functional was employed to account for exchange-correlation effects as Generalised Gradient Approximation functionals can provide a more accurate description of the metal-metal bonding that is present in nanoparticle systems than hybrid functionals such as PBE0. Although PBE0 has been shown to provide a more accurate model of third row transition metal complexes, hybrid functionals can introduce unphysical properties when applied to metals, such as predicting band-gaps for metallic materials, and so have not been utilised in the examination of the metallic systems in this study.[48,111]

4.2.2 Bonding Characterisation

Bader's atoms in molecules (AIM) topology analysis of the electron density and descriptors, as implemented in the MultiWFN software package, were utilised to examine the properties of the electronic structure. The specific descriptors used in this examination were used to look at the local density of states, orbital localisation and kinetic energy measures, and also the character of the bonding and non-covalent interactions within the nanoparticle.

Descriptor Functions

As is shown in equation 4.2, the average local ionisation energy, $\bar{I}(r)$, ALIE, provides a measure of the energy required to extract an electron from a specific region of

space.[112]

$$\bar{I}(r) = \frac{\sum_i \rho_i(r)|\epsilon_i|}{\rho(r)} \tag{4.2}$$

Where ρ is the electron density, i is the orbital number, and ϵ_i is the orbital energy.

As it is the sum of orbital densities multiplied by the magnitude of the orbital energy over the complete electron density at a given point, this provides a relative measure for determining the favourability of sites of ionisation. Low ALIE regions have been shown to correlate well with known electrophilic reactive sites, whereas high ALIE indicates a regions with a relatively high propensity to be receptive to electron addition, thus allowing some insight into areas where reduction and oxidation are more or less favourable.[112,113] This is particularly useful when mapped onto the van der Waals (vdW) surface, herein defined as the 0.001 or $99.9\,\%$ confidence surface of electron density.

The metallic character, which is a measure of the freedom of electrons with respect to their localisation to atomic nuclei, of bonding within the particles was examined using two measures, metallicity, shown in equation 4.3, and the dimensionless metallicity, shown in equation 4.4.[114,115] Both of these quantities measure the same fundamental property, namely the electron density over the second-order gradient of the electron density; however the dimensionless metallicity has been found to improve the compatibility of the measure with the theory of atoms in molecules and critical points developed by Bader.[64,65]

$$\xi_j(r) = \frac{\rho(r)}{\nabla^2\rho(r)} \tag{4.3}$$

$$\xi_m(r) = \frac{36(3\pi^2)^{2/3}}{5}\frac{\rho(r)^{5/3}}{\nabla^2\rho(r)} \tag{4.4}$$

As discussed by Ayers and Jenkins, the localized orbital locator (LOL), equation 4.5, proposed by Schmeider and Becke provides a conceptual inversion of metallicity, where values greater than 1 show orbital localisation to specific regions of space.[115,116] The measure itself can be considered a transformed function examining the electron density relative to the orbital kinetic energy density at a given point.

$$\textit{LOL}(r) = \frac{S(r)}{1 + S(r)} \tag{4.5}$$

$$S(r) = \frac{\frac{3}{10}(3\pi^2)^{2/3}\rho(r)^{5/3}}{(1/2)\sum_i \eta_i |\nabla\phi_i(r)|^2} \tag{4.6}$$

Where ϕ is the orbital wavefunction, i is the orbital number, and η_i is the ith orbital occupation number.

Regions of Slow Electrons, equation 4.7, are a measure of electron kinetic energy with results similar to the localized orbital locator.[117] It can be considered as a measure of electron density with respect to the time spent within a given region of space.[115,117] This gives insight into the degree of localisation and the potential reactivity of specific regions within the electron density.

$$\nu(r) = \frac{\frac{3}{10}(3\pi^2)^{2/3}\rho(r)^{5/3} - \frac{1}{2}\sum_i \eta_i |\nabla\phi_1(r)|^2}{\frac{3}{10}(3\pi^2)^{2/3}\rho(r)^{5/3} + \frac{1}{2}\sum_i \eta_i |\nabla\phi_1(r)|^2} \tag{4.7}$$

Non-covalent interactions were also examined using the methodology presented by Johnson *et al.*; here the reduced density gradient (RDG), given by equation 4.9, is either plotted against or mapped by the Ω function, which multiplies the sign of the second largest eigenvalue, $\lambda_2(r)$, of the electron density by the electron density as shown in equation 4.10.[118] This provides significant insight into the weak non-covalent interactions that can have both stabilising, attractive function and can also manifest as destabilising repulsive forces and can provide an understanding of the interaction between atoms that is not observed through other methodologies.

$$\textit{sign}(x) = \frac{x}{|x|} \tag{4.8}$$

$$\text{RDG}(r) = \frac{1}{2(3\pi^2)^{1/3}} \frac{|\nabla\rho(r)|}{\rho(r)^{4/3}} \tag{4.9}$$

$$\Omega(r) = \textit{sign}(\lambda_2(r))\rho(r) \tag{4.10}$$

The synthesis of the combined information obtained through applying these descriptor functions is utilised to present a coherent understanding of the bonding within the nanoparticle structure and the vdW surface character that lends itself to catalytic activity.

4.2.3 Determining High-quality Approximate Elastic Tensors

In order to address the difficulties in characterising nanoparticle elasticity as discussed in the introduction to this chapter, this work will seek to provide a methodology for the calculation of elastic tensors, with potential for generalisation to other tensor properties, that are high-quality, low-cost approximations with a diverse range of potential applications.

Coordination Definition of Strain

By defining elasticity in terms of a bond-aligned tensor, where bonds are defined as existing between atoms that fall within a specified radius of another atom in the unstrained geometry, the elastic tensors can be calculated such that they correspond to the bonding environments that exist within the nanoparticle system, rather than in alignment with the strain vectors that displace the whole system. To better characterise the elasticity of nanoparticles, the bonds are first characterised based upon the coordination environment of the pair of atoms. For Au_{19} three distinct bond coordination environments were determined to exist, as shown in figure 4.3. This allows for the elasticity to be expressed as a tensor that distinguishes between the bonding environments.

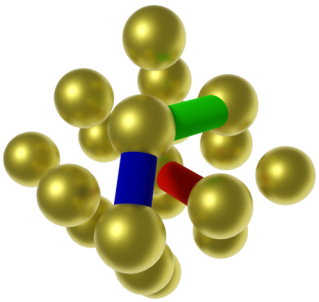

Figure 4.3: Au_{19} with the three distinct bond coordination environments indicated in red, blue, and green.

The bonds within the geometry, as distinguished by the coordination of the pair of bonding atoms, are reorientated to give an aligned bond vector that is consistently orientated with respect to the elastic tensor. The process for this is defined below and shown in figure 4.4.

(1) The lowest coordination atom in the bond is placed at the origin.

(2) The vector between the two atoms of the bond is then rotated such that it aligns with the z-axis of the Cartesian space.

(3) The x,y-components of the other bonds involving the low-coordination atom are averaged. If the magnitude of the average vector is non-zero then this average

vector is aligned with the x-axis. If the magnitude of the average vector is zero then the longest bond vector is aligned with the x-axis.

(4) The inverse of these rotations is then stored in order to allow for the forces to be realigned with the real Cartesian space.

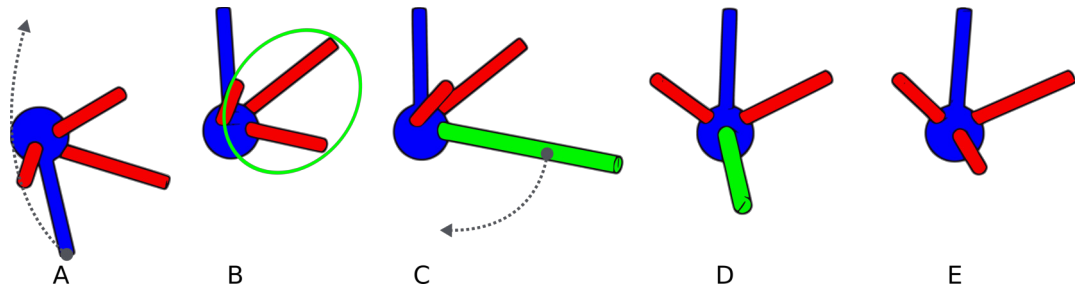

Figure 4.4: Alignment process for the blue bond. The blue sphere is the lowest coordinate atom of the blue bond and the red bonds indicate the other bonds to the low-coordination atom. The green average bond vector indicates the combined x,y components of the remaining bonds following the alignment of the blue bond with the z-axis.

The aligned-bond strain is given by equation 4.11. The rotation, R_i that was used to align the unstrained bond, u_i, is applied to the strained bond vector, v_i, and the difference between these vectors, b_i, is the aligned bond strain. Pairs of atoms within the unstrained geometry are stored and recalled when examining the strained geometry in order to reduce the number of searches for neighbours.

$$b_i = R_i v_i - R_i u_i = \begin{pmatrix} x \\ y \\ z \end{pmatrix} \tag{4.11}$$

The strain, b_i is then expressed as a $3l$-vector, B_i, where l is the number of bond coordination categories. This high-dimensional representation is referred to as the strain-space representation, an example of this for the 3 coordination environments shown in figure 4.3 is shown in equation 4.12. The z-axis aligned bond strain is transformed using X_l, which converts the bond-aligned strain to the $3l$-dimensional strain-space.

$$X_l B_i = \begin{pmatrix} x_1 \\ y_1 \\ z_1 \\ x_2 \\ y_2 \\ z_2 \\ x_3 \\ y_3 \\ z_3 \end{pmatrix} \tag{4.12}$$

The relationship between force and the aligned bond strain is given by equation 4.13. C is the coordination delimited elastic tensor, P_i is the inverse of R_i transformed to act upon the strain-space, and σ is the restorative force.

$$\sigma = \sum_i P_i C X_l B_i \tag{4.13}$$

An example of the $3l$-dimensional force vector for the three bond coordination environments of Au_{19} is shown in equation 4.14, colour-coding indicates how the tensors can be subdivided into the different coordination environments. It should be noted that, for the purpose of clarity, this equation neglects the P_i rotation matrix.

$$\begin{pmatrix} c_{111} & c_{112} & c_{113} & c_{211} & c_{212} & c_{213} & c_{311} & c_{312} & c_{313} \\ c_{121} & c_{122} & c_{123} & c_{221} & c_{222} & c_{223} & c_{321} & c_{322} & c_{323} \\ c_{131} & c_{132} & c_{133} & c_{231} & c_{232} & c_{233} & c_{331} & c_{332} & c_{333} \end{pmatrix} \text{ eV Å}^{-2} \begin{pmatrix} x_1 \\ y_1 \\ z_1 \\ x_2 \\ y_2 \\ z_2 \\ x_3 \\ y_3 \\ z_3 \end{pmatrix} \text{ Å} = \begin{pmatrix} f_x \\ f_y \\ f_z \\ f_x \\ f_y \\ f_z \\ f_x \\ f_y \\ f_z \end{pmatrix} \text{ eV Å}^{-1} \tag{4.14}$$

It should be noted that the elastic constants produced using this methodology are not directly equivalent to the elastic constants that are given for crystal structures, although these can be determined for the nanoparticles from the bond-aligned elastic compliance tensor. The dimensionality of the nanoparticle elastic tensor can exceed that of crystal structures, as there may be non-linear terms in greater number than in any of the crystal symmetries.

4.2.3.1 Artificial Neural Network

In order to efficiently determine the bond-centred elastic constants, a feed-forward, error back-propagation artificial neural-network (ANN) was employed. These networks allow for optimisation and approximation over noisy data and can act as a non-linear solver, efficiently implementing gradient descent to determine the values of the elastic tensor, C. This approach was found to produce approximations that could be refined to an arbitrary precision through iteration. The structure of an ANN can be conceptualised as layers of nodes connected by weighted branches. The nodes themselves apply an activation function to the sum of their inputs and a bias, or constant term to be added to the sum of their input branches. This then produces an output value that is forward propagated to the next layer of the network. The layers of the neural network applied in this study can be divided into three distinct categories, the input, hidden, and output layers. For this application the inputs given to the network were the set of bond-aligned strain vectors and the forces upon the system, with the output being the bond-aligned elastic tensor, C.

```
1               model = Sequential()
2               # Add input layer
3               model.add(Dense((STRAIN_SPACE_INPUT_LENGTH),
    input_dim=(STRAIN_SPACE_INPUT_LENGTH)))
4               model.add(LeakyReLU(alpha=alpha))
5
6               # Hidden layer 1
7               model.add(Dense((2 * NUM_COORD_ENV * SPACE_DIMENSION
    * SPACE_DIMENSION)))
8               model.add(LeakyReLU(alpha=alpha))
9               model.add(Dropout(dropout))
10
11              # Hidden layer 2
12              model.add(Dense((NUM_COORD_ENV * SPACE_DIMENSION *
    SPACE_DIMENSION)))
13              model.add(LeakyReLU(alpha=alpha))
14              model.add(Dropout(dropout))
15
16              # Output Layer
17              model.add(Dense((NUM_COORD_ENV * SPACE_DIMENSION *
    SPACE_DIMENSION)))
18
```

Python Code Snippet 4.1: Artificial Neural Network Structure

The number of terms in the output layer is the number of coordination environments multiplied by the number of linearly independent force components squared.

The dimensions of the force vector must be the number of coordination environments multiplied by the number of linearly independent force dimensions.

4.2.3.2 Activation Function

The Leaky Rectified Linear Unit (L-ReLU) with $\alpha = 0.9$ was used as the activation function of the dense layers of the network. The leaky form of the rectified linear unit is used, because, unlike the rectified linear unit, the function is non-zero and continuously differentiable in the domains $x < 0$ and $x > 0$. This allows for learning to occur with input values that are negative rather than these giving outputs that are limited to zero.

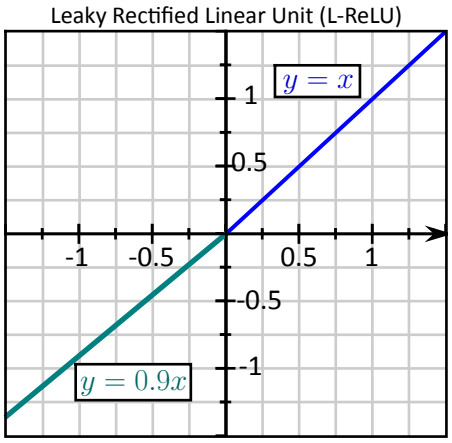

Figure 4.5: Leaky Rectified Linear Unit (L-ReLU) with $\alpha = 0.9$.

4.2.3.3 Loss and Gradient Descent

ANNs of the type utilised in this study learn through the back-propagation of errors. This is achieved by calculating a loss function, which determines the difference between the desired results and the results predicted by the network, then feeding that a fraction of the value back through the network and applying it to alter the weighting of the branches. The simplest method for calculation of the appropriate weight correction is achieved by multiplying the loss by a learning rate, to prevent oscillation of the values. The contribution of each weighted branch to the over-all loss can then be determined, which is undertaken by differentiating the activation functions and then applying these to the loss function. In practice these values also incorporate momentum terms to assist with the convergence of the network. Two optimisation functions that perform the gradient descent are utilised in this study, namely the ADAM optimiser and the ADAMAX optimiser. These were selected during the tuning process as being the most efficient available methodologies.

The custom loss function determines the accuracy of the network and provides the values used to correct the weights. The loss function created for evaluating this tensor data is shown in snippet 4.2. It fits the output of every iteration against the entire dataset in order to reduce potential issues with over-fitting of the network to

the individual geometries of the dataset. The loss of the network is evaluated based upon the characterisation of the stress—strain relationship for all geometries despite being predicted by the neural-network based upon an individual geometry. Fitting the bond-aligned tensor against the entire dataset in order to calculate loss avoids issues with the under-determination of the terms of the elastic tensor for an individual geometry and, combined with batching the updates to the network weights, this ensures that the network produces accurate elastic tensors without over-fitting to individual geometries.

The loss function applies the tensor to all strained geometries, determines the forces, and then returns the loss as the sum over all geometries of the mean squared error in the Cartesian aligned forces.

```
1                def custom_loss_function(strain_force, tensor):
2                # Unpack strain vectors and force
3                strain = strain_force[0:, 0:len_strain]
4                force = strain_force[0:, len_strain: len_strain +
    len_force]
5                # Determine the number of structures in the batch
6                num_structures = len(strain)
7                # Reshape the strain to separate the strain vectors
8                strain = tf.reshape(strain, [num_structures,
    STRAIN_VEC_COUNT,STRAIN_SPACE_VECTOR_LENGTH])
9                # Unpack the inverse rotation matrices
10               rotation = strain_force[0:, len_strain + len_force:]
11               # Reshape them for the vectors
12               rotation = tf.reshape(rotation, [num_structs,
    STRAIN_VEC_COUNT, SPACE_DIMENSION, SPACE_DIMENSION])
13               # Shape the tensor produced by the ANN
14               tensor_2 = keras.backend.reshape(tensor,
    [num_structs, SPACE_DIMENSION, SPACE_DIMENSION * NUM_COORD_ENV])
15               # Duplicate the tensor for each vector of each
    structure
16               tensor_2 = tf.expand_dims(tensor_2, axis=1)
17               tensor_2 = tf.repeat(tensor_2, STRAIN_VEC_COUNT,
    axis=1)
18               # Apply tensor to each vector of each structure
19               y_guess = tf.linalg.matvec(tensor_2, strain)
20               # Apply the inverse rotation
21               rot_force = tf.linalg.matvec(rotation, y_guess)
22               # Sum the forces for each structure
23               sum_rot_force = keras.backend.sum(rot_force, axis=1,
    keepdims=False)
24               # Calculate the mean square error
25               losses = keras.backend.square(sum_rot_force   force)
26               loss = keras.backend.mean(losses, axis=0)
27               # Sum the errors for each structure
28               loss = keras.backend.sum(loss, axis=0)
29               return loss
```

Python Code Snippet 4.2: Custom Loss Function

4.2.3.4 Tuning ANN Hyperparameters

Hyperparameters of the network, such as the layer size (dynamically determined as is shown in Python snippet 4.1), learning rate, dropout (0.1), and the alpha component (0.9) of the activation function, were tuned using the Keras optimiser. However, it was found that additional manual tuning of the batching, learning rate, and epoch length through a process of trial and improvement increased the efficiency of the convergence. Producing a high initial rate of loss minimisation was found to provide greater efficiency in the overall rate of loss minimisation, with these results converging to sufficient accuracy more quickly than the Keras-determined hyperparameters.

For the initial phase of training it was determined that the learning rate was most efficient when increased to the maximum value that did not result in divergence during the initial step. The batching was also increased in order to produce an average over all of the geometries, although this was found to be less significant than the learning rate. The epoch length was limited based upon the loss value, when the loss was low enough that the learning rate could be efficiently decreased to improve the accuracy of the results the epoch was ended and a new epoch with a lower learning rate introduced. The final learning rate, epoch length, and batch size that were determined to efficiently produce an accurate tensor for the Au_{19} system are quoted in the results section below.

4.2.3.5 Example Tensor

A set of ten distorted Au_{19} structures were created from an optimised cluster. The magnitude and directions of the displacements applied were randomly determined but constrained to within 1 Å of the equilibrium structure.

In order to examine the accuracy of the neural network in the evaluation of tensors of known value, several test cases were generated. These tensors, C_n, were populated with random values and applied to the strain vectors of the distorted geometries to give forces against which the network could be trained. The dimensions of the tensors were of dimension $E \times D$, where $E = 3$, the number of coordination environments, and $D = 3$, the number of linearly independent spatial dimensions.

As is shown in equation 4.15, the first test tensor was populated along the primary diagonal with random values between 0—1. This tensor replicates a stress-strain relationship that can be characterised by the linear displacement of the bond vectors in the x, y, and z-axes.

The forces for this tensor were then calculated for the strained geometries and these were then used to train the network until it converged with a loss that was measured to be less than 1×10^{-10} at the end of an epoch.

The absolute error, δ_{C_1} as shown in equation 4.16, was calculated by subtracting the predicted tensor from the actual tensor. It was found that the largest errors,

those greater than 0.0001, occur in the xy-plane about the diagonal. This suggests that further convergence would likely reduce these errors. The relative percent error, *RPE* as is shown in equations 4.17 and 4.18, reports a maximum error of 0.9% with a mean *RPE* of 0.1% across the whole tensor. It should be noted that, as these displacements occur symmetrically about the z-axis and are of equal magnitude but inverse sign, these errors can be considered to cancel when symmetry considerations are considered. These errors can be expected to tend to zero with an increased number of convergence cycles.

$$C_1 = \begin{pmatrix} 0.085 & 0.000 & 0.000 & 0.256 & -0.004 & 0.000 & 0.863 & 0.009 & 0.000 \\ 0.000 & 0.862 & 0.000 & 0.004 & 0.569 & 0.000 & -0.009 & 0.476 & 0.000 \\ 0.000 & 0.000 & 0.176 & 0.000 & 0.000 & 0.014 & 0.000 & 0.000 & 0.296 \end{pmatrix} \text{ eV Å}^{-2} \tag{4.15}$$

$$\delta_{C_1} = \begin{pmatrix} 0.0001 & 0.0000 & 0.0000 & 0.0000 & 0.0044 & 0.0000 & 0.0001 & 0.0089 & 0.0001 \\ 0.0000 & 0.0000 & 0.0000 & 0.0044 & 0.0001 & 0.0000 & 0.0088 & 0.0000 & 0.0000 \\ 0.0001 & 0.0000 & 0.0000 & 0.0000 & 0.0000 & 0.0001 & 0.0000 & 0.0000 & 0.0001 \end{pmatrix} \text{ eV Å}^{-2} \tag{4.16}$$

$$\textit{RPE} = \frac{|C_{trueij} - C_{calcij}|}{1 + |C_{trueij}|} \tag{4.17}$$

$$\textit{RPE}(C_1) = \begin{pmatrix} 0.0\,\% & 0.0\,\% & 0.0\,\% & 0.0\,\% & 0.4\,\% & 0.0\,\% & 0.0\,\% & 0.9\,\% & 0.0\,\% \\ 0.0\,\% & 0.0\,\% & 0.0\,\% & 0.4\,\% & 0.0\,\% & 0.0\,\% & 0.9\,\% & 0.0\,\% & 0.0\,\% \\ 0.0\,\% & 0.0\,\% & 0.0\,\% & 0.0\,\% & 0.0\,\% & 0.0\,\% & 0.0\,\% & 0.0\,\% & 0.0\,\% \end{pmatrix} \tag{4.18}$$

A second tensor was created from random numbers in the range 0—101, shown in equation 4.19. From the absolute error, given in equation 4.21, it can be observed that the errors across the calculated tensor, A_{100} in equation 4.19, are within the same order of magnitude as the true terms, C_{ij}. This shows how a large variance across the force magnitude can result in constant errors. This can be corrected somewhat by dividing the forces by a constant term before analysis.

$$C_{100} = \begin{pmatrix} 98.20 & 29.33 & 85.60 & 21.99 & 81.26 & 68.88 & 2.60 & 36.89 & 40.10 \\ 39.61 & 101.12 & 32.53 & 80.04 & 3.96 & 4.36 & 38.06 & 2.36 & 12.17 \\ 39.87 & 2.15 & 86.75 & 93.22 & 78.48 & 79.17 & 21.069 & 42.83 & 16.57 \end{pmatrix} \text{ eV Å}^{-2} \tag{4.19}$$

$$A_{100} = \begin{pmatrix} 99.32 & 29.91 & 86.51 & 22.97 & 81.41 & 69.21 & 1.54 & 38.02 & 39.84 \\ 39.93 & 100.72 & 32.95 & 81.41 & 3.04 & 4.18 & 38.02 & 1.36 & 12.86 \\ 40.68 & 2.07 & 86.92 & 93.34 & 78.51 & 79.61 & 20.21 & 42.60 & 18.54 \end{pmatrix} \text{ eV Å}^{-2} \tag{4.20}$$

$$\delta_{C_{100}} = \begin{pmatrix} 1.111 & 0.575 & 0.919 & 0.980 & 0.153 & 0.328 & 1.053 & 1.126 & 0.268 \\ 0.323 & 0.398 & 0.421 & 1.367 & 0.924 & 0.184 & 0.043 & 1.000 & 0.693 \\ 0.811 & 0.079 & 0.162 & 0.122 & 0.035 & 0.436 & 0.855 & 0.224 & 1.968 \end{pmatrix} \text{ eV Å}^{-2} \tag{4.21}$$

$$\mathit{RPE}(C_{100}) = \begin{pmatrix} 1.1\,\% & 1.86\,\% & 1.1\,\% & 4.1\,\% & 0.2\,\% & 0.5\,\% & 41.4\,\% & 2.9\,\% & 0.7\,\% \\ 0.8\,\% & 0.4\,\% & 1.2\,\% & 1.7\,\% & 22.9\,\% & 3.6\,\% & 0.1\,\% & 42.3\,\% & 5.0\,\% \\ 2.0\,\% & 2.6\,\% & 0.2\,\% & 0.1\,\% & 0.0\,\% & 0.5\,\% & 4.0\,\% & 0.5\,\% & 10.1\,\% \end{pmatrix} \tag{4.22}$$

4.2.3.6 Computational Details

Structures were created through random distortions of the optimised Au_{19} geometry and the forces upon these geometries were calculated using the VASP implementation of periodic density functional theory.[52–55] The PBE exchange-correlation functional with D3BJ dispersion correction was employed with an energy cut-off for the plane wave basis of 400 eV. The electronic relaxation for the self-consistency was selected to be 10^{-6} eV.[46] A $1 \times 1 \times 1$ k-point grid was used for the nanoparticle with a Monkhorst-Pack grid applied to the sampling of the Brillouin zone.[89] A 24 Å vacuum gap was used to prevent self interaction.

Of the random displacements, three structures were excluded as the magnitude of the forces indicated that length of displacements distorted the structure beyond the elastic limits. The force upon each structure was calculated relative to the unstrained geometry as described above.

4.3 Results and Discussion

4.3.1 Characterisation of Bonding

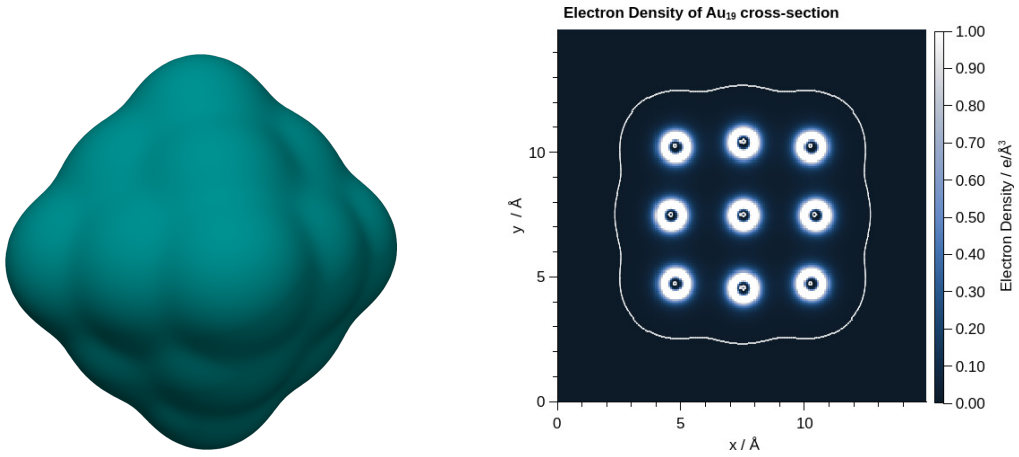

(a) (b)

Figure 4.6: Electron density of Au_{19} showing the 99.9% confidence surface (a) and a cross-section of the electron density through the plane bisecting 4 vertex atoms with the 99.9% van der Waals surface indicated as a white line.

Insight into how small nanoparticles exhibit activity and properties that are so distinct from bulk gold can be obtained through analysis of the surface properties of small nanocrystalites. The van der Waals surface, the 99.9% confidence isosurface of the electron density shown in figure 4.6, mapped with the average local ionisation energy (ALIE) indicates the differences with which electrons may be extracted from the molecular surface. In particular this indicates that the electrons in general are relatively weakly bound and also that the regions of electron density which corresponds with the edges of the nanocrystallite are where electrons are most easily extracted from the surface, as is shown in figure 4.7b. This indicates that these edge sites are more likely to be sites of electrophilic attack and are the most probable locations of reaction sites for electrophilic reactants. Examination of the ALIE also indicates that the vertex sites of the nanocrystallite show a relative favourability towards nucleophilic species.

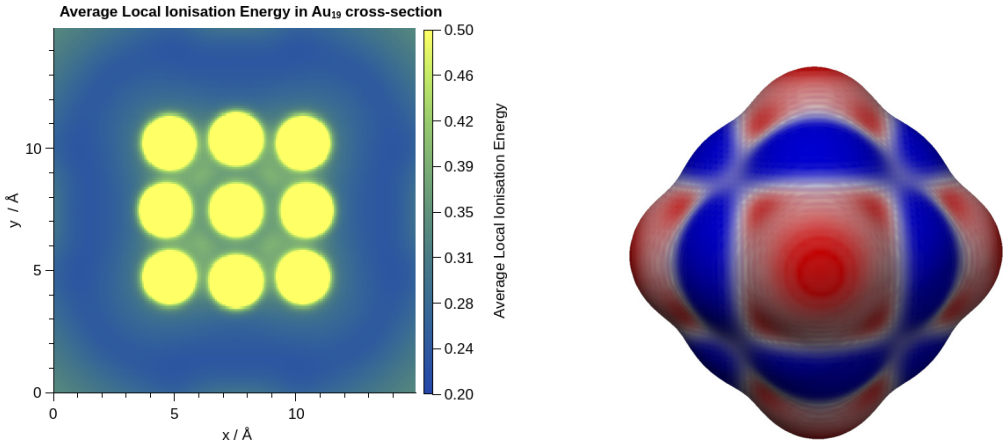

(a) (b)

Figure 4.7: Au_{19} average local ionisation energy.

The character of the electronic structure was further investigated through examining the metallicity and locality of the electrons. The cross-sectional planes, shown in figures 4.8 and 4.9 where a greater value indicates more metallic character, show a high degree of metallicity, which suggests a high density of states, a large extent of electron delocalisation, and low localised electron momentum density. It was found that the dimensionless metallicity, as proposed by Ayers and Jenkins, allowed for easier analysis of the metallic character of the nanoparticles, as is shown in figure 4.9. The highly delocalised nature of the electronic structure is further supported by examination of the localised orbital locator function, shown in figure 4.10b. The localized orbital locator function shows localisation where LOL(r) > 0.5, however, for the bonds within the Au_{19} nanocrystallite, it can be observed that, aside from electrons that are considered within the core of the atom, the electron density is largely delocalised with specific regions of slightly greater localisation between the atoms. This indicates a substantial delocalisation of the electronic structure which is also supported by an examination of the regions of slow electrons (RoSE), figure 4.10a. Higher values of RoSE indicate regions in which electrons spend a significant amount of time and lower values indicate greater non-locality. As the RoSE shows, the electrons within Au_{19} are relatively fast moving and, as such, spend little time localised into bonding regions. From the LOL, RoSE, and metallicity it can be understood that Au_{19} shows significant delocalised metallic character; however, in comparison to the facets and other surface regions of the cluster, the internal region of the cluster actually shows relatively lower metallicity and delocalisation. This is indicative of an inequivalence in the bonding environments of the gold atoms and suggests an inhomogeneity consistent with that shown by the average local ionisation energy, allowing Au_{19} to show particular

catalytic activity whilst also having a relatively high proportion of the surface area being the more active edge and vertex sites. The relative lability of the easily ionisable electrons present at the vdW surface also correlates well with the experimental evidence that shows smaller nanocrystalites to be disproportionately effective catalysts in comparison to larger nanoparticle species. The metallicity, LOL, and RoSE also indicate that these sites are diffuse and delocalised with significant metallic character, a high density of states contributing to the electron density in comparison to molecular systems. The proximity of these sites to regions favouring electrophilic species indicates how these clusters can act catalytically by binding reactants such that they are within small distances.

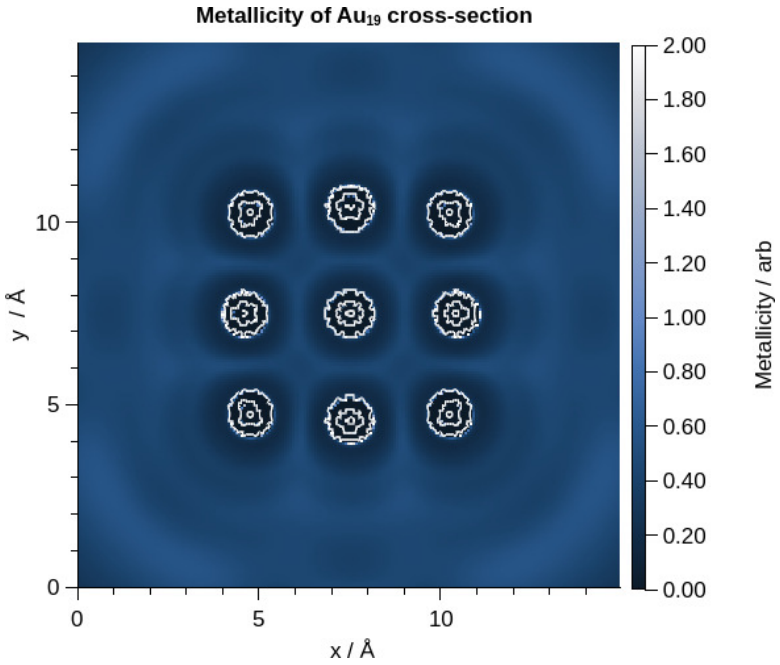

Figure 4.8: Metallicity of Au_{19}.

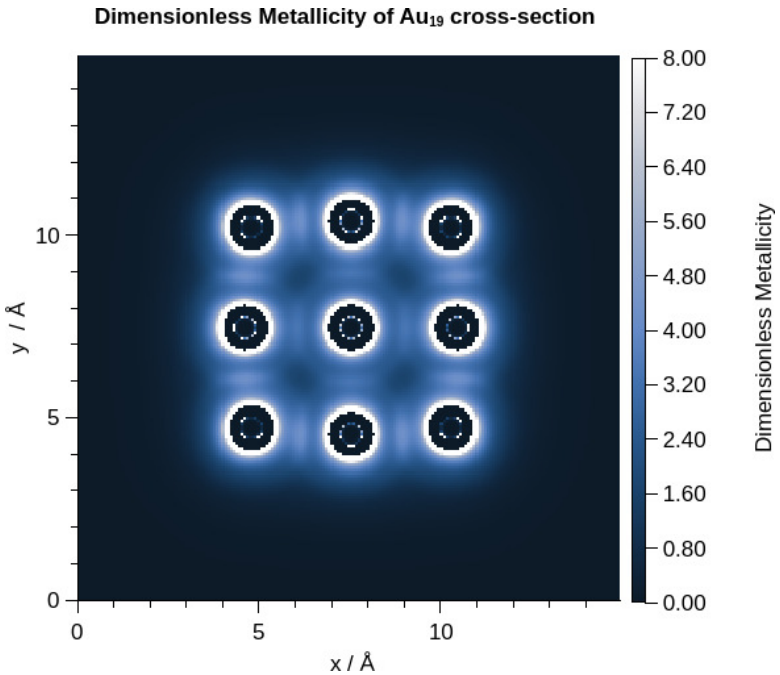

Figure 4.9: Dimensionless Metallicity of Au_{19}.

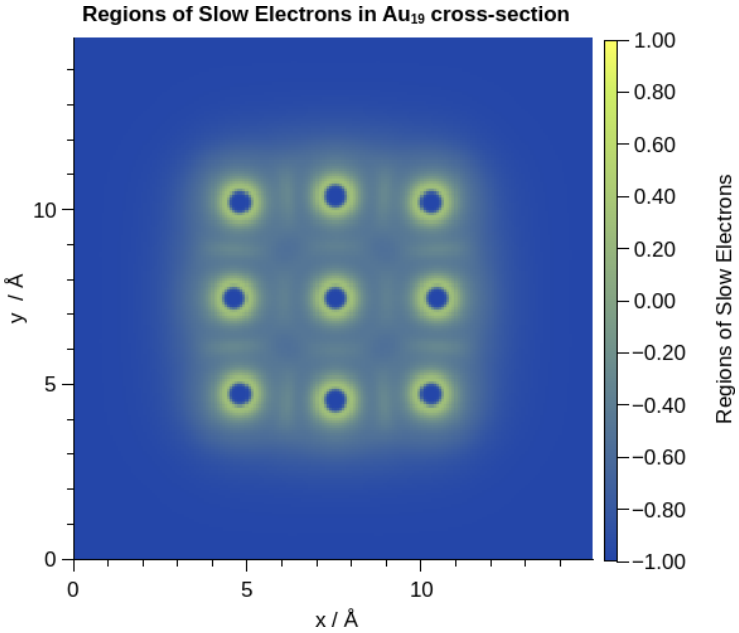

(a) Regions of Slow Electrons Au_{19}.

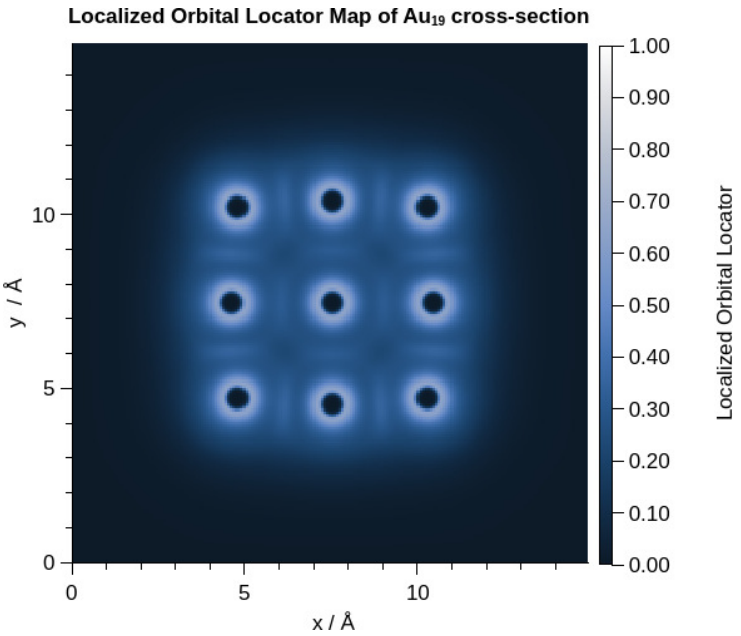

(b) Localised Orbital Locator Au_{19}.

Figure 4.10: Au_{19} RoSE and LOL cross sections.

Comparison of equivalent sized facets with molecular gold species, where molecular gold is understood to mean structures in which a metal-like coherent band structure cannot be observed, also shows some notable differences in property. For the purposes of this case-study, Au_6, shown in figure 4.11 was utilised for this comparison, as it can be directly contrasted with the trigonal facets of Au_{19}. Application of topological analysis based upon the quantitative theory of atoms in molecules, QTAIM, allowed for descriptors to be evaluated at the critical points of the electron density. Here bond critical points (BCPs), saddle points where the gradient norm of the electron density is zero and two eigenvalues of the Hessian matrix are negative (3, -1), will be focussed upon in particular, as these regions are found to correlate well with the traditional notions of the chemical bond.

Figure 4.11: Au_6 gold molecule.

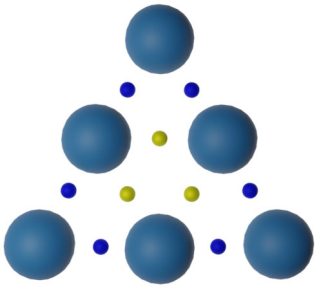

Figure 4.12: Critical points of Au_6. Large spheres correspond to $(3,-3)$ nuclear critical points, small spheres are $(3,-1)$ critical points (Yellow indicates points within the facet, dark blue indicates edge critical points)

Bond Critical Point Type			Dimensionless Metallicity	Localised Orbital Locator
Facet	(Edge—Edge)	$(3,-1)$	3.89	0.33
Edge	(Corner—Edge)	$(3,-1)$	5.76	0.37

Table 4.1: Critical points for Au_{19} with the values of dimensionless metallicity and the localised orbital locator values for the critical points.

Examination of the BCPs of Au_6 showed two distinct types in terms of both the metallicity and localisation, as is shown in table 4.1. Edge atom—corner atom and edge atom—edge atom bonds, labelled respectively as Facet and Edge and shown as yellow and blue small sphere in figure 4.12. These BCPs indicated significant differ-

ences in metallicity and localisation of the constituent electrons within the bonds of Au_6, with the Facet bonds being more diffuse and delocalised with significantly less metallic character than the Edge bonds.

In comparison to the Au_6, Au_{19} BCPs indicate three distinct regions of bonding, the Facet and Edge bonds similar to those found in Au_6 and additional internal bonds between the edge atoms and the nanoparticle core atom. The critical points, although showing a similar pattern in relative metallic character and localisation as the molecular gold species, show reduced metallicity and a greater delocalisation than Au_6. The decreased metallicity indicates a more covalent character and a decrease in the density of states for the Edge and Facet bonds. It is noteworthy that this does not appear to be an artefact of the atom-centred DFT methodology, as the density of states were found to be consistent with the electronic structure predicted by periodic, plane-wave DFT.

Bond Critical Point Type			Dimensionless Metalicity	Localised Orbital Locator
Facet	(Edge—Edge)	$(3,-1)$	3.40	0.32
Edge	(Corner—Edge)	$(3,-1)$	4.25	0.35
Internal	(Edge—Core)	$(3,-1)$	3.38	0.31

Table 4.2: Critical points for Au_{19} with the values of dimensionless metallicity and the localised orbital locator values for the critical points.

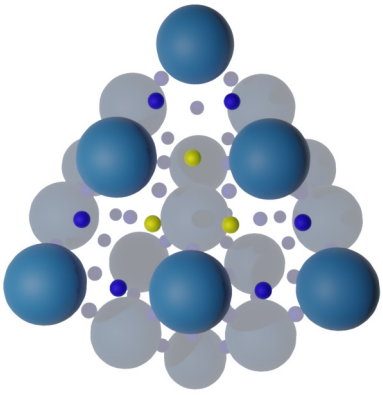

Figure 4.13: Critical points of Au_{19} facet. Large spheres correspond to $(3,-3)$ critical points, small spheres are $(3,-1)$ critical points (Yellow indicates points within the facet, dark blue indicates edge critical points).

Although the reduction in metallic character of the surface bonds in Au_{19} may appear to be a decrease in metallicity, examination of the dimensionless metallicity actually reveals this to be better considered as a shift of metallic character towards the surface of the species. The dimensionless metallicity of Au_6 and a facet of Au_{19}, figure 4.14, clearly shows the decreased metallicity in the internal bonding of the Au_{19} facet relative to the molecular gold, as well as the increase in metallic character of the region around the vertices and edges of the facet. It can be observed that the metallic character extends further from the facet of the nanoparticle than it would for the Au_6 molecular gold species.

Comparison of the RoSE for the Au_{19} facet and Au_6 molecular species, shown in figure 4.15, indicates that the electrons are more diffuse with fewer local regions of slow electrons. However, similarly to the metallicity, regions of slow electrons can be observed to extend further into space for the Au_{19} than the Au_6. This suggests that the more readily ionisable electrons, which are from a high number of contributory states, spend more time at the edges of the Au_{19} facets than they do at the edges of the molecular gold species. This inhomogeneity suggests a lability that would be an important contributory factor to the increased relative propensity of small gold nanoparticles to be effective catalysts, with high reactivity in comparison to the bulk materials and molecular species.

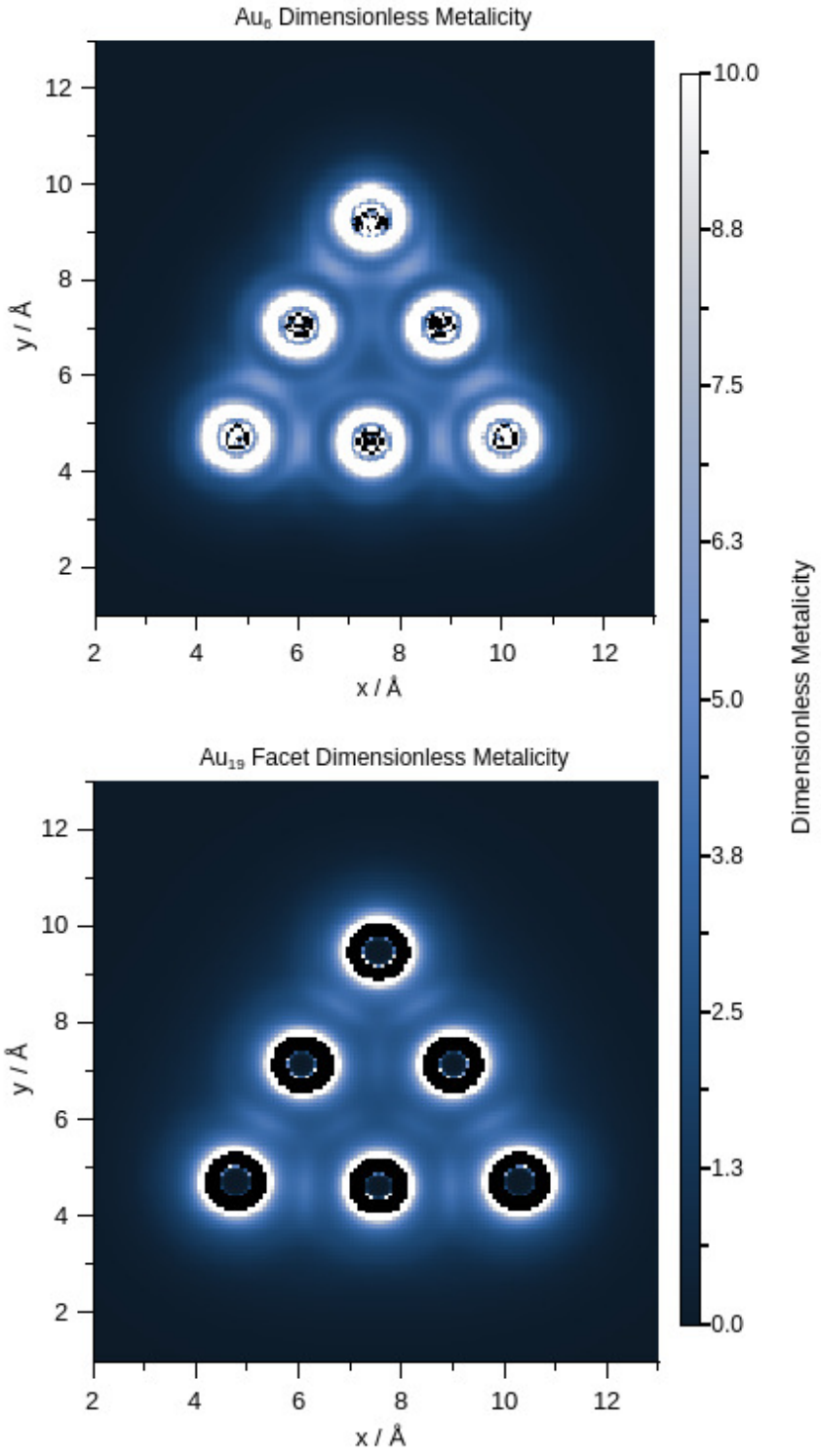

Figure 4.14: Dimensionless Metallicity of Au_6, upper, and a facet of Au_{19}, lower.

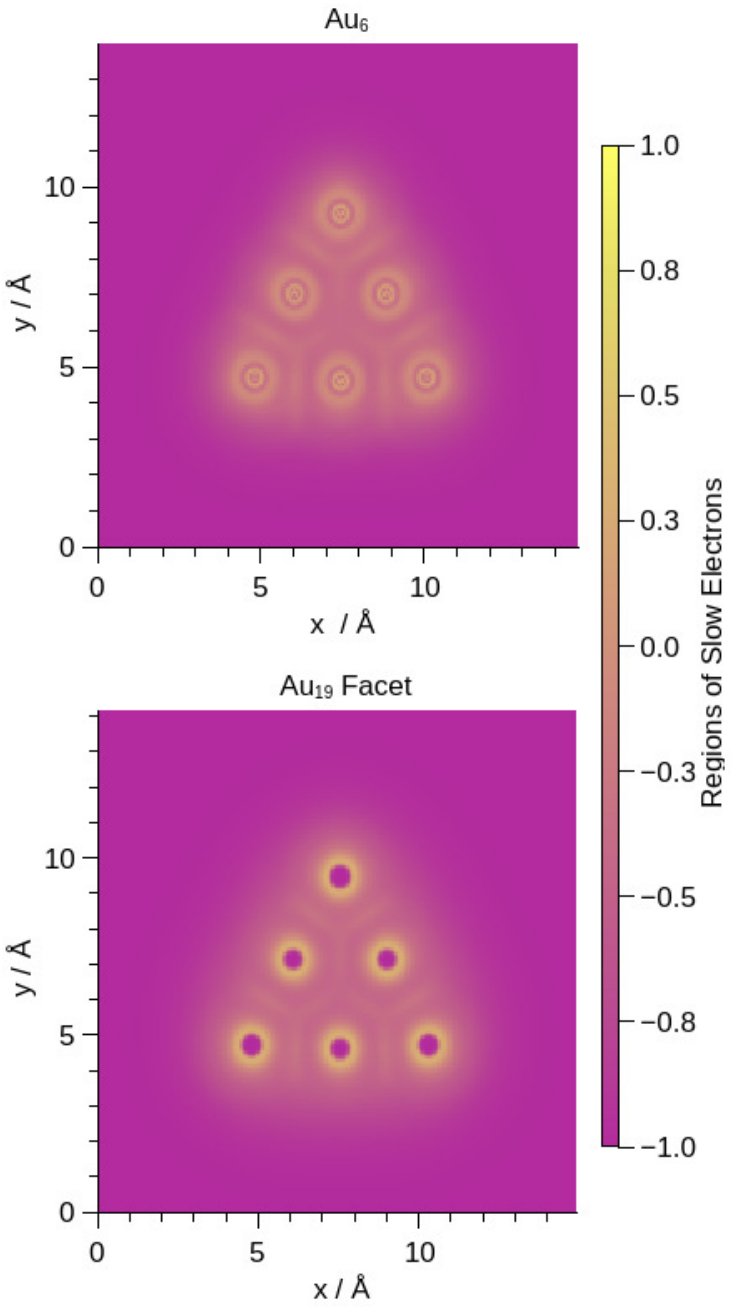

Figure 4.15: Regions of Slow Electrons, RoSE Au_6, upper, and a facet of Au_{19}, lower.

Examining critical points other than the bond critical points also shows how metallic character of the facets is decreased relative to the equivalent surface on Au_6. The $(3,+1)$ ring critical points, shown as red spheres in figure 4.16, show a lower metallicity and a decrease in the RoSE value for Au_{19} relative to the Au_6. The most metallic critical points for the Au_{19} are the bond critical points linking the vertex and edge atoms of the facet. In comparison to Au_6, Au_{19} shows decreased metallicity for all comparable bonds.

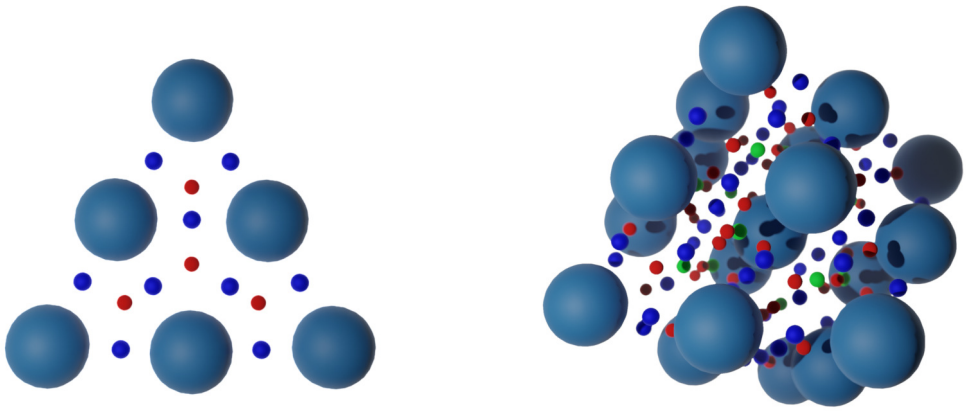

(a) (b)

Figure 4.16: All critical points in the electron densities of Au_6 (a) and Au_{19} (b). Large spheres correspond to atoms or $(3,-3)$ critical points; bond critical points, $(3,-1)$, are indicated with small blue spheres; ring critical points, $(3,+1)$, are red spheres; and cage critical points are indicated by green spheres, $(3,+3)$.

Critical Point Type			$\overline{\text{RoSE}}$	$\overline{\text{Dim. Metallicity}}$
Bond	(Edge—Core)	$(3,-1)$	-0.374	3.376
Bond	(Edge—Edge)	$(3,-1)$	-0.361	3.402
Bond	(Corner—Edge)	$(3,-1)$	-0.302	4.247
Ring	(Facet Centre)	$(3,+1)$	-0.426	2.535
Ring	(Internal)	$(3,+1)$	-0.419	2.737
Ring	(Facet Edge)	$(3,+1)$	-0.374	3.055
Cage	(Tetrahedral)	$(3,+3)$	-0.441	2.408
Cage	(Octahedral)	$(3,+3)$	-0.543	1.658

Table 4.3: Critical points for Au_{19} with the values for Regions of Slow Electrons, RoSE, and dimensionless metallicity.

Critical Point Type			$\overline{\text{RoSE}}$	$\overline{\text{Dim. Metallicity}}$
Bond	(Edge—Edge)	$(3,-1)$	-0.34278	3.8908
Bond	(Corner—Edge)	$(3,-1)$	-0.25931	5.7621
Ring	(Facet Centre)	$(3,+1)$	-0.38588	2.7978
Ring	(Facet Edge)	$(3,+1)$	-0.31562	3.5920

Table 4.4: Critical points for Au_6 with the mean values for regions of slow electrons and dimensionless metallicity.

The radial distribution function of the dimensionless metallicity, shown in figure 4.17, measures the average metallicity as a function of distance from the geometric centre. The low metallicity values in the region 0.8 Å to 2 Å indicates that, rather than metallic character being distributed throughout the cluster, the high density of states is concentrated between the atoms of the surface of the cluster with the electron density in the centre of the cluster being dominated by the core atom, which causes a low density of states and, therefore, a low metallicity score. The average interaction between the core and the surface shows little metallic character, which indicates that the regions with the highest density of states around the Fermi level are close to the surface.

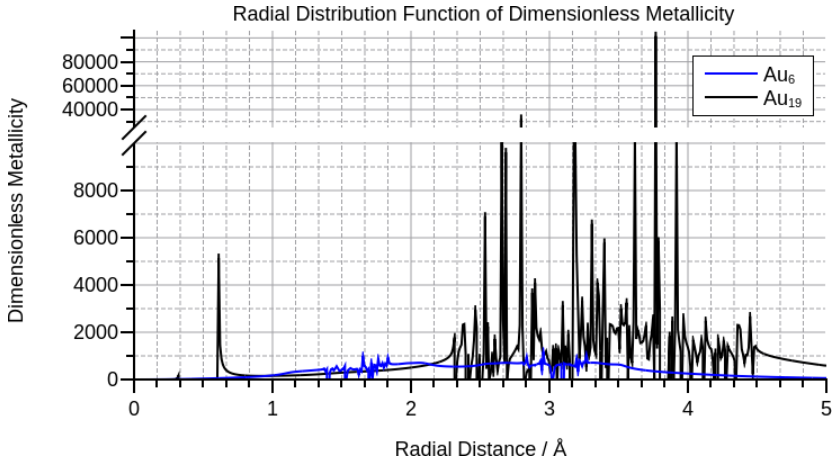

Figure 4.17: Radial metallicity of Au_6 and Au_{19}.

That the bonds between the core and surface atoms show a distinct character in comparison to the vertex—edge atom bonds is also supported by analysis of both the LOL and the non-covalent interactions (NCI), shown in figure 4.18 as defined by equations 4.10 and 4.9. Vertex—Edge bonds show largely covalent character in both the LOL and NCI surfaces. This can be observed as holes through the NCI surface and ellipsoids within the LOL surface diagram. Blue surface regions in NCI indicate non-covalent bonding character; this can be observed to be present around the covalent regions but also as the primary bonding interaction in the edge — edge and edge — core bonds. The NCI surface also indicates a red region of destabilising repulsive in-

teraction between the vertex and core atoms, where the sign of λ_2 is positive.

Consistent with the high metallicity found at the bond critical points, bonding within the Au_{19} cluster is also found to show relatively low levels of localisation, indicated by the small size of the ellipsoids in figure 4.18a. The ellipsoid regions were found to be more consistent with covalent bonding, a conclusion which is supported by the holes in the NCI surface as shown in figure 4.18b, but are surrounded by non-covalent attractive bonding density. When combined with the measure of localisation and metallicity, this indicates that these attractive regions are delocalised with a high density of states contributing to them, indicating metallic character. However, despite the high degree of metallic character, a high density of states does not necessarily imply charge carrier mobility, so this should not be interpreted to suggest a continuous band structure similar to that of the bulk material.

The data produced by these descriptors are consistent with the bonds within the cluster being a combination of covalent and metallic bonding regions that defy simple classification as either metallic or covalent bonds. An inherent limitation of the local measures used in this study is the reduced accuracy with which long range phenomena such as delocalisation can be examined, however, as this analysis is supported by multiple measures that characterise non-covalent interaction, localisation, and metallicity, the conclusion that there is a mixed covalent-metallic bonding between the gold atoms of the Au_{19} cluster is well-supported despite other relevant properties such as delocalisation not being directly examined.

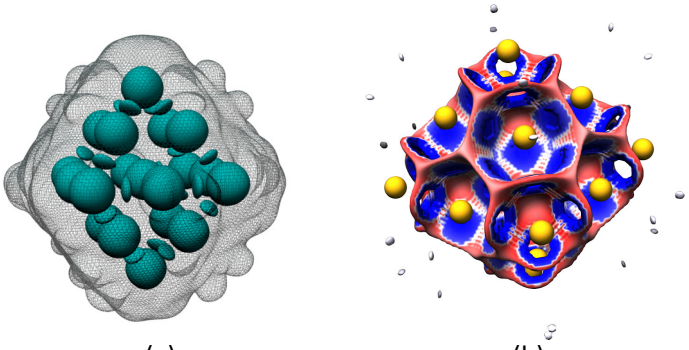

(a) (b)

Figure 4.18: Plots of bonding interactions using the 0.7 isosurface of the localised orbital locator shown within a mesh of the van der Waals surface (a) and the reduced density gradient 0.5 isosurface mapped with sign$(\lambda_2)\rho$ (b), which shows non-covalent interactions. (Red indicating positive repulsive interactions and blue indicating negative attractive interactions.)

Molecular gold (Au_6) is significantly more covalent in character than the small nanoparticle species, which is supported by comparison of the non-covalent interactions shown in figure 4.19. It can be observed that although non-covalent interactions still play a significant role within the Au_6 structure, the nanoparticle species has a greater reliance upon these to stabilise the structure, as shown by a greater number and magnitude of the stabilising interactions for the cluster, where sign$(\lambda_2)\rho < 0$. The higher proportion of these interactions shows that the nanoparticle has a much greater influence from attractive non-covalent character than the molecular species. Although similar non-covalent interactions can be observed for the two geometries, Au_{19} has a much broader range of stabilising attractive non-covalent bonding (sign$(\lambda_2)\rho < 0$) than the molecular gold. The NCI plot also shows significantly greater amounts of repulsive interactions for the nanocrystallite in comparison to the molecular species.

Plotting the local orbital locator, reduced density gradient and sign$(\lambda_2)\rho < 0$ allows for a closer examination of the type of interactions present in the Au_{19} species, shown in figure 4.20. From this it can be observed that, as the reduced density gradient tends to 0 the attractive stabilising interactions, sign$(\lambda_2)\rho < 0$, tends towards values of approximately 0.33, which is consistent with the edge—edge values found for the bond critical points. Although these regions have significant covalent bonding character, the NCI analysis further supports that they are also attractive through delocalised non-covalent interactions and do not display significant covalent character.

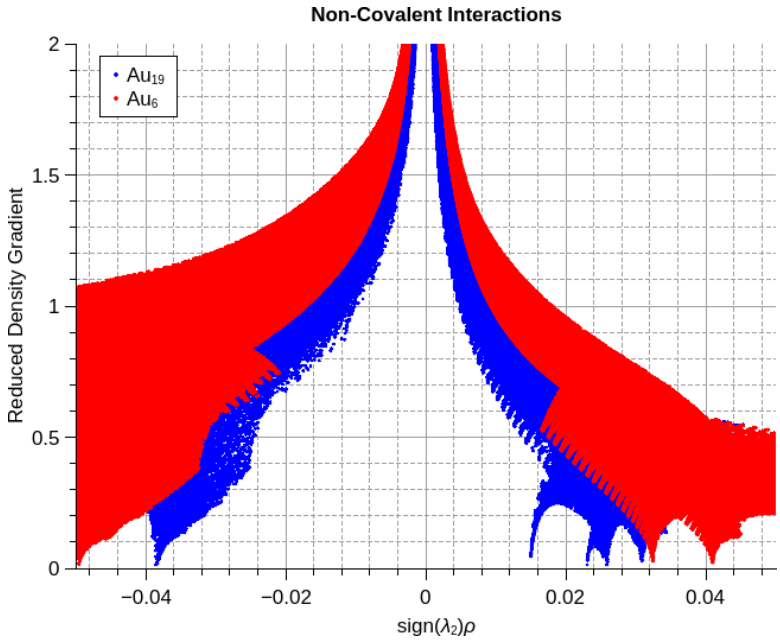

Figure 4.19: Plot of the Reduced Density Gradient, RDG, against sign$(\lambda_2)\rho$, showing non-covalent interaction.

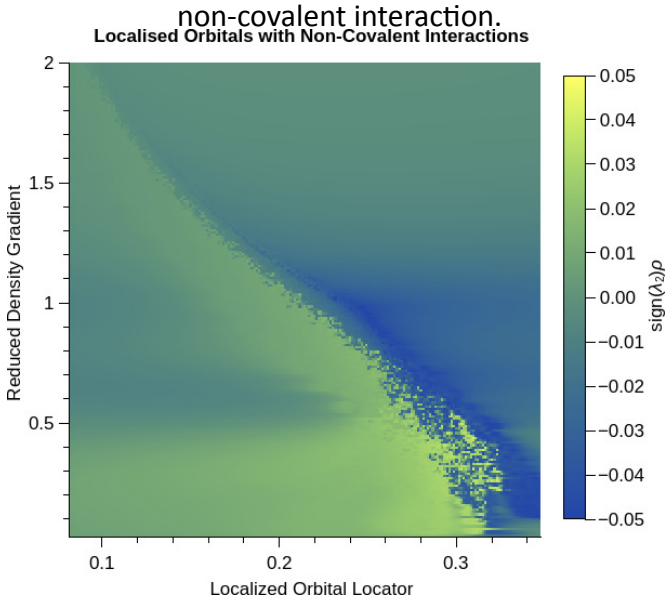

Figure 4.20: Map of the Reduced Density Gradient, Localised Orbital Locator and sign$(\lambda_2)\rho$ values.

4.3.2 Elastic Bond Distortion Within Au_{19}

The stress calculated for each directional component of the 7 distorted geometries, produced using random displacements of a magnitude less than 1 Å, is shown in figure 4.21. The tensor used to calculate these forces, shown in equation 4.23, was converged using a batch size of the entire 7 structures and two training epochs. The first being 50,000 iterations and the second having a maximum of 6,000,000 steps, although a cut-off when the loss reached 1×10^{-12} was employed. The stress upon each

structure was then calculated using equations 4.13 and 4.11. As can be observed in the plot shown in figure 4.23, for the first iteration of the ANN, despite the z component of the σ_1 forces showing a significant error, the general quality of the approximation of the tensor was very high. As is shown in figure 4.22, there was significant agreement between the predicted and measured forces and, excluding the anomalous value for σ_1, the values conform to $y = 1.00x + 0.000$ with a coefficient of determination $R^2 = 1.000$. This suggests that the batching over a large proportion of the dataset can result in tensor fitting that does not necessarily satisfy all terms of the data or cannot be accurately characterised with a dataset of this small size and random character.

$$\overline{C} = \begin{pmatrix} 0.152 & 0.300 & 0.014 & 0.190 & -0.166 & -0.194 & 0.077 & -0.742 & 0.033 \\ -0.115 & 0.170 & 0.013 & 0.282 & 0.012 & -0.156 & -0.602 & 0.017 & 0.322 \\ -0.090 & 0.176 & -0.222 & -0.415 & -0.098 & 0.157 & -0.014 & -0.797 & -0.182 \end{pmatrix} \tag{4.23}$$

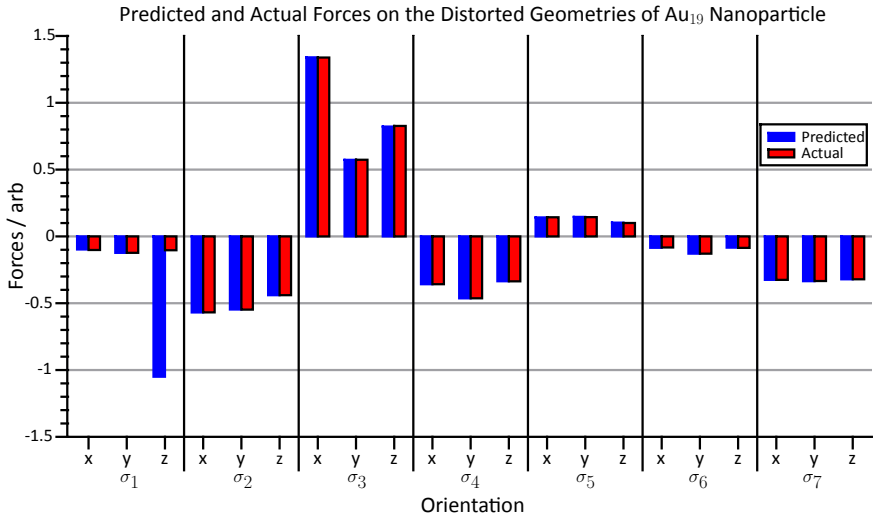

Figure 4.21: Chart showing the actual forces and predicted forces for each strained geometry with a tensor determined by a neural network with batching parameters of 7 and 7 for the first and second fitting stages.

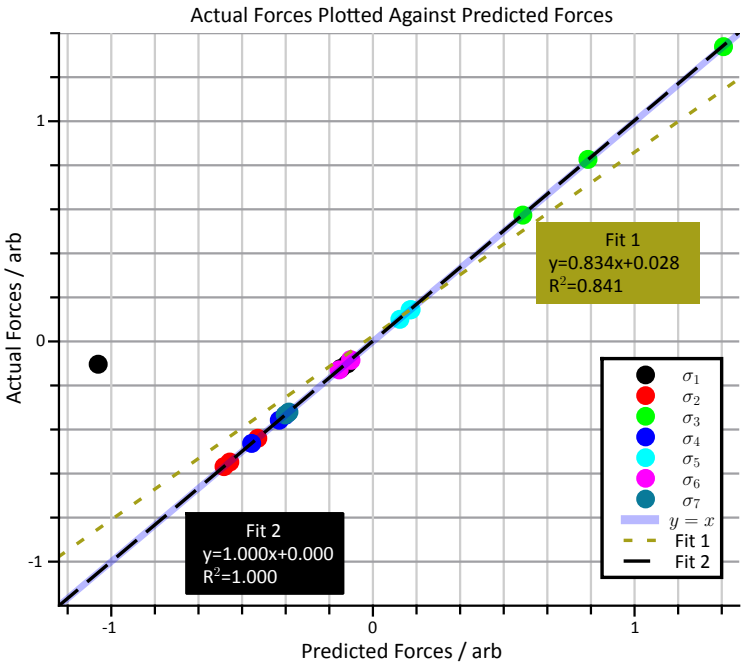

Figure 4.22: Plot of the actual forces against the predicted forces. Fit 1 is across all data, fit 2 excludes the anomalous point in σ_1.

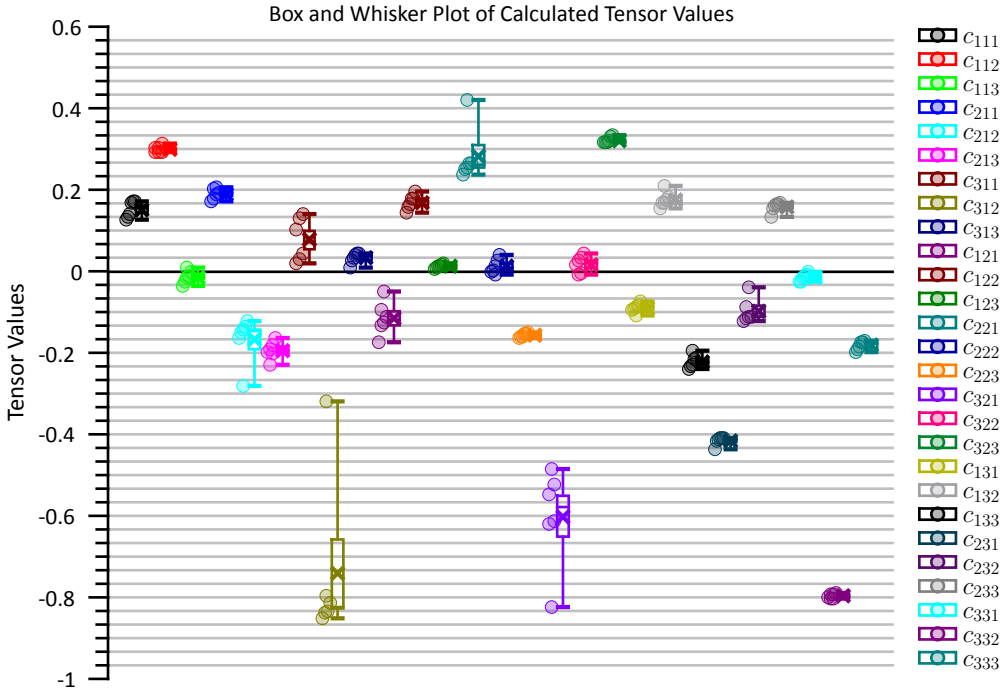

Figure 4.23: Plot of the mean tensor values. Whiskers indicate the range of the values and the boxes show the standard error and median value for each term of the mean tensor. The component data are plotted alongside.

In order to examine whether the inaccuracy arose due to methodology or dataset, the batching of the training set for the neural network was reduced. The decreased batching, where the tensor value was updated after fewer calculations of the loss function, was found to result in a tensor, equation 4.24, that perfectly comported to the actual forces found by computational experiment, shown in figures 4.24 and 4.25. The final tensor was calculated using three training runs, which was found to reduce the computational time required to produce each tensor and increase the resultant accuracy. The first had a batch size of 4 and ran for 40,000 epochs with a learning rate of 0.001, the second had a batch size of 2 with 200,000 epochs and a learning rate of 0.0001, and the third ran used a batch size of 3 with 500,000 maximum epochs, as these values were benchmarked as producing the fastest accurate convergence process during analysis of the example tensors. Two different optimisation algorithms were sequentially employed, the first being the ADAM method and the second and third training phased employed the ADAMAX function, both as implemented in the Keras Python library.

The tertiary training run network weights were then used to populate the production network and the final tensor was calculated as an average over the elements of the tensors calculated for all distorted geometries. The outputs from five training runs of the neural neural network were then averaged to produce the bond-centric elasticity tensor, equation 4.24.

$$\overline{C} = \begin{pmatrix} 0.060 & 0.383 & -0.069 & 0.241 & -0.144 & -0.109 & 0.178 & -0.691 & -0.150 \\ -0.060 & 0.133 & 0.027 & 0.169 & -0.008 & -0.158 & -0.547 & 0.369 & 0.376 \\ -0.107 & -0.112 & -0.137 & -0.335 & 0.097 & 0.223 & -0.208 & -0.682 & -0.256 \end{pmatrix} \tag{4.24}$$

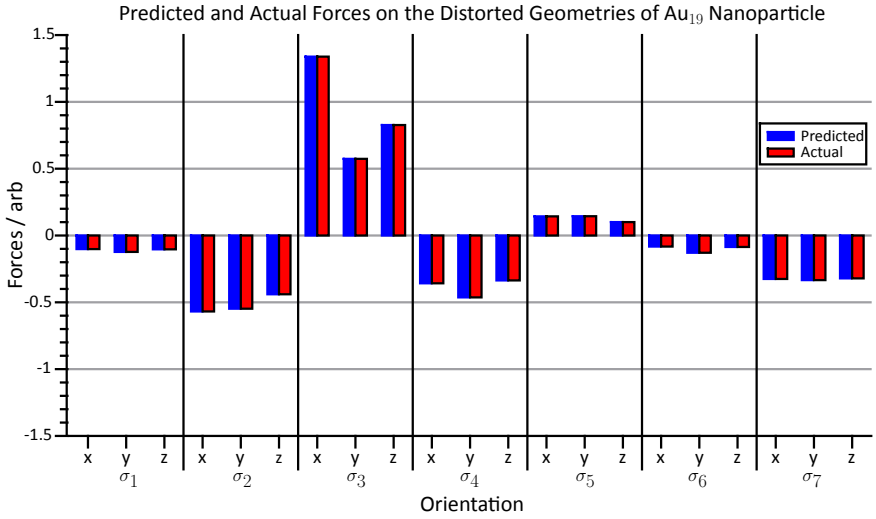

Figure 4.24: Chart showing the actual forces and predicted forces for each strained geometry.

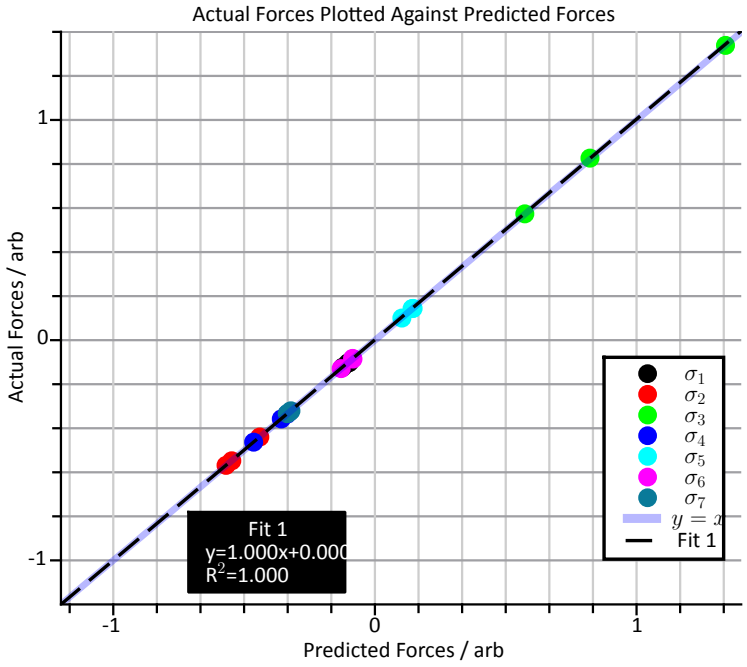

Figure 4.25: Plot of the actual forces against the predicted forces with a linear fit.

This approach provides a novel methodology for examining the elasticity of bonds within nanoparticles and presents a methodology for approximating the bond-aligned elastic tensor, which can be used to determine the forces caused by elastic deformation in inhomogeneous nanoparticle species. The inherent approximation within these tensors, that elastic constants can be defined relative to bond distortions, is acceptable as the bond aligned tensor must almost always attempt to incorporate at least two separate distortions. This can be best conceptualised by considering a bond between two atoms of inequivalent coordination environment, which is necessarily constrained within a framework, a simple bond stretch can correspond to distortions at either end of the bond and, as such, the bond-aligned tensor must be capable of incorporating all the distortion within the framework. This causes a dependence that cannot be fully decomposed into contributions from separate bonding environment.[119] However, the descriptive tensor that appropriately incorporates these deformations can still be understood as accurately characterising elasticity for the given set of structures, with a larger training set providing more accurate results. As such, these tensors can be applied in a predictive capacity for estimating the forces experienced under distortion and give a measure of the force, restorative or otherwise. That the z-terms of some tensors are positive indicates how these distortions occur with a framework and as such the individual components cannot necessarily be divorced from the changes within the wider cluster. The methodology is inherently scalable, as the network can be trivially expanded to encompass a greater number of bond coordination environments and atoms. This approach also avoids issues with over-fitting of the neural network, as the network itself serves the role of a non-linear gradient descent mechanism capable of handling noisy data and so must converge upon an appropriate tensor output that satisfies all data simultaneously.

4.4 Conclusions

This chapter presents a detailed characterisation of the bonds within the Au_{19} nanoparticle. The comparison with molecular gold species indicates that Au_{19} displays higher amounts of metallic character than the molecular species. However, rather than this metallic character being internal within the cluster, it was found to be diffuse and present at the molecular surface. The differences upon the surface were examined in terms of the Average Local Ionisation Energy, which indicated significant distinctions in ionisability between the vertex and edge atoms of the cluster.

Analysis of the descriptors of bonding environment at the critical points found by the atoms in molecules analysis indicated that there are three distinct types of bonding within the Au_{19} particle. These can be trivially divided between Edge, Facet, and Internal bonds and it is suggested that these variations in bonding are equivalent to the changes in catalytic activity and differing reactive character found over the surface of the particle.

The non-covalent interactions showed that the bonding of the surface atoms of the cluster was best described as a combination of metallic and covalent bonding, where covalently bonded regions were surrounded by areas of attractive non-covalent interaction that was significantly metallic in character. This metallic character was demonstrated by the metallicity and the localisation measures, both of which showed agreement with the NCI analysis. All of the measures indicate that the surface of Au_{19} presents a significantly distinct electronic structure to the molecular species of size equivalent to the facets.

Comparison of the metallicity of the molecular gold species Au_6 and the facet of Au_{19} at the bond critical points was found to indicate that the bonding within Au_6 was significantly more metallic in character than the mixed covalent metallic bonds that were observed in Au_{19}. However, comparison of the NCI for the two species, which indicated that the covalent bonds between the surface atoms of Au_{19} were surrounded by regions of attractive non-covalent interactions, suggested that there is stronger non-covalent interactions within the nanoparticle.

Building upon this characterisation of the differing bonding environments, a method for analysing and predicting stress using a bond aligned elastic tensor was also elu-

cidated. This distinguishes between the distinct bonding environments and characterises their elastic properties using an approximated tensor calculated across a set of candidate structures. This also describes a machine-learning derived methodology for approximating complex tensor properties through utilisation of the neural network for the purposes of error-gradient descent. Bond-aligned, local elastic constants were found to accurately characterise the relationship between stress and strain and these were determined using a cost-effective computational resource investment.

This approach to property determination is not limited to elasticity, which was selected for the purposes of this study due to the inherent difficulty in applying the concept to nanoparticle systems and the utility to biological property prediction, but can be applied in more general terms to allow for the accurate prediction of tensor properties given a sufficient set of training data.

Chapter 5

Irregular Particle Symmetry Analysis

5.1 Introduction

Symmetry is one of the fundamental paradigms through which the universe, and that which is contained within it, may be examined, understood, and simplified. The majority of properties of physical systems and molecules are derived from the character and interaction of the constituent atoms that form the system and the symmetry of these interactions provides significant insight into the form and quality of resultant properties.[96] Symmetry is generally utilised as a method of binary classification into discrete categories through the representations afforded by group theory, however, as demonstrated by Zabrodsky, Peleg, and Avnir, this illuminates only one facet of the utility that symmetry can provide.[120] Continuous symmetry measures provide a paradigm through which symmetry can be examined that, in accordance with Leibniz's continuity principle, account for a continuum of infinitesimal changes that underlie a finite or discrete change.[120,121]

Continuous symmetry measures show particular utility for classification and approximation. The use in classification arises from being able to describe a system in terms of a quantifiable proximity to a higher symmetric classification than is determined by group theory. As will be demonstrated by this study, this allows for an examination of molecular dynamics trajectories or crystal structures that clearly show favourability or distinct symmetry states that would otherwise be classified as C_1 symmetry. For the applications to approximation, by measuring symmetry and using near-symmetries to give a fix approximation, initial guesses for electronic structure or tensor properties can be approximated based upon these measures, which can be used

to reduce computational cost or speed up theoretical procedures.

Earlier works in continuous symmetry have developed robust methodologies for characterising symmetry without a reliance upon dichotomous conception. The continuous symmetry measure (CSM) developed by Dryzun *et al*, as described by equations 5.1 and 5.2, calculates the symmetry as a maximisation of the measure comparing a geometry and permutations of a symmetry transformed geometry which is normalised relative to the order of the operation and the size of the structure.[122]

$$S(G) = 100 \left[\frac{max \sum_{i=1}^{N} \sum_{j=1}^{N} \bar{Q}_i{}^T \hat{g}_j(m) \bar{Q}_{\hat{P}_{ij}}}{hd^2} \right] \tag{5.1}$$

$$d = \sqrt{\sum_{i=1}^{N} |\bar{Q}_i|^2} \tag{5.2}$$

Where $\bar{Q}$ is the original geometry, i is the index of the atom, h is the order of the operation, $\hat{g}_j$ is the j^{th} symmetry transform, m is the unit vector for the axis of the transform, N is the number of atoms, and P_{ij} is a specific permutation of the atoms.

The work of Pinsky *et al* on symmetry operation measures describes an ingenious methodology for evaluating the extent to which a geometry is symmetric under a given symmetry operation. This measure is defined, as is shown in equation 5.3, using the minimal distance between a geometry and the transformed image of the geometry normalised relative to the size of the geometry to produce a percentage relative to ideal symmetry.[41]

$$Z(Q, \hat{R}) = min \frac{\sum_{k=i}^{N} |q_k - t_k|^2}{4 \sum_{k=i}^{N} |q_k - q_0|^2} \times 100 \tag{5.3}$$

$$T = \hat{R}\hat{P}Q \tag{5.4}$$

Where Q is the geometry composed of N points, q_k, q_0 is the centre, and t_k is a point from the set of points T which is closest to equivalence with q_k following a symmetry transform, $\hat{R}$, acting upon the points of Q. In order to construct T, a label interchange operator, $\hat{P}$, is utilised, as shown in equation 5.4, in order to determine the minimum possible collections of pairings of points for the operation under measurement.

This form of approach, where symmetry is normalised with respect to the structure under examination, introduces some limitations within the methodology. By normalising relative to the distance from the geometric centre, distortions towards the exterior of a geometry become reduced arbitrarily. The limitation imposed by this approach can be understood by considering a trimer of π—π stacked benzene rings arranged such that the rings are evenly distributed along a shared axis of 6-fold rotation. For a given distortion of a ring, the change in measured rotational symmetry would be different depending upon the distance of the ring from the geometric centre.

A similar argument against the normalisation factor used in the CSM measure of Dryzun *et al* can be constructed. An example that demonstrates the limitation introduced by this scaling factor can be exemplified by consideration of distortions in a dimer of π—π stacked benzene rings distributed along a shared axis of 6-fold rotation. An idealised ferrocene geometry with benzene rings of the same orientation as the dimer but with greater spacing along the axis of 6-fold rotation can also be constructed. Introducing equivalent distortions to the benzene rings of the dimer and the benzene rings of ferrocene would result in different measures of symmetry for the two geometries, despite the distortions being equivalent with respect to the symmetry element. The distortion in symmetry relative to an element should not be decreased due to scaling along the axis of the element but, due to imposition of the normalisation factor related to the size of the geometry, the measure would show a reduction in distortion for the ferrocene in comparison to the dimer of benzene molecules when measured against the 6-fold rotation.

The incorporation of a normalisation factor into these measures results in changes in symmetry not measured as equal despite being distortions of the same magnitude and character. Whilst normalisation factors do introduce an ability to compare between geometries of different sizes, by using a geometry-dependent factor the reliability and accuracy of the measure is significantly reduced. For this reason, the form of measure introduced within this work utilises a constant normalisation and measures symmetry as a deviation relative to perfect symmetric equivalence in terms of unit length.

These numerical methodologies often also prove difficult to apply in an automated

form, with this being a particular issue for large or highly irregular systems, due to the complexity of evaluation.[122] The Symmetrizer described by Largent, Polik, and Schmidt applies most effectively to nearly symmetric objects and the methodologies requiring construction of polyhedra also prove difficult to apply to larger systems.[123–125] The available methods for continuous symmetry analysis, although still useful in their own domains of application, show similar limitations when the analysis of large irregular species is required, as the computational workload scales approximately with $O(N!)$.[122] Although the work of Dryzun *et al* does provide an examination of symmetry that scales with $O(N^2)$, this is an approximation and, as described above, the measure that it approximates is also based upon a methodology that is weakened by the introduction of size-dependent scaling.

This chapter provides the theoretical basis and methodology for a novel and robust technique that allows for the analysis of symmetry as a continuous measure. This methodology avoids the limitations imposed by geometry dependent normalisation factors used in earlier approaches and measures symmetry using a geometrically derived algorithm, which scales with $O(N^3)$. This also avoids the necessity for nearest neighbour searches with symmetry images or construction of shapes of known symmetry, both of which greatly increased the computational cost of earlier measures. Four novel methods of symmetry analysis, the proof of concept Irregular Particle Symmetry Analysis software, and the theoretical framework for examining continuous symmetry and group theory under a consistent mathematical framework will be discussed.

This work demonstrates several novel approaches to applying symmetry as a tool for exploring chemical systems and discusses a unique insight into how the geometric symmetry of atomic structures may be examined and quantified. This is both a practical methodology for application to chemical investigations and a low cost addition to other existing examinations of materials and molecular properties. It provides not only methodologies for analysis but also a tool for using symmetry as a categorisation and investigative protocol with a diverse range of applications.

5.2 Symmetry Analysis Methodology

5.2.1 Implementation

The Irregular Particle Symmetry Analysis (IPSA) code implements four measures of symmetry using a novel method of analysis in order to enable the examination of geometries that would previously have been difficult to do so with other symmetry analysis techniques. IPSA is a parallel code that is developed in the Rust programming language as both a stand-alone command-line interface analysis tool and Python 3.0 accessible library, which enables the automation of the symmetry analysis techniques and the incorporation into existing unsupervised methodologies and toolchains.[126,127] The IPSA software source code is available via the Roldan group website:

http://www.roldan-group.com/

The process applied by the software can be broadly divided into parsing, preparation, analysis, and interpretation. With parsing, preparation, and interpretation being trivial in terms of time-cost and analysis being a bottleneck that scales approximately with $O(N^3)$ where N is the number of atoms. Multiple elements being present decreases the number of pairwise comparisons required for each atom and so a molecule of 30 atoms but three chemical elements would require less resources for analysis than a structure with 20 atoms of the same element. Furthermore, higher symmetry structures tend to have fewer potential axes and, whilst smaller geometries require analysis for fewer orders of rotation, an artificial cap of rotational order, $O_{max} = 15$, is introduced by default for geometries with more than fifteen atoms.[96] Speed is also increased by pre-calculation of values for pairs of atoms relative to the axis being tested and order-independent components are reused where possible to avoid repetitive calculations. This ensures that calculations are relatively efficient despite their potential for complexity. Small structures have an analysis period of milliseconds and larger multi-element geometries of around 20 atoms of 23 elements have been found to take seconds on a standard desktop computer. This analysis has also been applied to low symmetry mono-element nanoparticles of up to 50 atoms and, although there is significant variation in computational time depending upon the symmetry and arrangement of atoms, these take a period of tens of minutes, further details and runtimes for various sample systems are provided within the supplementary information. This efficiency makes IPSA a practical tool for analysis of simulated structures and a relatively low time-cost addition to existing computational calculations.

5.2.2 IPSA Symmetry Analysis Process

5.2.2.1 Preparation

Prior to the automated analysis, an initial preparation of the structure is undertaken by determining the geometric centre of the collection of atoms and then translating the molecule to the origin of the Cartesian space. Four algorithms are utilised to generate the potential symmetry axes, with the positions of the atoms used as the initial set of potential axis points. This set is expanded by the inclusion of the potential axes passing through the centres of edges, regular even-sided faces, and the mid-points, determined by triangulation of regular odd-sided faces. The final algorithm searches for potential axes that are normal to the plane defined by a pair of points from the set of potential axes and the origin. The extensive set is then normalised such that the vector lengths of the potential axes are unity and any axes that are within a threshold, 1×10^{-3} Å by default, of the other potential axes are merged.

5.2.2.2 Analysis

The calculation of symmetry is done through application of the analytic, pairwise, axis and operation-dependent continuous symmetry measure, CSM_l, shown in equation 5.5. This function determines the symmetrical equivalence of a pair of atoms about an axis for a given symmetry operation and has the same fundamental form for all symmetry operations excluding those relevant to tiling and space-group symmetries.

$$f(x_1, x_2, y_1, y_2, z_1, z_2, \theta, O) = \frac{1}{1 + \sqrt{C_{xy}(\theta, O, x_1, x_2, y_1, y_2) + C_z(z_1, z_2, \theta, O)}} \tag{5.5}$$

Where f is a pairwise measure of symmetry, x_n, y_n, and z_n are the coordinates for the pair of atoms $a1$ and $a2$, C_{xy} and C_z, defined below, are measures of displacement from symmetric equivalence for the given operation, O is the rotational order of the operation, and θ is the angle between the atoms projected onto the xy-plane.

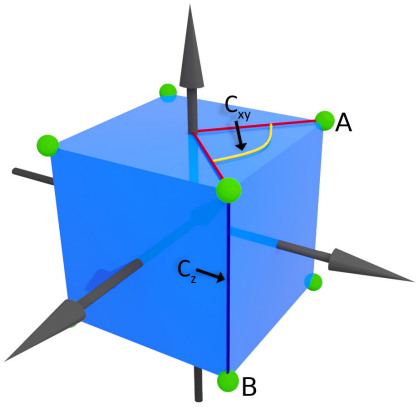

Figure 5.1: Aspects measured by C_{xy} and C_Z for the cubically arranged atoms A and B.

Following the determination of a set of potential axes, the atoms of the candidate structures

are divided by element to give E sets of atoms. All atoms are measured once per axis to determine their axial character using the f-function detailed in equation 5.5, where C_{xy} has the form shown in equation 5.6 defining the distance from the z-axis. For roto-reflectional operations, the measure compares the position of the atom to both the z-axis and also to the reflection of the atom, which utilises the C_z given in equation 5.8. Indeed, the quality of axiality, f_a, for an axial atom can be determined by measuring the distance of the atoms from the z-axis and, in the roto-reflectional case, axiality also includes the z-displacement and axiality of the atom that lies closest to a symmetry equivalent position. Equations 5.6—5.9 show special cases of the C_{xy} and C_z functions where the calculation can be simplified and reduced in complexity.

$$C_{xy}(x_1, y_1) = x_1^2 + y_1^2 \tag{5.6}$$

$$C_{xy}(x_1, y_1, x_2, y_2) = (x_1^2 + y_1^2) - (x_2^2 + y_2^2) \tag{5.7}$$

$$C_z(z_1, z_2) = (z_1 - z_2)^2 \tag{5.8}$$

$$C_z(z_1) = z_1^2 \tag{5.9}$$

For all atoms, the measure as a function of distance from the origin is also determined, f_o, once for each structure using the C_z given in equation 5.9 and the C_{xy} of equation 5.6.

The components of the pairwise symmetry, C_{xy} and C_z, are respectively given by equations 5.10 and equations 5.11, 5.12, and 5.13. The derivation of these equations can be found in appendix A.1. As is shown in figure 5.1, C_{xy} quantifies the deviation of a point B following a symmetry operation, with respect to the position of the reference point A, projected onto the xy-plane. The deviation from the xy-plane is then quantified using C_z, this varies depending upon the type of operation and whether the point should be reflected through the xy-plane at the origin, i.e. roto-reflection or inversion. This allows for all operations to be quantified using the same form of equation and for direct comparison in deviation from symmetrical equivalence. Atoms that were determined to be perfectly axial or placed directly at the origin are excluded from these calculations, as θ cannot be calculated for points that lie directly upon the axis, and assigned pairwise f-values of zero, see equation 5.10. These f-values can then be used to determine the combined symmetric relationships of individual atoms to all other atoms with respect to the specific symmetry operation, order, and axis.

$$C_{xy}(\theta, O, x_1, x_2, y_1, y_2) = \begin{pmatrix} -2\sqrt{a^2+b^2} \times \sqrt{2(a^2+b^2) - 2d\cos(c)} \\ \cos\left(\arccos\left(\frac{y_1 a + x_1 b}{\sqrt{d}\sqrt{a^2+b^2}}\right) - \frac{\pi - c}{2}\right) \\ -2d\cos(c) + a^2 + 2d + b^2 \end{pmatrix} \quad (5.10)$$

Where: $a = (y_1 - y_2)^2$, $b = (x_1 - x_2)^2$, $c = \frac{2\pi}{O}\lfloor\frac{O\theta}{2\pi} + 0.5\rfloor$, $d = x_1^2 + y_1^2$

$$C_z = (z_1 + \epsilon(O, \theta) \times z_2)^2 \quad (5.11)$$

Where $\epsilon(O, \theta)$ is a sign determining coefficient that varies based upon the operation, as shown in equation 5.12.

$$\epsilon(O, \theta) = \begin{cases} -1 & \text{Proper rotation} \\ 1 & \text{Reflection} \\ \begin{cases} 1 & \epsilon_z(O, \theta) \geq 0 \\ -1 & \epsilon_z(O, \theta) \leq 0 \end{cases} & \text{Inversion, Improper rotation} \end{cases} \quad (5.12)$$

Where: $\epsilon_z(O, \theta) = \frac{2}{\pi}\arccos\left(cos\left(\frac{1}{2}O\arccos\left(cos\left(\frac{2\pi}{O}\right)\right)\lfloor\frac{O\theta}{2\pi} + 0.5\rfloor\right)\right) - 1$ (5.13)

Reflections can be understood as a subset of the improper rotations, a rotation by 2π followed by a reflection in the plane orthogonal to the rotational axis. Similarly, it can also be seen that inversion symmetry is analogous to a second order improper rotation, $O = 2$, where a rotation by π followed by a reflection in the plane orthogonal to the axis causes an inversion of the structure about the geometric centre.

The combination of the pairwise f-values is achieved through the application of equations 5.14 and 5.16. Equation 5.14 produces a combined value for a specific axis and order that incorporates the pairwise components, as expressed above. The pairwise quantities, f, are sorted such that the zeroth term is the maximum and a mean is then taken over the O highest values, which determines the symmetric equivalence for a given order. This is corrected by multiplying by one minus the difference between the maximum and minimum f in order to give F. This range correction is done to ensure individual terms are not averaged to insignificance for the larger sets of atoms

with high symmetry and individual atoms that diverge significantly from the high symmetry. If the number of values of f is less than O then these missing values are treated as zeros, which indicates maximal symmetric inequivalence due to non-existence.

$$F(f_0, f_1, ..., f_O) = \frac{\sum_{n=0}^{O} f_n}{O}(1 - f_O + f_0) \tag{5.14}$$

Atoms are then assigned an F_{fao} value, which is the greatest of the F, f_a, or f_o confidences, as shown in equation 5.15.

$$F_{fao} = \begin{cases} F & F > f_a \text{ and } F > f_a \\ f_a & f_a > f_o \text{ and } f_a > F \\ f_o & f_o >= f_a \text{ and } f_o >= F \end{cases} \tag{5.15}$$

The F_{fao} values are also used to examine the single atom symmetry, SAS, which combines the F_{fao} with respect to each accepted axis to produce a per-atom symmetry measure, discussed further below. The means of these values for a specific order are then combined by taking the mean across all groups of chemical elements to produce F_{axial} values, as shown in equation 5.16. These F_{axial} values are used to calculate axial confidences for each rotational order and operation, which are used to determine whether a potential axis is accepted as an actual axis, the order of operation, and whether an axis is included in the calculation of continuous symmetry, soft and hard point group assignment, and per-atom symmetry, as discussed below.

$$F_{axial}(F_{0,0}, ..., F_{E,N_E}) = \frac{\sum_{e=0}^{E} \frac{\sum_{m=0}^{N_e} F_{fao}}{N_e}}{O} \tag{5.16}$$

Where E is the number of symmetry elements and N_e is the number of atoms of each element.

Axis assignment is based upon the F_{axial} values of operations. The subgroups of a symmetry element, which are the co-existent lower order symmetry elements of a specific operation, are determined separately for the proper (C_{proper}) and improper

(C_{impr}) operations and are given, respectively, by equations 5.17 and 5.18.

$$C_{proper} = \begin{cases} 1 & G \bmod g = 0 \\ 0 & G \bmod g \neq 0 \end{cases} \tag{5.17}$$

$$C_{improper} = \begin{cases} 1 & \frac{G}{g} \bmod 2 = 1 \\ 0 & \frac{G}{g} \bmod 2 \neq 1 \end{cases} \tag{5.18}$$

Where G is the magnitude of the overgroup order under examination and g is the magnitude of the order of the group to be examined as a potential subgroup of G.

F_{axial} values that correspond to the potential subgroups, g, of the prospective overgroup, G, are multiplied by their respective C_{prop} and C_{impr} coefficients, which are then summed to produce group confidence values. These confidences determine the likelihood of a specific group being the primary cyclic or roto-reflectional group associated with that axis. The existence of a subgroup of a specific overgroup bolsters the confidence in the overgroup whilst, conversely, the existence of an overgroup decreases the relative confidence in the subgroup. These subgroup corrected values are then normalised within the range of 0—1 and subsequently multiplied by the F_{axial} values leading to confidence values where the highest value of the proper rotations and improper operations indicates the primary operation of the axis for each set of operations. An artificial, perfect unit operation is also introduced into the improper rotations to give a baseline for comparison; this is done to ensure that, if no roto-reflectional symmetry element exists, the roto-reflectional element of the axis will be assigned to an artificial unit value and discarded as a roto-reflectional axis. For planes of reflection, as the symmetry does not potentially encompass subgroups, a comparative measure of confidence is not required.

5.2.3 Interpretation

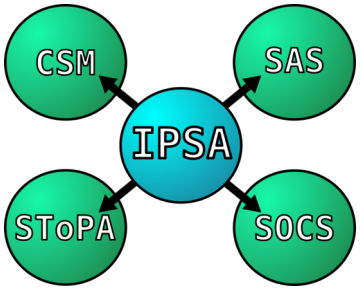

Figure 5.2: Ipsa symmetry interpretation measures.

5.2.3.1 Continuous Symmetry Measurement

CSM_l characterises symmetry as a single value, indicating the number and quality of the symmetry elements that exist for a specific structure. Unlike categorisations such as point groups, continuous symmetry measures do not attempt to divide symmetry by the type of operation, allowing for different forms of comparisons than discrete symmetry categorisation. Alongside continuity, the specific characteristics deemed to be of primary importance to forming a useful measure were:

I. Comparability of CSM_l values between structures of significantly different compositions.

II. Linear change in the CSM_l value corresponds with linear distortions with respect to a specific element.

III. Subgroup symmetries being accounted for in the CSM_l measures.

The continuous symmetry measurement is constructed from a sum of the F_{axial} quantities associated with the highest order symmetry element of the accepted axes, those which exist with a confidence that passes a lower arbitrary limit, l, multiplied by the magnitude of the order of the symmetry element, O. These values are then summed to produce the measure, which is referred to as CSM_l. The range of this is from CSM_0, where axes of any quality are accepted and only those where the maximum $O = 1$ are excluded, to CSM_{100}, which is limited to exact axes of symmetry that have perfect values for axes with $O > 1$ and $O < 0$, which are the roto-reflectional operations. The symmetry elements that are included in CSM_l are those for where

$F_{axial} \geq l$; for example, $CSM_{33.3}$ represents an accepted distortion, s, from symmetrical equivalence of 2.00 Å.

Treating deviations away from perfect symmetry as being equivalent due to their numerical size in units of length ensures that a distortion of s Å is equivalent between geometries of different size and also that the CSM_l is comparable and equivalent between structures. However, the comparability between significantly different geometries can limit comparisons between similar geometries of different scales. An example of such systems are SF_6 and Au_{19}, which both have octahedral symmetries despite the different constituent elements and, therefore, differing bond lengths. For these cases it is possible to examine distortions as a proportion of the geometry, rather than in absolute terms, by normalising the geometries following their centring upon the origin. For this purpose, the length of the shortest, non-zero vector between an atom and the origin, or another vector that is considered to provide a better equivalence between structures, is scaled to unit length. The analysis is then performed in arbitrary units that are relative to this scaled length.

Linearity of the continuous measurement is ensured by using a sum of the F_{axial} values. A symmetry of half the quality in absolute terms corresponds to a halved value of the continuous measure. Incorporating subgroups into the measure ensures that primary axes are not treated as equivalent when more symmetries are also present. For practical purposes it is suggested that CSM_{99} and $CSM_{33.3}$ provide particular insight into the structural symmetry. However, using other l values may prove to be of greater utility for specific systems as the l value can be chosen to increase sensitivity in the range of interest.

5.2.3.2 Soft-tolerance point group assignment

Discrete point group assignment is commonly utilised to categorise the collected symmetry operations of a molecule into a point group. These point groups are most commonly specified using the Schönflies notation, with the categories of point groups specified under the Schönflies schema broadly divided into cyclic, roto-reflectional or mirror, and cubic groups.[128] The subdivisions of these categories are then given by the orders of operation of the primary axis and the other elements that define the group. For instance, the D_x grouping is that of the mirror or roto-reflectional groups; these are defined as containing at least one cyclic element of $O > 1$ as well as OC_2 axes orthogonal to the primary axis, C_O. The cubic groups, Octahedral (O), Icosahedral (I), and Tetrahedral (T), are distinguished from the cyclic and roto-reflection groups by their containing two or more C_3 axes. These are then further subdivided based upon the rotational, reflectional, and inversion symmetry elements.

To achieve discrete point group categorisation, symmetry elements are evaluated on a binary basis. An element is understood as being either present or not and, based upon the extant symmetry elements, a structure is classified within a specific point group. This discrete categorisation is robustly supported by the mathematics of group theory. However, as explained in the theoretical section above, it loses some utility in describing physical systems, particularly where thermal noise creates geometries that are formally classified as C_1 or where slight deviations from perfect symmetry occur due to internal strains on bond lengths and angles. For this reason, the concept of soft assignment has utility in the description of physical systems where thermal noise and inherent uncertainty ensure that perfect symmetry is an idealised model in all but the most exceptional of physical conditions.

Soft point group assignment quantifies the deviation from all point groups and allows for the closest point groups to be determined rather than solely ascribing a single perfect point group. This method of categorisation is achieved by computing the quality of conformity to the elements which determine categorisation and requires that certain secondary values are calculated, see supplementary information for the details of these calculations and the point group binary tree used for assignment. These quantitative assessments are then combined to allow for the extent to which a structure conforms to the requirements of specific point groups to be examined. This is undertaken as a binary tree where the weighting of each branch is given by either P

or $1-P$, where P is the confidence in the existence of a specific symmetry element or combination of symmetry elements, calculated during the evaluation of CSM_l. As the conditionals are inclusive, the total for each group can be determined by multiplication of the values ascribed to the branches that must coincidentally occur for that specific point group; examples of the C_s and C_i are given by equations 5.19 and 5.20 respectively. The range of the P values is limited by normalisation those within specified thresholds to the range 0—1 and setting values outside of these limits to either zero or one. This limitation of the value of P allows for the process of soft assignment to be utilised in discrete categorisation, as well as increasing the sensitivity of the measure within the specified limits. Lower and upper bounds of 0.9999 and 1.0000 respectively mimic a discrete assignment, whilst tolerance values of 0.3333 and 0.9700 allow for the symmetry scores in this range to be accepted and excludes distortions for individual symmetry elements that result in symmetries of quality lower than the smaller limit. This method of analysis allows for the structures to be discretely categorised and for the similarity to multiple other point groups to be examined simultaneously, with the specified values depending upon the thresholds with which they are evaluated. The results of these calculations are given as $StoPA_l^m$ values, with m and l specifying the upper and lower bounds of the measurement, and are quoted as point groups followed by percentage confidences, for example: C_s – 44.92%, C_1 – 55.08%.

$$P(C_s) = (1 - P(Linear))(1 - P(C_s))(1 - P(C_n))P(\sigma) \tag{5.19}$$

$$P(C_i) = (1 - P(Linear))(1 - P(C_s))(1 - P(C_n))(1 - P(\sigma))P(Invert) \tag{5.20}$$

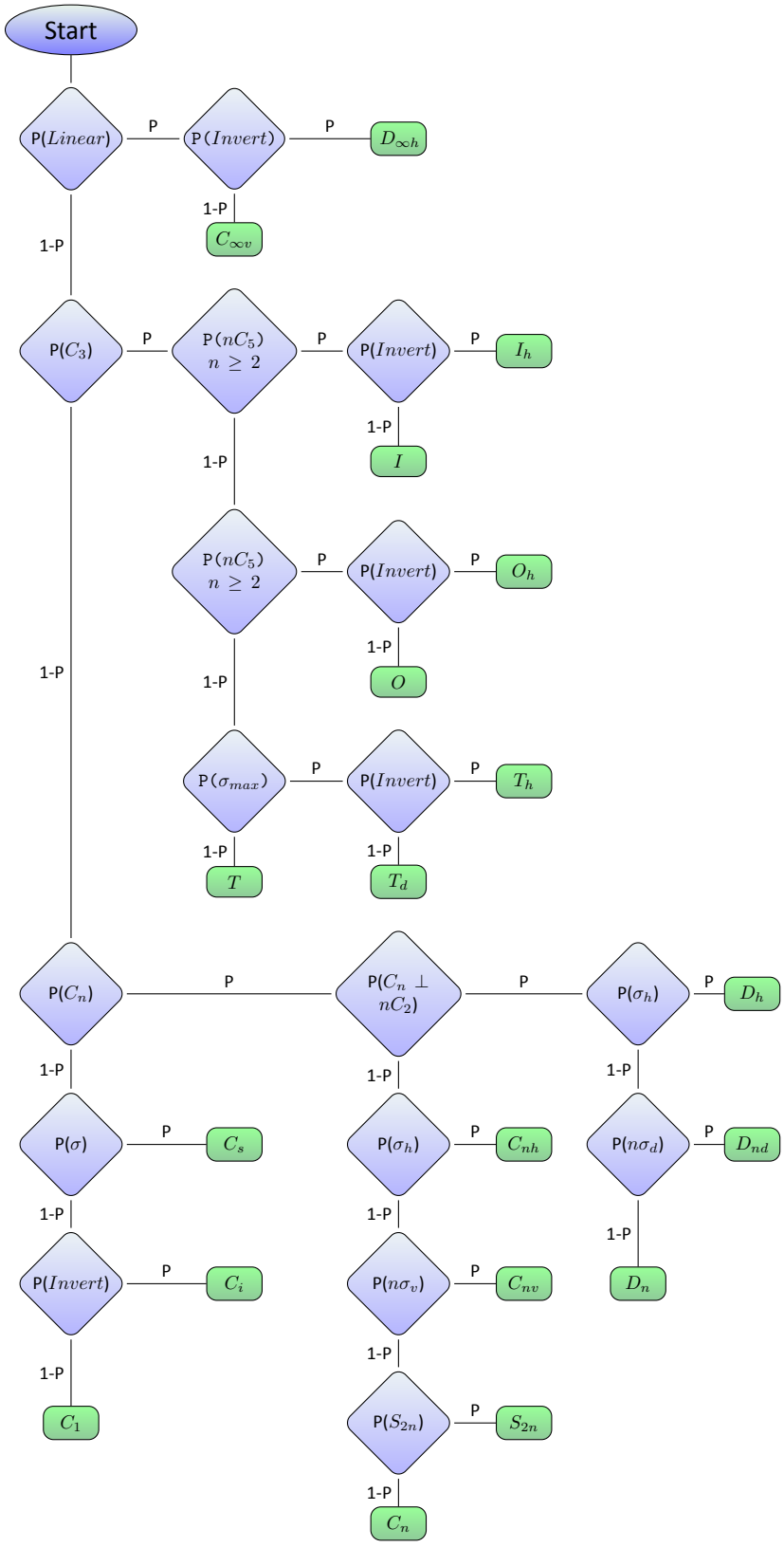

Figure 5.3: Point group assignment as a binary tree of conditional confidences.

5.2.3.3 Single Atom Symmetry

Single Atom Symmetry, SAS, is determined by combining the F_{foa} values for the primary operations of all accepted axes that have a primary screening value $\geq l$, where l is between zero and one. This SAS_l value gives a measure of the symmetric relationships that an atom has with all other atoms to which it shares near or perfect symmetric equivalence. Higher values of SAS_l indicate a greater number of higher quality symmetry elements present for a specific atom. For example, it can be observed that the symmetry of the hydrogen atoms within the distorted geometries of the vibrational modes of chloromethane are distinct based upon the symmetries despite their being the same element. Atoms placed at the origin have a formally infinite score for this measure, although in practical terms this value is limited to the order of each axes for the other points, N_{max}.

5.2.3.4 Zeroth, First Order, and n^{th} Order CSM

The CSM_l and SAS measures can be combined to determine n^{th} order CSM, CSM_l^n. Here, the continuous symmetry and single atom symmetries are iteratively calculated n times, with the zeroth order being the CSM_l defined above. The subsequent symmetries are computed with the lowest symmetry atom, as determined by the SAS_l value, excluded from the calculation. The result gives values of CSM_l^n that indicate the extent to which the lowest symmetry atoms cause a lower CSM value. If $CSM_l^0 > CSM_l^1$ then it can be determined that the structure is distorted from an optimal symmetry whereas, if $CSM_l^0 < CSM_l^1$ then the atom indicated by the lowest CSM_l value for that symmetry is strongly symmetry breaking. This has particular utility in determining the effects of individual atom symmetry upon structural symmetry, whether symmetry of whole structures is favoured over the symmetric equivalence of individual atoms.

5.2.3.5 Symmetry as a vector space

Sylow theory, which is rooted in the Lagrange theorem, specifies that the order, O, of any overgroup, G, can be expressed as the product of the prime factors p_n raised to an appropriate exponent, α_n where $\alpha_n \in \mathbb{Z}_{\geq 0}$ and $\mathbb{Z}$ is the set of all integers.

$$O = 1^0 \times 2^{\alpha_1} \times ... \times p^{\alpha_n} = \prod_{n=1}^{\infty} p_n^{\alpha_n} \tag{5.21}$$

This ensures that the coexistent subgroups for a given overgroup must necessarily be a combination of the prime factors raised to a power less than or equal to the power of the prime factor in the overgroup. For example, the group with a rotational order of 12 can be expressed as:

$$12 = 1^0 \times 2^2 \times 3^1 = 2^2 3 \tag{5.22}$$

It follows from this that the prime factors of the order, O, can be expressed as shown in equation 5.23.

$$log(O) = \sum_{n=1}^{\infty} \alpha_n log(p_n) \tag{5.23}$$

For $\alpha_n \in \mathbb{Z}_{\geq 0}$ it can be observed that the $log(p)$ terms can be used to form a vector space where the exponent is treated as the coefficient of a basis vector $\vec{x_n} = log(p_n)$.

$$\overrightarrow{log(O)} = \begin{matrix} \vec{x_n} \\ log(2) \\ log(3) \\ log(5) \\ \vdots \\ log(p_n) \end{matrix} \begin{matrix} \alpha_n \\ \begin{pmatrix} \alpha_1 \\ \alpha_2 \\ \alpha_3 \\ \vdots \\ \alpha_n \end{pmatrix} \end{matrix} \tag{5.24}$$

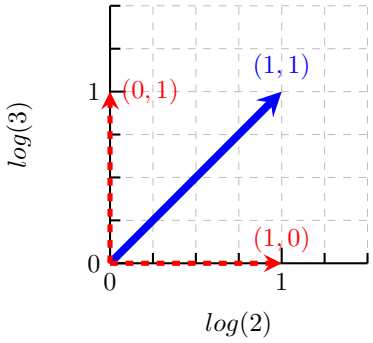

(a)

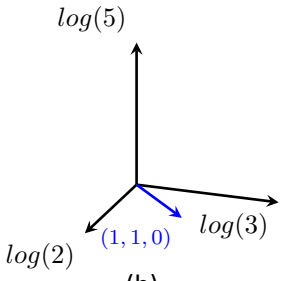

(b)

Figure 5.4: $O = 6$ plotted in the logarithmic vector space of prime factors. Shown as the vector $(1, 1)$ in a 2-dimensional slice along $log(2)$ and $log(3)$ and as the blue vector $(1, 1, 0)$ in the 3-dimensional section of the space showing the $log(2)$, $log(3)$, and $log(5)$ axes.

This then allows for group theory to be represented by the coefficients of the basis vectors $\vec{x_n}$. This representation is formally countably infinite in dimension over all primes greater than 1, $\mathbb{P} = 2, 3, 5, 7, 11, 13, ..., p_\infty$. However, being generally of the order $O \leq 15$, groups relevant to chemistry can generally be sufficiently characterised using a finite subspace of the infinite vector space with dimension 6; this form is shown in equation 5.25.

$$\overrightarrow{log(O)} = \begin{matrix} \vec{x_n} \\ log(2) \\ log(3) \\ log(5) \\ log(7) \\ log(11) \\ log(13) \end{matrix} \begin{matrix} \alpha_n \\ \begin{pmatrix} \alpha_1 \\ \alpha_2 \\ \alpha_3 \\ \alpha_4 \\ \alpha_5 \\ \alpha_6 \end{pmatrix} \end{matrix} \tag{5.25}$$

The symmetry vector space can be further expanded to include roto-reflectional symmetries by introducing a basis vector corresponding to $log(-1)$, giving a vector subspace of dimension 7. This then gives the set $\mathbb{P}_{-1} = -1, 2, 3, ..., p_\infty$ where $\mathbb{P} \in \mathbb{P}_{-1}$. The 7-vector representation of this space is shown in equation 5.26.

$$\overrightarrow{log(O)} = \begin{matrix} \vec{x_n} \\ log(-1) \\ log(2) \\ log(3) \\ log(5) \\ log(7) \\ log(11) \\ log(13) \end{matrix} \begin{matrix} \alpha_n \\ \begin{pmatrix} \alpha_0 \\ \alpha_1 \\ \alpha_2 \\ \alpha_3 \\ \alpha_4 \\ \alpha_5 \\ \alpha_6 \end{pmatrix} \end{matrix} \tag{5.26}$$

This formulation of the vector space then allows for reflections, $O = -1$; inversions, $O = -2$; and improper rotations, $O \leq -4$, to be represented in the vector space. Thus, all operations about an axis can be described by two vectors, one which encapsulates the proper operations and another which describes the improper elements. Vectors that correspond directly to real-space rotational elements have integer coefficients and $\alpha_0 = 0$.

$$\overrightarrow{log(6)} = \begin{matrix} \vec{x_n} \\ log(-1) \\ log(2) \\ log(3) \\ log(5) \\ log(7) \\ log(11) \\ log(13) \end{matrix} \begin{matrix} \alpha_n \\ \begin{pmatrix} 0 \\ 1 \\ 1 \\ 0 \\ 0 \\ 0 \\ 0 \end{pmatrix} \end{matrix} \tag{5.27}$$

Vectors that describe improper operations are given by vectors with integer coefficients and $\alpha_0 = 1, \alpha_1 \geq 1$.

$$\overrightarrow{log(-6)} = \begin{pmatrix} 1 \\ 1 \\ 1 \\ 0 \\ 0 \\ 0 \\ 0 \end{pmatrix} \tag{5.28}$$

Reflections are given by a vector with only $\alpha_0 \neq 0$ and inversions are given by the vector $\alpha_0 = 1, \alpha_1 = 1$

$$\overrightarrow{log(-1)} = \begin{pmatrix} 1 \\ 0 \\ 0 \\ 0 \\ 0 \\ 0 \\ 0 \end{pmatrix} \qquad \overrightarrow{log(-2)} = \begin{pmatrix} 1 \\ 1 \\ 0 \\ 0 \\ 0 \\ 0 \\ 0 \end{pmatrix} \tag{5.29}$$

Operations may also be combined multiplicatively through addition in the logarithmic space. The combination of $C_2 \times C_2 = C_4$ is given by the vector equation 5.30.

$$\begin{pmatrix}0\\1\\0\\0\\0\\0\\0\end{pmatrix} + \begin{pmatrix}0\\1\\0\\0\\0\\0\\0\end{pmatrix} = \begin{pmatrix}0\\2\\0\\0\\0\\0\\0\end{pmatrix} \tag{5.30}$$

Similarly the combination of $S_2 \times C_3 = S_6$ is given by the vector equation 5.31.

$$\begin{pmatrix}1\\1\\0\\0\\0\\0\\0\end{pmatrix} + \begin{pmatrix}0\\0\\1\\0\\0\\0\\0\end{pmatrix} = \begin{pmatrix}1\\1\\1\\0\\0\\0\\0\end{pmatrix} \tag{5.31}$$

It can be observed that this representation is sufficient to represent all known symmetries as a collection of vectors in the log-space.

For example, a square can be represented by the vectors:

$$\begin{pmatrix}1\\2\\0\\0\\0\\0\\0\end{pmatrix}, \begin{pmatrix}0\\2\\0\\0\\0\\0\\0\end{pmatrix}, 4\begin{pmatrix}0\\1\\0\\0\\0\\0\\0\end{pmatrix}, \infty\begin{pmatrix}1\\1\\0\\0\\0\\0\\0\end{pmatrix} 5\begin{pmatrix}1\\0\\0\\0\\0\\0\\0\end{pmatrix} \tag{5.32}$$

This gives a total of 5 distinguishable axes, an inversion centre, and 5 planes of reflection. The vectors that give the square symmetry can be plotted as shown in figures 5.5a and 5.5b. A cube can also be represented in this space by the vectors shown in equation 5.33, as shown in figure 5.5c.

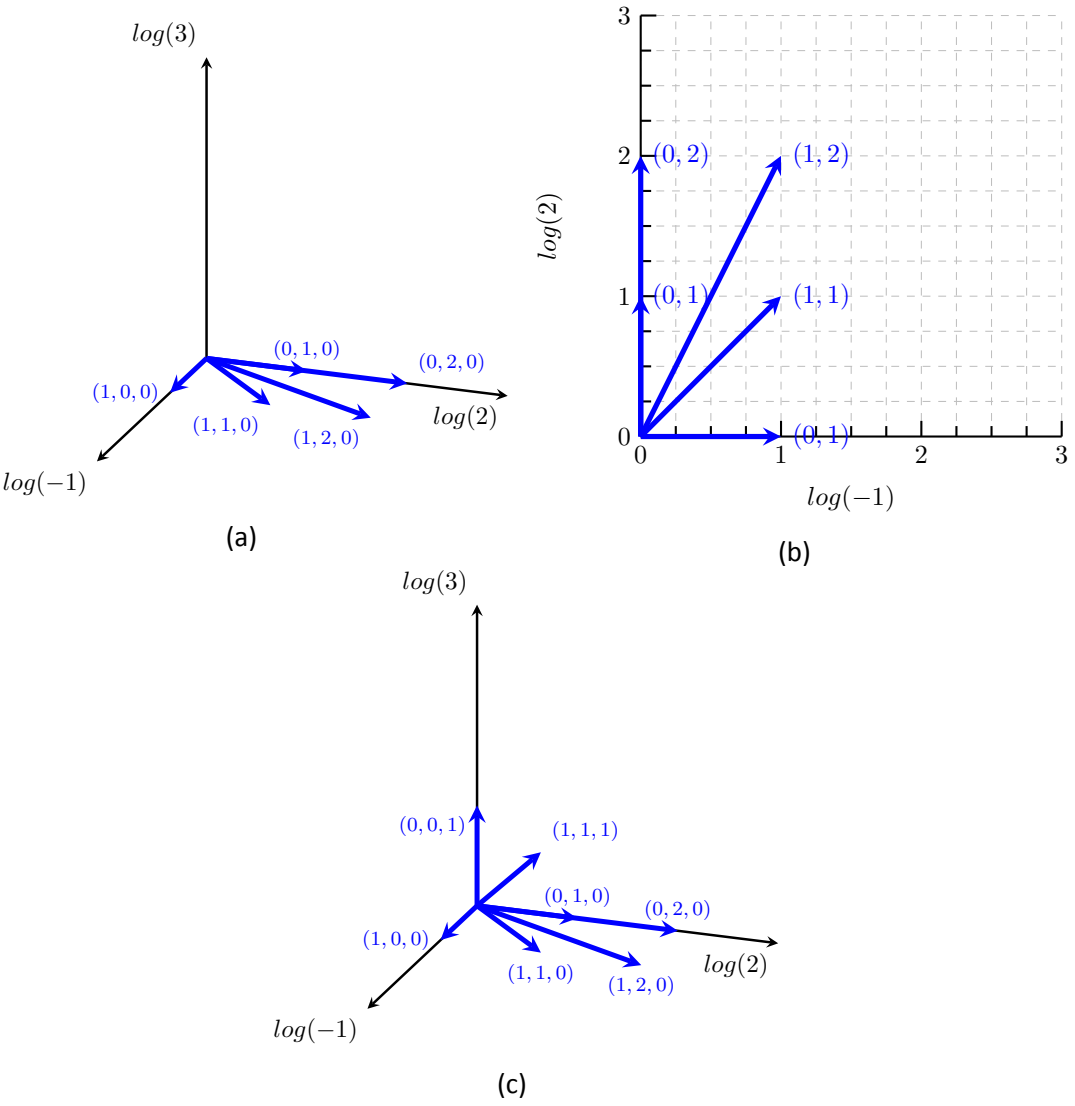

Figure 5.5: Symmetry space representation of a square, (a) and (b), and the symmetry space representation of a cube, (c).

$$3\begin{pmatrix}1\\2\\0\\0\\0\\0\\0\\0\end{pmatrix}, 3\begin{pmatrix}0\\2\\0\\0\\0\\0\\0\\0\end{pmatrix}, 6\begin{pmatrix}0\\1\\0\\0\\0\\0\\0\\0\end{pmatrix}, \infty\begin{pmatrix}1\\1\\0\\0\\0\\0\\0\\0\end{pmatrix} 9\begin{pmatrix}1\\0\\0\\0\\0\\0\\0\\0\end{pmatrix} 4\begin{pmatrix}0\\0\\1\\0\\0\\0\\0\\0\end{pmatrix} 4\begin{pmatrix}1\\1\\1\\0\\0\\0\\0\\0\end{pmatrix} \tag{5.33}$$

This representation also suggests a unifying description of symmetry, where con-

tinuous symmetry and group theory can both be described by the α coefficients of the vector space. The continuity of the space can be observed by allowing the coefficients of $\vec{x_n}$ to take on any real value, $\alpha_n \in \mathbb{R}$. The basis for this is demonstrated for the degradation of a C_4 to a C_2 using the symmetry-degradation operator $\hat{D}(g)$. Through application of the $\hat{D}(C_2)$ operator, as $C_4 \to C_2,\ \alpha_1 \to 1$.

$$\hat{D}(C_2)C_4 = C_2 \tag{5.34}$$

$$\hat{D}(C_2)\begin{pmatrix}0\\2\\0\\0\\0\\0\\0\end{pmatrix} \to \begin{pmatrix}0\\1\\0\\0\\0\\0\\0\end{pmatrix} \tag{5.35}$$

As established by equation 5.30, $\overrightarrow{log(4)}$ can be considered as a $\overrightarrow{log(2)} + \overrightarrow{log(2)}$, this can then be substituted into equation 5.35 to give equation 5.36.

$$\hat{D}(C_2)\left(\begin{pmatrix}0\\1\\0\\0\\0\\0\\0\end{pmatrix} + \begin{pmatrix}0\\1\\0\\0\\0\\0\\0\end{pmatrix}\right) = \begin{pmatrix}0\\1\\0\\0\\0\\0\\0\end{pmatrix} + \begin{pmatrix}0\\0\\0\\0\\0\\0\\0\end{pmatrix} \tag{5.36}$$

However, there is a second form of possible degradation, that being shown by equation 5.37.

$$\hat{D}(C_2)\left(\begin{pmatrix}0\\1\\0\\0\\0\\0\\0\end{pmatrix}+\begin{pmatrix}0\\1\\0\\0\\0\\0\\0\end{pmatrix}\right)=\begin{pmatrix}0\\0\\0\\0\\0\\0\\0\end{pmatrix}+\begin{pmatrix}0\\1\\0\\0\\0\\0\\0\end{pmatrix} \tag{5.37}$$

The change occurring during degradation, $\hat{D}(C_2)C_4 = C_2$, can be simplified to the form shown in equation 5.38.

$$\begin{pmatrix}0\\1\\0\\0\\0\\0\\0\end{pmatrix}\rightarrow\begin{pmatrix}0\\0\\0\\0\\0\\0\\0\end{pmatrix} \tag{5.38}$$

This formulation shows that the degradation of an axis of order $O = p_n^{\alpha_n}$ to an axis of $O = p_n^{\alpha_n - 1}$ axis can be conceptualised as being equivalent to the change from $O = p_n^1$ to an axis of $O = p_n^0$. This gives a constant C_2 that remains unchanged.

Groups are defined above as being the product of primes raised to an exponent restricted to the positive integers, $\mathbb{Z}_{\geq 0}$. From this it should be understood that the separation of the vectors indicates that, in terms of group theory, the order of the axis immediately changes to the maximum integer less than the α coefficient value. However, in terms of considering the symmetry as a continuous property, this can also be understood to suggest that the extent of degradation is encapsulated by the difference in α coefficients between the vectors of the initial and final symmetries. This can also be expanded into m transitions from p_n^1 to p_n^0, where m is the number of elementary prime degradations forming the change in symmetry.

This formulation also allows for degradation of multiple symmetries to be examined, such as the degradation of $O = 6$ to form threefold or twofold geometries. Simultaneous degradations of multiple symmetries may also be examined; for example

a fourfold degrading to asymmetry, $C_4 \rightarrow C_1$, can be understood as being consistent with equation 5.39.

$$\begin{pmatrix}0\\1\\0\\0\\0\\0\\0\end{pmatrix} + \begin{pmatrix}0\\1\\0\\0\\0\\0\\0\end{pmatrix} \rightarrow \begin{pmatrix}0\\0\\0\\0\\0\\0\\0\end{pmatrix} + \begin{pmatrix}0\\0\\0\\0\\0\\0\\0\end{pmatrix} \tag{5.39}$$

A point along this change would then be represented by a pair of vectors with non-integer α coefficients that do not correspond directly to group theory representations other than C_1. It is noteworthy that this symmetry, where two summed two-fold symmetries simultaneously degrade such that they cannot be recombined to form a single vector where the terms correspond to perfect symmetry. Different geometric changes produce unique symmetry representations and this suggests that certain structures require multiple vectors to represent a set of points in relation to a specific rotational axis, and that the zero terms of the vectors are themselves approximations, as no geometry is infinitely distant from a possible symmetry, where the limit in possibility is given by the number of equivalent points.

5.2.3.6 Geometric Algebra

This vector description of symmetry allows for the application of geometric algebra to discussions of symmetry. A brief example of this application is shown in equations 5.40 and 5.41, where the geometric algebra concepts of projection and rejection are applied to the vector representations of symmetry to determine the maximum symmetry of an overgroup with respect to a basis vector, $\vec{x}_n$ of the space and also the rejected symmetry formed from an overgroup and a basis vector.

$$(\vec{x}_n \cdot \vec{O})\vec{x}_n = \vec{O}_{\parallel \vec{x}_n} \tag{5.40}$$

$$(\vec{x}_n \wedge \vec{O})\vec{x}_n = \vec{O}_{\perp \vec{x}_n} \tag{5.41}$$

As such the definition of a subgroup under this model can be understood as being defined by equation 5.42. Where a group, g, is a subgroup of an overgroup,$\vec{O}$, if the projection of the overgroup onto the subgroup results in the group multiplied by a coefficient, s, greater than or equal to one.

$$(\vec{g} \cdot \vec{O})\vec{g} = s\vec{g} \tag{5.42}$$

5.2.3.7 Summary

These descriptions of symmetry do not replace those of group theory but expand upon the concept to allow for the discussion and description of near symmetries, those that exist already as part of a specific group, but do not result in specific symmetry elements being present. This then gives the theoretical foundation for measuring continuous symmetry, which can be considered as a measure of the deviation from integer values of the collective α_n exponents of the prime factors, p_n as described by equation 5.21. This is compatible with the group theory definitions of symmetry, where $p_n \in \mathbb{P}_{-1}$ and $\alpha_n \in \mathbb{Z}_{\geq 0}$, and also shows the utility of continuous symmetry in describing near symmetries when $\alpha_n \in \mathbb{R}$.

As this representation of symmetry is abstract mathematics, it is difficult to find direct chemical applications. However, as this understanding of symmetry is not restricted by the dimensions of the physical space, there are potential applications in using this to examine high-dimensional symmetry. One direct application is presented in the form of symmetry-orientation cross-section (SOCS) plots, where a cross-section of the symmetry vector coefficients are plotted against the orientation of the element in physical space. This gives a completely novel method for visualising symmetry.

5.2.3.8 Symmetry-Orientation Cross-Sections

Building upon the continuous vector space representation of symmetry, the symmetry-orientation cross-sections, SOCS, can be utilised to examine the near-symmetries of structures. Interpretation of the symmetry space cross section provides significant insight into the morphology of structures and it is the suggestion of the author that this may provide an interesting space in which reactions and dynamic processes can be observed.

By calculation of the orientation in real space of an axis or normal of a symmetry element, the magnitude of the respective symmetry vector under examination can be combined with the real space θ and ϕ values to give a real space direction that can applied to the symmetry vector. This allows for the construction of a symmetry-orientation space. Spherical symmetry-orientation cross-sections (SOCS) can then be utilised to examine the symmetries and near-symmetries of the geometries under examination. As shown in figure 5.6, one method for examining these cross-sections is by their projection onto a 2-dimensional plane.

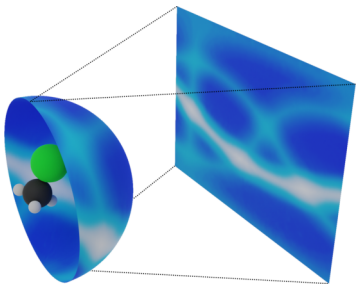

Figure 5.6: Mapping of the SOCS by projection from the unit sphere to a 2-dimensional plane for chloromethane.

The space can be examined for any combination of symmetry vectors, such that the inversion and improper rotation space θ-ϕ-$(log(-1) + log(2))$ (i-SOCS) or rotation space θ-ϕ-$(log(2) + log(3) + log(5) + log(7) + log(11) + log(13))$ (c-SOCS) may be examined, as well as any subset of those spaces. This allows for cross-sections that compare any and all permutations of symmetry, as well as comparison of the θ-ϕ-$(log(-1) + log(2) + log(3) + log(5) + log(7) + log(11) + log(13))$ space that characterises all symmetry for a given geometry, ω-SOCS. Similarly, as the components of the $log(-1)$ term characterise the reflections and improper rotations, a reflection SOCS (σ-SOCS), which excludes all other roto-reflectional vectors by subtraction, characterises the reflection space cross-section without inversion or improper rotation.

The SOCS maps were produced using the perceptually uniform colour map 'oslo' by Fabio Crameri in order to avoid artefacts due to non-uniform perceptual changes in

colour.[129] The 3-dimensional representations were produced using the Blender modelling software.[130]

5.3 Application of Symmetry Analysis

5.3.1 Symmetry of Isolated Nanoparticles

Changes in morphology that deviate from isolated ground-state geometries are often prevalent in real world systems, due to both environmental effects and thermal energetic contributions, symmetry analysis can also be applied to further understand the changes that occur within these systems. To model analysis of these forms of structural deformations a range of gradual changes from O_h to C_1 symmetry for Au_{19}, figure 5.7, are shown in table 5.1. Random displacements were applied to the atoms and the resultant structures were then analysed using the CSM_{95} measure. This method allows for the characterisation of the qualities of all symmetry elements which is advantageous over the application of discrete binary measures, as a discrete categorisation would interpret changes above the numerical tolerance to result in the immediate loss of symmetry elements. Furthermore, the $StoPA$ point group categorisation allows for the capture of point group symmetry within the bounds of acceptable fluctuations, such as in systems with thermal noise or slight numerical imprecision. The measures used for the categorisation of the distorted Au_{19} particles are relatively constrained and narrow, resulting in more noticeable changes in symmetry with distortions, however this range can be tuned such that they provide utility in the examination of state changes or distortions.

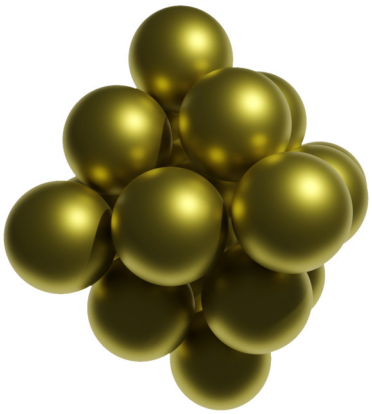

Figure 5.7: Au_{19} nano-crystallite.

The actual symmetry of the 0.1 Å distorted cluster is confirmed by tight tolerance $StoPA^{0.990}_{0.989}$ to be $100\% - C_1$. However, analysis with $StoPA^{0.99}_{0.60}$ reveals it to have 88.22% – C_s, $6.05\,\%$ – C_i, and $5.73\,\%$ – C_1 character. This indicates that the structure still has a high amount of reflection character and that the geometry is in close proximity to an invertible geometry. In contrast to the analysis of a distorted cluster, a randomly po-

Table 5.1: Continuous symmetry measurement of random distortions of Au_{19}. *(T_h symmetry is a coincidence of computer-generated random displacements of magnitude 0.001 Å.)

Magnitude of Distortion per atom of Au_{19} / Å	CSM_{95}	$STOPA^{0.80}_{0.99}$ Category	$STOPA^{0.80}_{0.99}$ Quality
0.0000	71.00	O_h	$100.00\,\%$
0.0001	67.00	O_h	$100.00\,\%$
0.0010	57.00	T_h*	$100.00\,\%$
0.0100	9.88	C_s	$100.00\,\%$
0.1000	0.95	C_s	$72.82\,\%$
1.0000	0.00	C_1	$100.00\,\%$

sitioned set of 20 atoms measured using $STOPA^{0.99}_{0.60}$ analysis, shows only $100.00\,\% - C_1$ character. This emphasises the utility of soft tolerance measures in examining symmetries for the purposes of categorisation and discrimination in automated methodologies, where comparison between similar geometries and structures can be achieved through an examination of the deviation from point group symmetry.

These similarities between symmetries can also be examined for the Au_{19} and SF_6 geometries, both of which are O_h point group. Figure 5.8 shows the σ-*SOCS*, with nine perfect planes of reflectional symmetry, as indicated by the maxima. The differences in absolute value are indicative of differences in the size of the structures, with the larger structure having greater change over a given angle and thus a lower average symmetry between axes. This can be corrected by normalisation of the longest distance between the origin and an atom. However, in terms of examining the symmetry comparatively, the similarities between the structures are readily apparent. The proximity of the Au_{19} nanocrystalite to more complex symmetries is also readily apparent, as shown by the small peaks between the maxima, referred to as the local maxima. This indicates that there is some reflection or improper rotation character at these sites which does not exist for the SF_6. Both structures indicate nine perfect reflection planes, divided into six that appear as maxima along dihedral bands, shown as yellow and orange lines in the rightmost plots of figure 5.8, and three that appear at dihedral band intersections. The periodicity of the maxima, 4, and the displacement of the maxima that lie upon intersections of the dihedral bands indicate that the set of three reflection planes are distributed orthogonally to each other with the other six being placed between them.

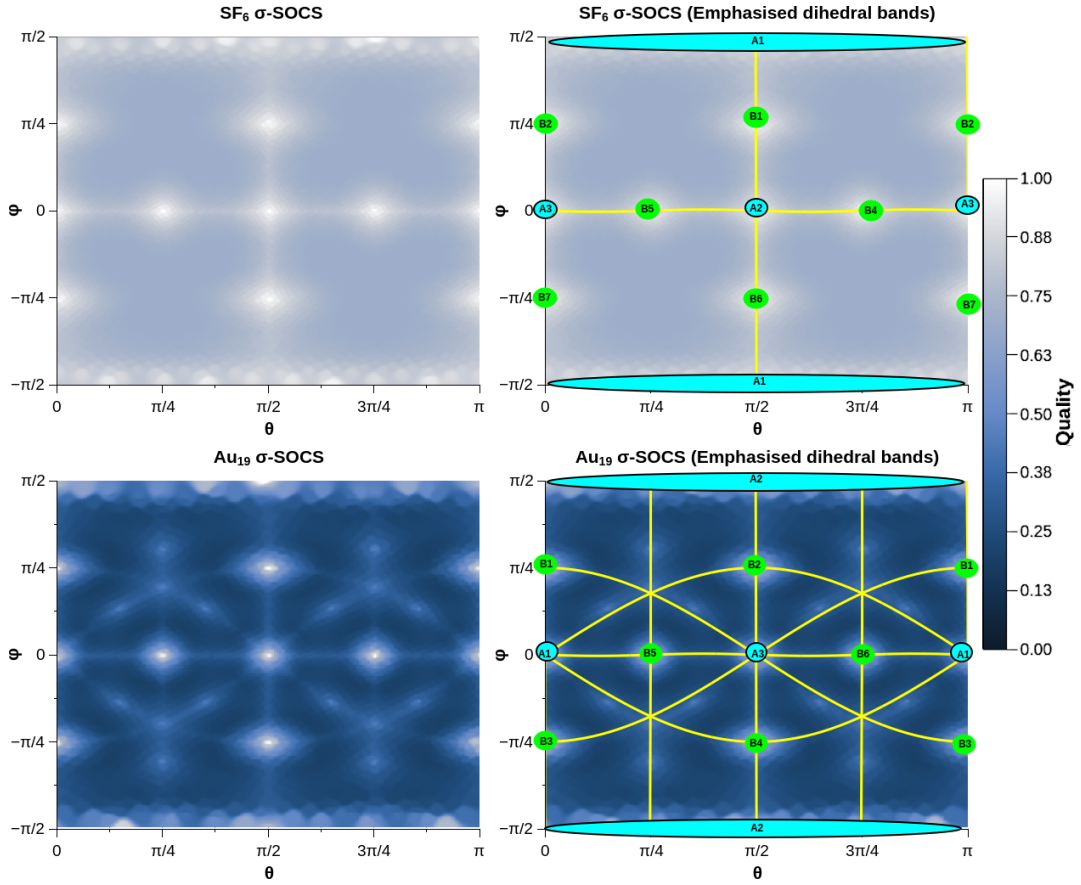

Figure 5.8: σ-*SOCS* of SF_6 (upper left), labelled σ-*SOCS* of SF_6 (upper right), σ-*SOCS* of Au_{19} (lower left), and labelled σ-*SOCS* of Au_{19} (lower right). Maxima are indicated with green and cyan circles, the dihedral bands are shown as orange lines.

This immediately shows the structure to be in the O_h point group, as both threefold and fourfold symmetries can be observed, with the threefold symmetries appearing as rectangles due to the mapping of the sphere onto a 2-dimensional plane and the smearing along the x-axis of the uppermost and lowermost points of the y-axis, labelled as point A1 and A2 in the labelled plots for SF_6 and Au_{19} respectively, shown in figure 5.8. The Au_{19} map also shows several dihedral bands that are not observed in the σ-*SOCS* of SF_6, linear arrangements of atoms that do not exist in the sulphur hexafluoride. As the dihedrals of SF_6 can be trivially attributed to the linear pairs of fluorine atoms, this indicates that dihedrals in Au_{19} can be found between the vertex Au atoms and that the edges of the cluster have atoms that are bisected by perfect mirror planes. From this it can be observed that the Au_{19} cluster has trigonal facets with three atoms to each edge. The nine dihedral bands also indicate that there are eighteen atoms that form unique dihedrals, with the nineteenth atom placed at the centre.

Sulphur hexafluoride was found to have a symmetry determined by $STOPA^{0.99}_{0.97}$ to be O_h. Examination of the symmetry indicates that the physical properties must comport with the 9 reflection planes, 13 proper rotation axes, 7 improper rotation axes, and the inversion centre. The set of unique elements in table 5.2 shows the unique elements necessary to characterise the symmetry of the molecule.

The centre of inversion, symmetry vector $O = -2$, indicates that no permanent dipole is present. Other electronic properties, such as the polarisability, can also be examined to some extent. Even without determination of the precise values of the polarisability constants, the polarisability, a 2nd rank tensor, must comport to a symmetry compatible with the O_h point group. In order to conform with the reflection and two-fold rotation, the polarisability tensor must be symmetric about the diagonal and all off-diagonal terms must be equal; this ensures that the tensor can be diagonalised to produce an isotropic polarisability, as expressed in equation 5.43. This isotropic polarisability also allows us to conclude that SF_6 is inactive under examination with Rotational–Raman spectroscopy.

Table 5.2: Irreducible symmetry vector representation of SF_6 (O_h)

Orientation vector			$SOCS_{0.95}$ components of SF_6			Order	Quality
X	Y	Z	log(-1)	log(2)	log(3)		
1.00	1.00	1.00	0	2	0	4	1.00
0.71	0.00	0.71	0	1	0	2	1.00
0.58	0.58	0.58	0	0	1	3	1.00
1.00	0.00	0.00	1	2	0	-4	1.00
0.58	0.58	0.58	1	1	1	-6	1.00
1.00	0.00	0.00	1	0	0	-1	1.00
0.71	0.00	0.71	1	0	0	-1	1.00
0.00	0.00	0.00	1	1	0	-1	1.00

$$a = \begin{pmatrix} a_{xx} & a_{xy} & a_{xz} \\ a_{yx} & a_{yy} & a_{yz} \\ a_{zx} & a_{zy} & a_{zz} \end{pmatrix} = \begin{pmatrix} a_{xx} & a_{xy} & a_{xz} \\ a_{xy} & a_{yy} & a_{yz} \\ a_{xz} & a_{yz} & a_{zz} \end{pmatrix} = \begin{pmatrix} a_{xx} & 0 & 0 \\ 0 & a_{yy} & 0 \\ 0 & 0 & a_{zz} \end{pmatrix} \tag{5.43}$$

The nineteen dihedral bands visible in the σ-*SOCS* of Au_{38}, figure 5.9, can account for all of the pairs of atoms, which, in combination with the lack of distortion of the bands, suggests that no central atom is present. Both fourfold and threefold rotations are visible and it can also be noted that, within the threefold regions, it appears that there is some degree of sixfold character. This suggests the presence of hexagonal facets with a central atom and threefold rotational symmetry, due to either the extended surface of the particle or the internal structure. This is also in agreement with the fourfold regions, which also lie upon the intersection of dihedral bands, suggesting that the reflection planes must bisect two sets of atoms arranged such that they align in the reflection plane. Overall, this suggests a truncated octohedral morphology, with square facets which are bounded by hexagonal facets, combined with an octahedral structure with the trigonal faces and vertices respectively aligned with the hexagonal and square facets of the truncated octahedron, which is consistent with the O_h point group classification.

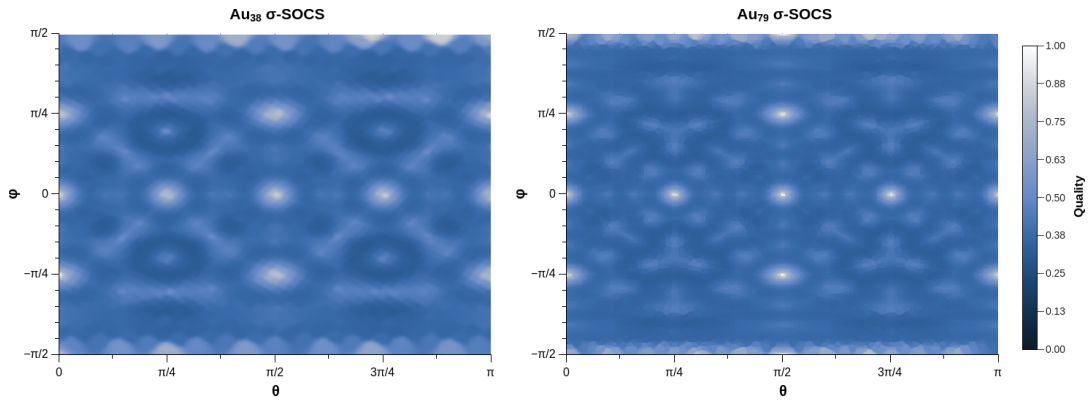

Figure 5.9: σ-*SOCS* of Au_{38} (left), and Au_{79} (right).

The σ-*SOCS* of larger structures, such as Au_{79}, figure 5.9, specific identification of the dihedral bands is more challenging due to the complexity. However, it can still be observed that there are regions of threefold and fourfold rotational character with the intersection of orthogonal dihedral bands indicating a central atom. It can also be observed that the fourfold region is bounded by three local maxima, with the central local maximum located more closely to the dihedral of the reflection plane. This suggests a smaller octahedral geometry, consistent with Au_{19}, bounded by a larger structure which is itself conformant with octahedral symmetry. The relatively low intensity of the dihedral bands linking the centre of the trigonal facets and the fourfold rotational sites, in comparison to those bands which conform with the edges of the facets, indicate that it is unlikely for the corner atoms to be present on the larger oc-

tahedral geometry. This gives the Au_{79} geometry as being a cuboctahedron, with an internal octahedron consistent with the structure of Au_{19}.

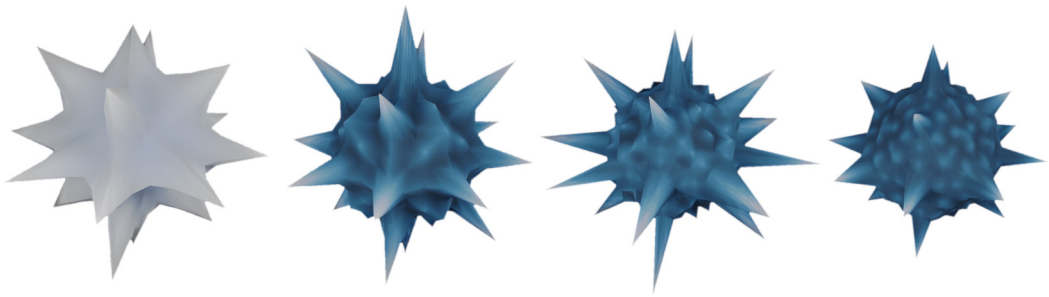

Figure 5.10: Left—right: σ-*SOCS* of SF_6, Au_{19}, Au_{38}, and Au_{79}.

As is shown in figure 5.10, representation of these maps as 3-dimensional structures can also provide immediate insight into the similarities between geometries. The comparison of the σ-*SOCS* geometries for SF_6, Au_{19}, Au_{38}, and Au_{79} shows that the structures share perfect reflectional symmetry, indicated by the position and number of the maximum peaks in the structures which exactly correspond for all of the geometries. This representation also provides a clear visualisation of the spatial relationships between maxima, local maxima, and dihedral bands.

5.3.2 Symmetry of Capping Agents and Small Molecules

5.3.2.1 NH_3

Symmetry analysis of the nuclear positions in ammonia and the centroids of the localised molecular orbitals and the nitrogen lone pair both indicate a C_{3v} point group. The symmetry of the centroids demonstrating the degeneracy and equivalence between the nitrogen-hydrogen bonds. This information can be used to determine the orientation of the dipole, which is known to occur due to the lack of inversion symmetry. For reasons of symmetry, it must occur at the intersection of the mirror planes and the C_3 rotation axis, which is consistent with the results of the DFT calculation of the dipole. The orientation of the dipole in this case being restricted to invariance under C_3 rotation about the molecular axis and also invariance within the intersection of plane of molecular symmetry, which coincide with the rotation axis.

The polarisability tensor may be constructed by defining a coordinate frame of

reference to conform to two axes of the molecular symmetry. Here the primary axis is aligned with the z-axis and the x,y-components of hydrogen—nitrogen bond are rotated into alignment with the y-axis and the tensor is then expressed as shown in equation 5.44.

$$a = \begin{pmatrix} a_{xx} & a_{xy} & a_{xz} \\ a_{yx} & a_{yy} & a_{yz} \\ a_{zx} & a_{zy} & a_{zz} \end{pmatrix} \tag{5.44}$$

Application of symmetry transformation matrices allows for the relationship between the tensor constants to be examined. Applying a reflection through the yz-plane, σ_y as shown in equation 5.45, determines that the terms a_{xy}, a_{yx}, a_{yz}, and a_{zy} are necessarily equal to 0.[96,128]

$$a = \begin{pmatrix} a_{xx} & a_{xy} & a_{xz} \\ a_{yx} & a_{yy} & a_{yz} \\ a_{zx} & a_{zy} & a_{zz} \end{pmatrix} = \sigma_y \begin{pmatrix} a_{xx} & a_{xy} & a_{xz} \\ a_{yx} & a_{yy} & a_{yz} \\ a_{zx} & a_{zy} & a_{zz} \end{pmatrix} \sigma_y^T = \begin{pmatrix} a_{xx} & -a_{xy} & a_{xz} \\ -a_{yx} & a_{yy} & -a_{yz} \\ a_{zx} & -a_{zy} & a_{zz} \end{pmatrix} \tag{5.45}$$

Application of the rotated reflection transformation, σ_2, further demonstrates that the a_{xx} and a_{yy} terms must be equal and that the a_{zx} and a_{xz} must also be equal to zero, equations 5.46 and 5.47.

$$a = \begin{pmatrix} a_{xx} & a_{xy} & a_{xz} \\ a_{yx} & a_{yy} & a_{yz} \\ a_{zx} & a_{zy} & a_{zz} \end{pmatrix} = \begin{pmatrix} a_{xx} & 0 & a_{xz} \\ 0 & a_{yy} & 0 \\ a_{zx} & 0 & a_{zz} \end{pmatrix} \tag{5.46}$$

$$a = \sigma_2 \begin{pmatrix} a_{xx} & a_{xy} & a_{xz} \\ a_{yx} & a_{yy} & a_{yz} \\ a_{zx} & a_{zy} & a_{zz} \end{pmatrix} \sigma_2^T = \begin{pmatrix} a_{xx} & 0 & 0 \\ 0 & a_{xx} & 0 \\ 0 & 0 & a_{zz} \end{pmatrix} \tag{5.47}$$

This gives the form of the polarisability tensor, a, which is consistent with the diagonal components of the tensor predicted by coupled perturbed self-consistent field, CPSCF, analytic calculation of the diagonalised ammonia tensor, equation 5.48.

$$a_{\text{CPSCF}}(NH_3) = \begin{pmatrix} 12.688 & 0 & 0 \\ 0 & 12.689 & 0 \\ 0 & 0 & 13.094 \end{pmatrix} \tag{5.48}$$

5.3.2.2 Methanol, Methane, Chloromethane, and Dichloromethane

Symmetry analysis of methanol optimised with Density Functional Theory (DFT) indicated it to be in the C_s point group with a mirror plane passing through the oxygen and carbon atoms. Soft tolerance point group assignment, $StoPA_{0.5}^{0.99}$, found the molecule to be consistent with C_s at a 97.31% limit of confidence. There was also a 2.69% C_1, indicating that some atoms were slightly deviated towards asymmetry. To further examine the nature of this deviation, the symmetry of the atoms with respect to the reflection plane was examined with Single Atom Symmetry. This indicated that all atoms were highly symmetric with respect to the reflection plane, however, as shown in table 5.3, some deviations from perfect symmetry were observed. The hydrogen atom bisected by the reflection plane, $H_{(2)}$, showed some deviation, indicating a small positional change relative to the reflection plane that best describes the other atoms. The continuous symmetry for the molecule at $CSM_{0.95}$ was found to be 0.9895, indicating that a reflectional transformation through the plane would result in near exact equivalence in position, this slight discrepancy likely due to slight relative rotations of the alcoholic proton relative to the O—C dihedral.

Table 5.3: Single atom symmetry for methanol ($SAS_{0.95}$)

Atom	$SAS_{0.95}$ / a.u.
$H_{(0)}$	0.985
$H_{(1)}$	0.985
$H_{(2)}$	0.980
$H_{(3)}$	0.990
C	0.997
O	0.987

The centroids of localised molecular orbitals, which give the weighted centre of the electron densities of each localised orbital, were produced using the the Pipek-Mezey methodology.[87] The centroids also examined using the symmetry analysis techniques

to gain insight into the symmetry of the bonding orbitals and the lone pairs on the oxygen. These were also found to be consistent with a C_s point group, with 88.87% confidence, and also 11.13% C_1 character indicating a slightly greater degree of asymmetry than that of the atomic positions. The reflection plane was again found to be of high quality, with a $CSM_{0.95}$ of 0.9568, although again slightly lower than the symmetry of the nuclear position. This shared symmetry of the atomic position and electronic structure is consistent with the predictions of Neumann's theory, which specifies that the symmetry of the electronic structure must be compatible with the symmetry of the overall system.[96,131] Neumann's theory, which states that if the structure of a molecule is invariant with respect to a given symmetry, that any properties must also be invariant with respect to that symmetry.[96] An example of this is that the existence of a single plane of reflectional symmetry for both the nuclear positions and the orbital centroids, shows that a permanent dipole must exist. By a qualitative application of Neumann's theorem it can also be determined that it must lie within the plane of reflection, as the matrix elements that do not lie in plane must necessarily either cancel or be zero, which is consistent with the DFT calculated dipole moment for methanol.

Symmetry analysis with SAS_l of two distorted geometries of chloromethane, which correspond to extrema of infrared active vibrational modes, provides insight into the specific modes of the vibration without requiring the vectors of the vibrational motion to be examined. The initial geometry of the chloromethane conforms to the C_{3v} point group with mean $SAS_{0.95}$ scores of 5.996 ± 0.004. The displacement geometry of the 3160 cm^{-1} vibrational mode with a mean $SAS_{0.795}$ score of 0.787 ± 0.220. The larger range of scores, and their low value, indicate asymmetry; this is consistent with the $STOPA^{0.99}_{0.80}$, which determined the point group to be 100% C_1. Examination of the symmetry vectors of the 3160 cm^{-1} geometry, table 5.5, indicated a reflection plane of 80% confidence was the only symmetry element contributing to the SAS score. From this, it is possible to determine that the mode is an asymmetric stretch of the $H_{(0)}$ and $H_{(1)}$ atoms. It also indicates a small displacement of the carbon atom, which further supports this being an asymmetric stretch. The SAS of the $H_{(2)}$ and Cl atoms indicates that these have much smaller distortions with respect to the reflection plane. It should be noted that in-plane distortions of the Cl and $H_{(2)}$ atoms are not necessarily visible from these scores and that a more detailed examination of the lower lying symmetry elements would be required in order to fully resolve this mode. However, this is sufficient to identify the mode as being primarily an asymmetric stretch of the

$H_{(0)}$—C—$H_{(1)}$ bonds.

The same analysis technique can also be applied to the 3161 cm^{-1} displacement geometry. The symmetry vector again indicates a reflection plane and it can be seen that the $H_{(0)}$ and $H_{(1)}$ both display a similar distortion. Combined with the C_s character found by the $STOPA^{0.99}_{0.80}$, this distortion suggests a symmetric stretching mode. It should be noted that the distortion in the $H_{(0)}$ relative to the reflection plane likely indicates that this bond is undergoing an asymmetric stretching mode relative to the other C—H bonds. The advantage of this form of analysis becomes more apparent if, rather than using extrema in which the displacements are visible upon cursory inspection, a smaller displacement is used, 0.01% of the maxima, table 5.5. These geometries appear indistinguishable with a root mean square deviation ($RMSD$) of only 0.0039 Å, however symmetry analysis allows clear insight into the types of distortion.

Table 5.4: Single atom symmetry (SAS_l) of chloromethane (equilibrium) and the maximum distortion

	SAS_l		
		Vibrational mode	
	Equilibrium Geometry	3161 cm^{-1}	3160 cm^{-1}
$l =$	0.95	0.80	0.89
$H_{(0)}$	6.00	0.57	0.69
$H_{(1)}$	6.00	0.65	0.69
$H_{(2)}$	5.99	0.75	1.00
C	6.00	0.75	1.00
Cl	6.00	0.97	1.00
$STOPA^{0.99}_{0.80}$	100% - C_{3v}	100% - C_1	45.94% - C_S , 54.06% - C_1

Table 5.5: Single atom symmetry (SAS_{95}) of chloromethane (equilibrium) and the 1% distortion geometry of the 3161 cm^{-1} vibrational mode

	$SAS_{0.95}$	
	Equilibrium Geometry	Vibrational mode 3161 cm^{-1}
$H_{(0)}$	5.995	2.958
$H_{(1)}$	5.995	2.960
$H_{(2)}$	5.992	2.949
C	5.999	2.987
Cl	5.999	2.987
$RMSD$	—	0.0039
$STOPA^{0.99}_{0.80}$	100% - C_{3v}	100% - C_s

In figure 5.11 the reflection symmetry-orientation cross-sections (σ-SOCS) of methane, chloromethane, and dichloromethane are shown. Despite methane, chloromethane, and dichloromethane being in significantly different point groups and having distinct substituents, the σ-SOCS of these molecules indicates similar morphologies. Methane shows six unique planes of reflection, indicated by maxima in the σ-SOCS projection. These maxima are linked by four unique dihedral bands, which indicate planes that bisect atoms but are not true reflections. Given the number of atoms, this indicates that the geometry must be a single central carbon atom with four identical hydrogen substituents arranged such that H—C—H bonds are not linear, as a square configuration would cause only two dihedral bands to form. The periodicity of the maxima, with three occurring on each dihedral band, indicates that the atoms must necessarily be arranged in a trigonal configuration relative to each dihedral which is in accordance with the known tetrahedral geometry of methane.

As with methane, chloromethane shows four dihedral bands indicating four atoms arranged around a central atom. Examination of the maxima of the σ-SOCS indicates that a periodicity of three about the dihedral, showing three equivalent atoms located in a trigonal configuration about a fourth distinct atom. This suggests a tetrahedral configuration with one inequivalent atom breaking the tetrahedral symmetry. The overall lower value of the background symmetry and the lower values of the dihedral bands which do not contain maxima also indicate that the carbon atom has been moved away from the geometric centre. This shows that the C—Cl bond length is

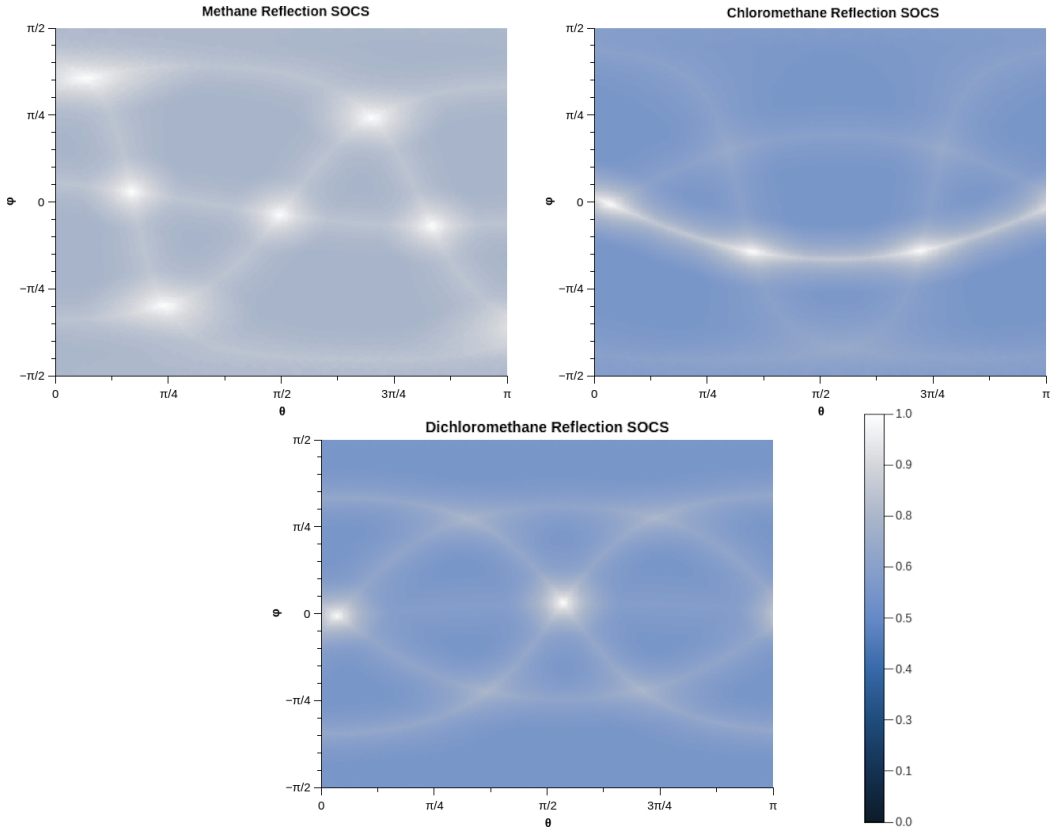

Figure 5.11: σ-SOCS of methane (top left), chloromethane (top right), and dichloromethane (bottom).

unique, as the dihedral lines for any equivalent bonds would be of equal intensity. For this reason, it also indicates equivalence between the C—H bonds due to the common dihedral band intensity.

The σ-SOCS of dichloromethane also has four significant dihedral bands, which indicates four substituents, and two maxima, indicating two distinct planes of reflection. The dihedral bands that meet to form maxima can naturally be partitioned into two pairs, indicating two inequivalent pairs of equivalent atoms, with the distinction between the pairs being indicated by the lack of maxima at the crossing points of the dihedral bands. The orthogonality of the reflection planes is apparent, due to the theta spacing of the maxima. This indicates the doubly substituted tetrahedron with the difference in height of the dihedral bands indicating two pairs of bond lengths. The fifth dihedral band, which is significantly less symmetric than the first, arises due to a significant deviation of the carbon atom from the geometric centre, also indicating the inequivalent character of the pairs of bonds in the structure.

5.3.2.3 Cyclic and Aromatic Molecules

From the examination of the σ-SOCS of benzene, shown in figure 5.12, it is immediately apparent that this is a high symmetry structure with sixfold rotational symmetry. Clear differences can be observed between the dihedral and non-dihedral reflection planes. As such, benzene can be considered an archetypal six-fold cyclic, C_{6h}, against which other structures may be compared.

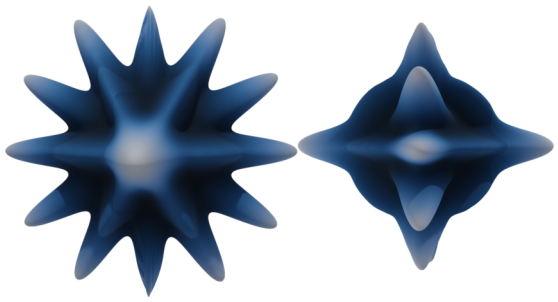

Figure 5.12: σ-*SOCS* of benzene.

In comparison to benzene, cyclohexane shows traits consistent with the the perfectly symmetrical six-membered ring. Perfect reflection planes can be observed to bisect the structure of cyclohexane orthogonally to the plane of the reduced six-fold symmetry. Furthermore, this can be observed to be consistent with the chair configuration of cyclohexane, as perfect reflection planes are only present in one direction. The distortion of the ring can also be observed to spread and decrease the the quality of the σ_h plane.

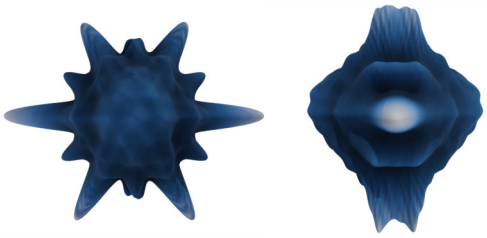

Figure 5.13: σ-*SOCS* of cyclohexane (chair configuration).

Similarly to cyclohexane, other structures that can be considered to be symmetrical derivatives from benzene. The σ-SOCS of phenol, figure 5.14a, and pyridine, figure 5.14b, both show similarities in symmetry that are unobservable through strict discrete point group assignment. It can be observed that both show local reflectional

maxima that are consistent with a six-member ring. For phenol it can be observed that, excluding the near-perfect maxima of the ring reflectional planes, the other ring maxima show similar distortions and angles relative to the centre as benzene. This suggests that the ring is largely undistorted. The decrease in reflection plane values around the entire ring shows that the hydrogen atom of the phenol must be unaligned with the oxygen—ring bond, however, the high quality of the σ_h shows the the atom must be in plane with the ring.

For pyridine it can be observed that a six membered ring is still present, however, the relative angles of the imperfect ring maxima show a distortion from the arrangement of atoms found in benzene. The presence of a dihedral band indicates precisely the position of the nitrogen atom and also that the hydrogen atom of the carbon opposite the nitrogen substitution is in-plane with the ring.

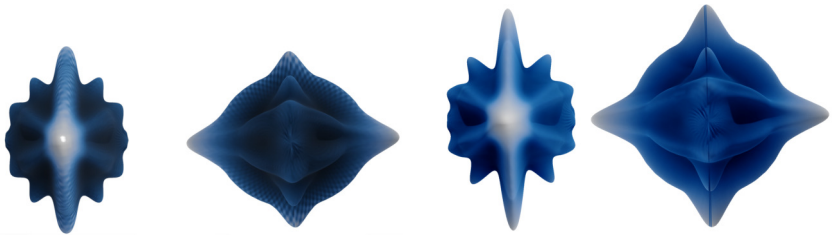

(a) (b)

Figure 5.14: σ-*SOCS* of phenol (a) and pyridine (b).

The stark contrast between symmetry maps of different structures is emphasised by comparison of the maps of cyclic molecules with that of non-cyclic structure, such as P_4O_{10}, as shown in figure 5.15.

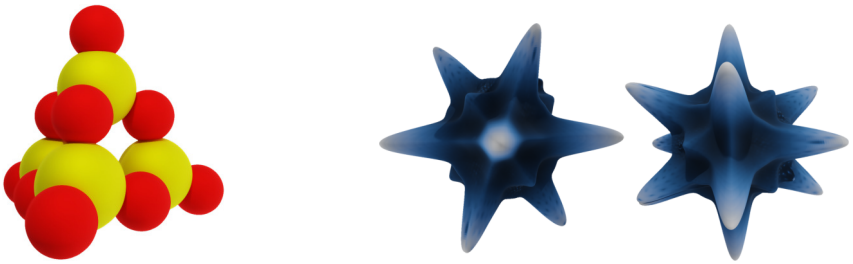

(a) (b)

Figure 5.15: Structure (a) and σ-*SOCS* (b) of P_4O_{10}.

5.3.3 Symmetry of Dynamic Processes

5.3.3.1 Ethanol

The symmetry analysis methodologies presented in this chapter provide not only insights into static geometries but also form a practical set of methodologies for interpreting dynamic processes. Figure 5.16 shows the $STOPA^{0.999}_{0.000}$ assignment values for ethanol during a molecular dynamics trajectory. From this it is readily apparent when changes between states occur and also when oscillations, vibrations, or other distortions take place.

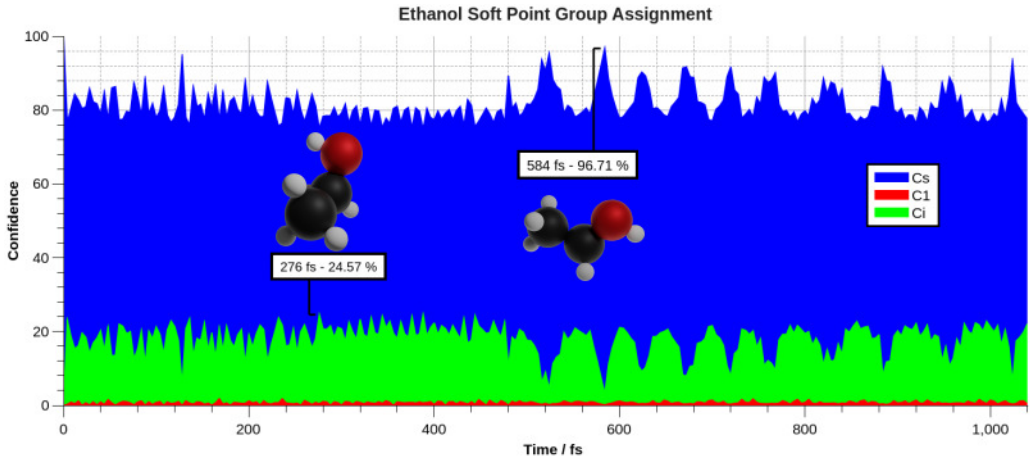

Figure 5.16: Symmetry classification of ethanol during molecular dynamics trajectory.

Comparison with current methodologies such as $RMSD$, as is shown in figure 5.17, indicates that symmetry analysis provides easier interpretation. Although methods such as $RMSD$ measures are capable of distinguishing both large and small structural deviations, alterations in geometry can prove difficult to analyse for small changes, which can be masked by larger structural conformational alterations. Applying symmetry analysis to dynamic processes solves these problems by being sensitive to state without requiring discrete or explicit categorisation. This provides a useful tool in the analysis of molecular dynamics where molecules or regions of large species, such as proteins, can be analysed over the duration of a trajectory and immediately interpreted to find chemically significant configurations. These traces can also be integrated within a specified confidence range in order to analyse the duration specific states are occupied over the course of a trajectory.

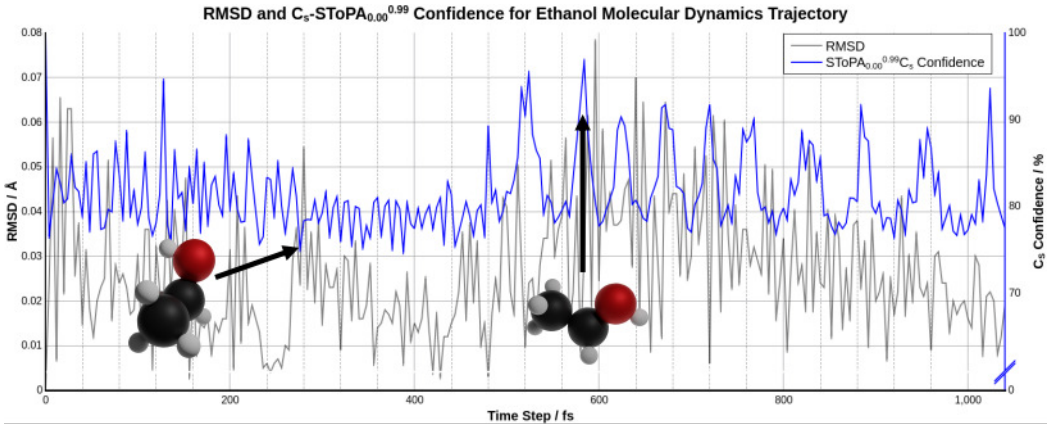

Figure 5.17: Symmetry classification of ethanol compared with RMSD during molecular dynamics trajectory.

5.3.3.2 Cyclohexane

A further example of the application of symmetry measurement to a dynamic system is given for cyclohexane. The initial exact configuration was measured using STOPA$^{1.00}_{0.98}$ as D_{3d}, however during the dynamics trajectory this symmetry was actually not observed, with tight tolerance assignment showing C_1, asymmetry and soft tolerance showing greatest proximity to C_s. The initial period of equilibration did show some significant C_{3h} and C_{2h}, plotted collectively as C_{nh} in figure 5.18. For the majority of the trajectory the symmetry was found to be most consistent with C_s, indicating near-reflectional character, with some contributions from C_i, indicating a centre of near-inversion.

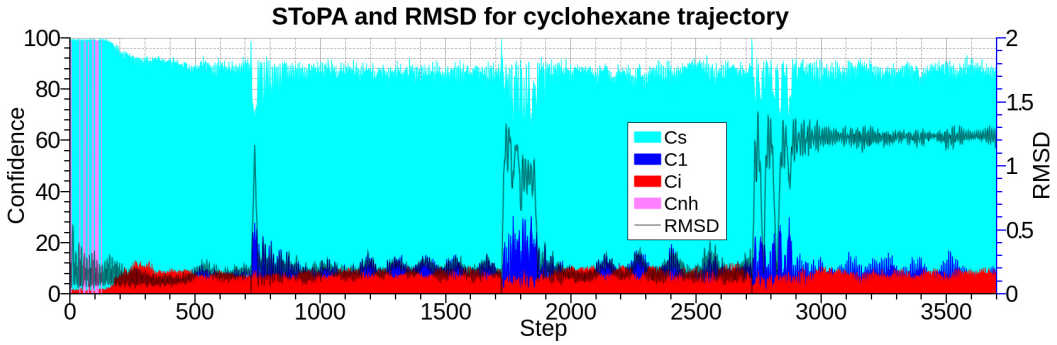

Figure 5.18: Full-width STOPA (STOPA$^{1.00}_{0.00}$) classification of cyclohexane compared with RMSD during molecular dynamics trajectory.

Both the RMSD and the STOPA analysis show two notably distinct states, which arise from a decrease in reflectional character. In order to examine the changes in symmetry that occurred, a short excerpt of the trajectory where significant change in

symmetry is observed, steps 2738 — 2742, were selected for closer examination. The SToPA and RMSD analysis of this period are shown in figure 5.19.

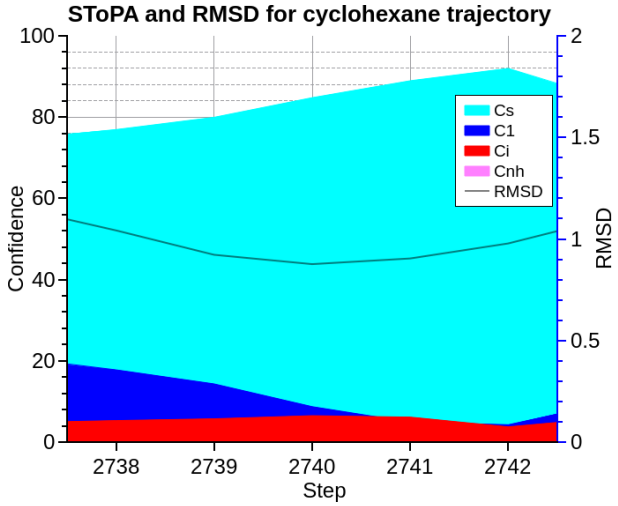

Figure 5.19: Full-width SToPA ($\text{SToPA}_{0.00}^{1.00}$) classification of cyclohexane compared with RMSD for the steps 2738 — 2742 of the molecular dynamics trajectory.

Figure 5.19 shows that the structure transitions from a relatively low C_s, high C_1 geometry towards a high C_s, low C_1 geometry during this period. This is an increase in reflectional symmetry and a decrease in random distortion, the changes from step 2738 — 2742 introduced stronger reflectional character. The relatively high degree of C_s symmetry throughout shows that the mirror planes, although distorted from complete symmetry, are largely present during these steps, a product of the constraints upon distortion that are imposed by the cyclic structure.

Analysis of cyclohexane using low- or no-threshold SAS was also undertaken. The no-threshold Single Atom Symmetry, $\text{SAS}_{0.00}$, has been sampled using a uniform grid of $10,000$ points distributed evenly on the surface of the unit sphere. In contrast to the high-threshold SAS employed above which shows high symmetry with high confidence scores and low divergence, low-threshold SAS shows high symmetry by lower scores combined with low divergence between atoms of the same element. Symmetrical geometries show more equivalence between atoms, as they can be transformed by the same symmetry operations. High symmetry also causes sharper resolution upon the intersections between dihedral bands, low threshold SAS measures the sharpness in the intersections of dihedral bands, which would coalesce were the symmetry elements present.

The $SAS_{0.00}$ analysis, shown in figure 5.20, clearly delimits the differences in symmetry that are observed during the initial equilibration, subsequent heating, and then the later production phases of the dynamics run. The production phase clearly shows sustained periods of high asymmetry punctuated by short-duration increases in symmetry that are comparable to the equilibration phase. This is evident for the entire molecule, with sharp troughs of low-divergence between the atoms being visible in both the carbon and hydrogen $SAS_{0.00}$ traces, respectively shown in figures 5.20b and 5.20c. This indicates that increased temperature results in a higher degree of average asymmetry.

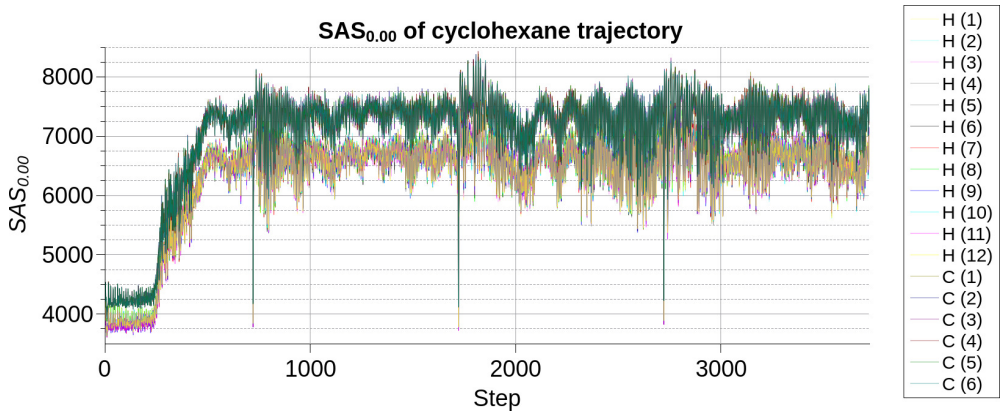

(a)

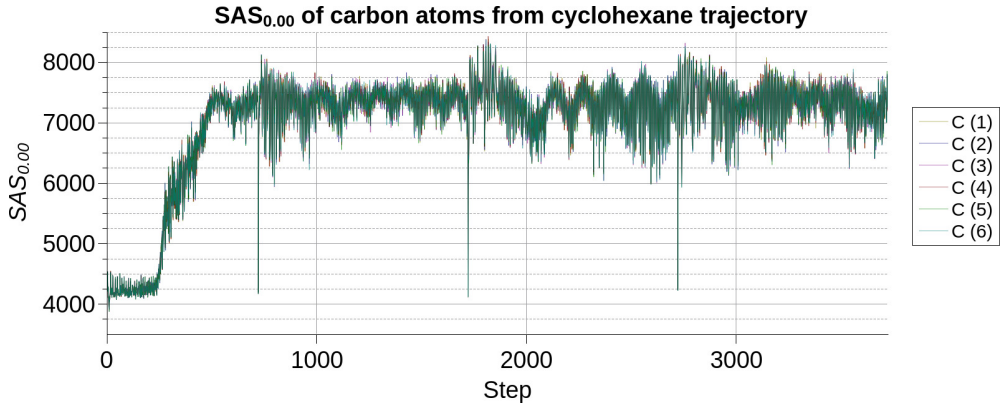

(b)

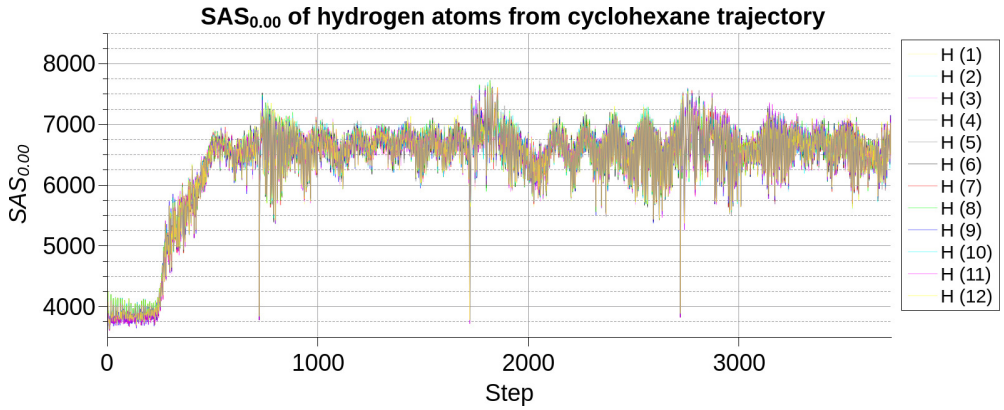

(c)

Figure 5.20: Single atom symmetry, $SAS_{0.00}$, of cyclohexane molecular dynamics trajectory. (a) shows the $SAS_{0.00}$ for all the atoms of cyclohexane, (b) shows the $SAS_{0.00}$ for the carbon atoms of cyclohexane, and (c) shows the $SAS_{0.00}$ for the hydrogen atoms only.

Comparison of the low-threshold $SAS_{0.45}$ and the high-threshold $SAS_{0.75}$, respectively shown in figures 5.21a and 5.21b, indicates that steps 2738 and 2739 have a high degree of inequivalence between atoms and a high degree of smearing of the dihedral band intersections. The decrease in $SAS_{0.45}$ between steps 2738 and 2741 shows an increase in equivalence between atoms and a decrease in dihedral band intersection smearing, this corresponds with an increase in $SAS_{0.75}$. These changes together indicate an increase in symmetric character for the molecule.

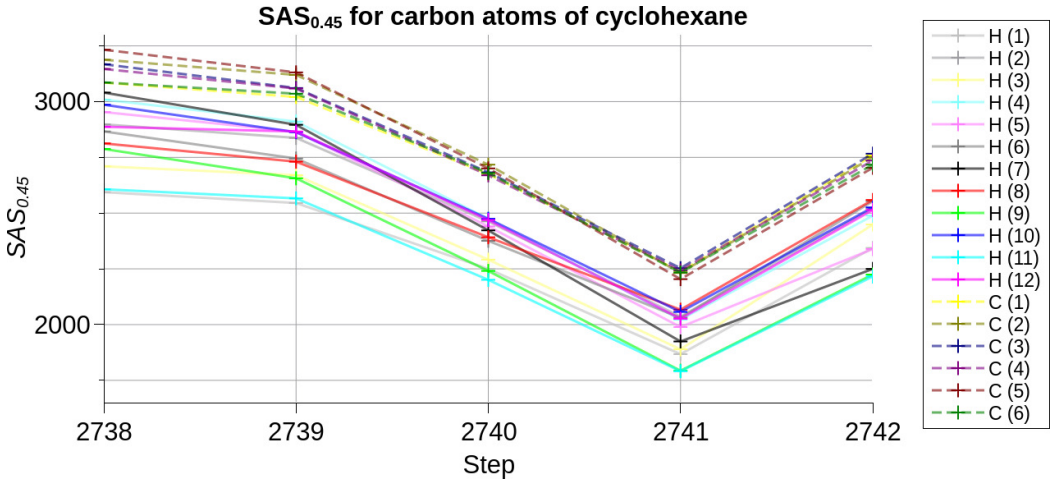

(a) $SAS_{0.45}$

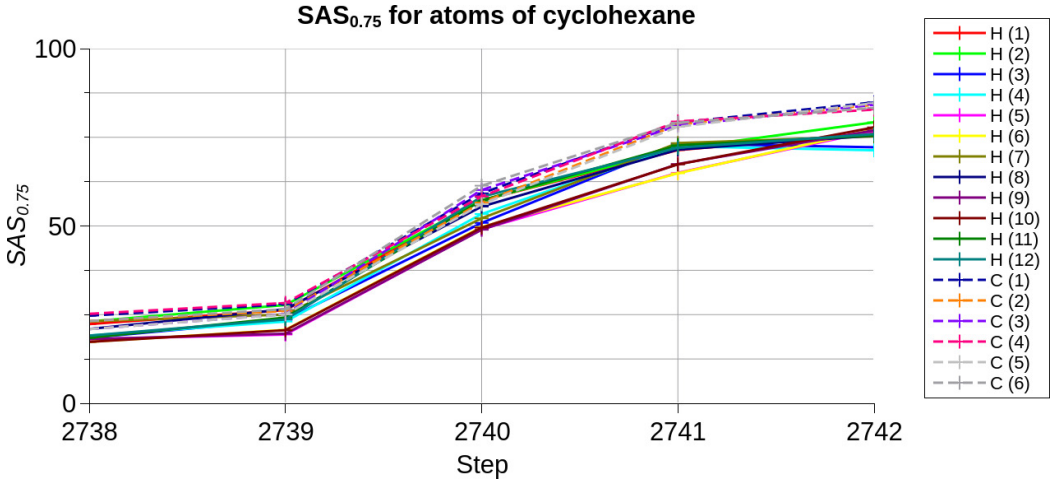

(b) $SAS_{0.75}$

Figure 5.21: Single atom symmetry analysis of cyclohexane molecular dynamics trajectory, showing the steps from 2738 to 2742.

The examination of the divergence shown in the violin plot of the $SAS_{0.75}$, figure 5.22, indicates significant changes in the grouping of atoms by symmetric equivalence. The carbon atom conformation for step 2738 shows a very broad clustering with some

significant outliers, which changes to form a tighter cluster of higher symmetry as the trajectory progresses, indicating that the carbon atoms become more symmetric. At step 2738 the hydrogen atoms show two, unequally sized, clusters of symmetry, indicating two distinct groupings of hydrogen atoms with some variation within those groups. It should be noted that higher tolerance values incorporate less of a measure of the smearing of symmetry within the system and so distinctions between the different atoms would be reduced and the clustering becomes tighter as fewer low symmetries are accepted.

The differences between these groups decreases during step 2739 but become more apparent again during steps 2740 through to step 2742. This is combined with an increase in the mean symmetry of the hydrogen atoms that is consistent with an increase in symmetry of the molecule. The clustering present in steps 2741 and 2742 indicates that the majority of atoms become more similar and symmetric with a minority that remain less symmetric. This is consistent with a switch of geometry towards a chair-like configuration with a majority of hydrogen atoms being in similar environments and four, those bonded to the outlying carbon atoms, distinct from the other hydrogen atoms but showing similar symmetries to each other.

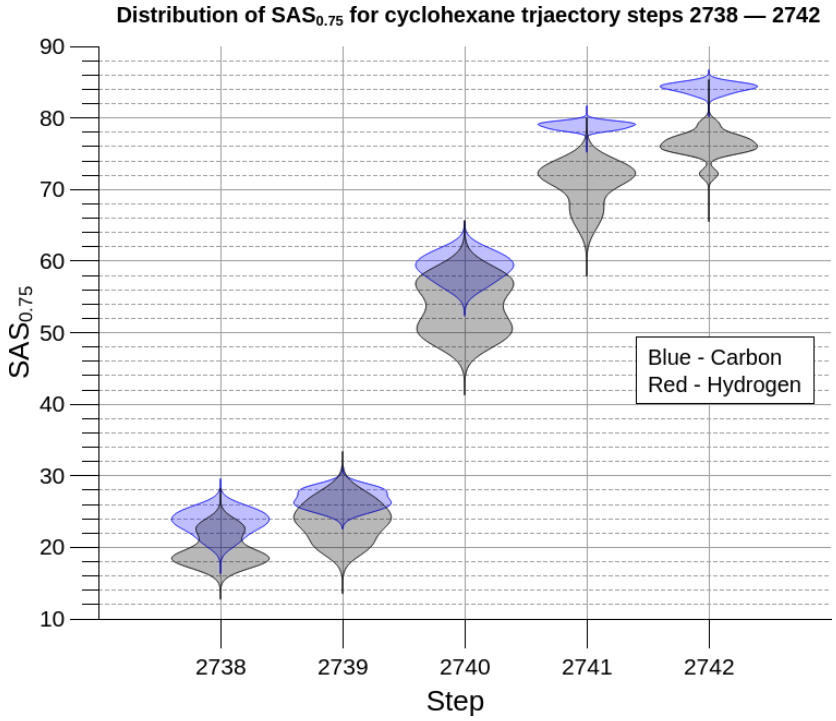

Figure 5.22: Violin plot of $SAS_{0.75}$ for cyclohexane molecular dynamics trajectory steps 2738 to 2742.

The precise nature of the change in symmetry can be further examined through comparison between the σ-SOCS analysis of the dynamics trajectory and that of the chair configuration of cyclohexane, shown in figure 5.13. From this comparison, it can be observed that throughout the course of the dynamics trajectory the symmetry is rarely more than superficially similar to the time-averaged chair-conformation. The appearance of a broad single peak orthogonal to the other, more consistently present, reflectional symmetries indicates that the system adopts significant planar character, similar to the symmetry of benzene, figure 5.12, or phenol, figure 5.14a.

The breadth of the central peak, combined with an asymmetrical distortion of the dihedral bands indicates that there is a rotational distortion of the hydrogen atoms about the plane of the ring. The presence of one particularly sharp peak with a strong dihedral band indicates that the distortion resembles the symmetry of pyridine or phenol, suggesting carbon atoms within one specific mirror plane orthogonal to the plane of the ring are particularly responsible for breaking symmetry in comparison to the other carbon atoms.

There is an increase in the reflectional symmetry of the mirror through the ring

of the molecule during the trajectory, which shown by a decrease in the radius and increase in the central dihedral intersection shown in figures 5.24 in comparison with the same region in figure 5.23. Furthermore, there is an increase in sharpness of the dihedral intersections of the mirror planes around the molecule, which is consistent with an atom moving into the plane of the ring.

Interpretation of the σ-SOCS is consistent with the SToPA analysis, shown in figure 5.19, which indicates a strengthening of the reflection planes that move the geometry closer to the C_s point group and further from C_1.

Steps 2741 and 2742 shows significant similarity to the symmetry of chair cyclohexane, shown in 5.13, combined with the symmetry of benzene, shown in figure 5.12. This suggests a conformation that is chair-like but significantly planar in comparison to the typical chair conformation. As would be expected, these findings are consistent with the observed geometries, which show significant planar character during the transition between the envelope-like and chair-like configurations. The advantage of applying measures of symmetry rather than using RMSD is that once the common symmetry states have been analysed the trajectory can be easily interpreted and understood by the measures alone, whether that is using the SOCS, SAS, or SToPA measures or a combination thereof.

This application of continuous symmetry measures to the dynamics trajectories shows how, depending upon the properties or characteristics of interest, different measures may be used to identify specific geometric configurations. The quantification of the relative prevalence of specific conformations is also easily achieved, as the SToPA or SAS measures can be integrated within upper and lower bounds. Similarly, through differentiation of the traces produced by these measures, periods of fluctuation between distinct symmetry states can be quickly identified.

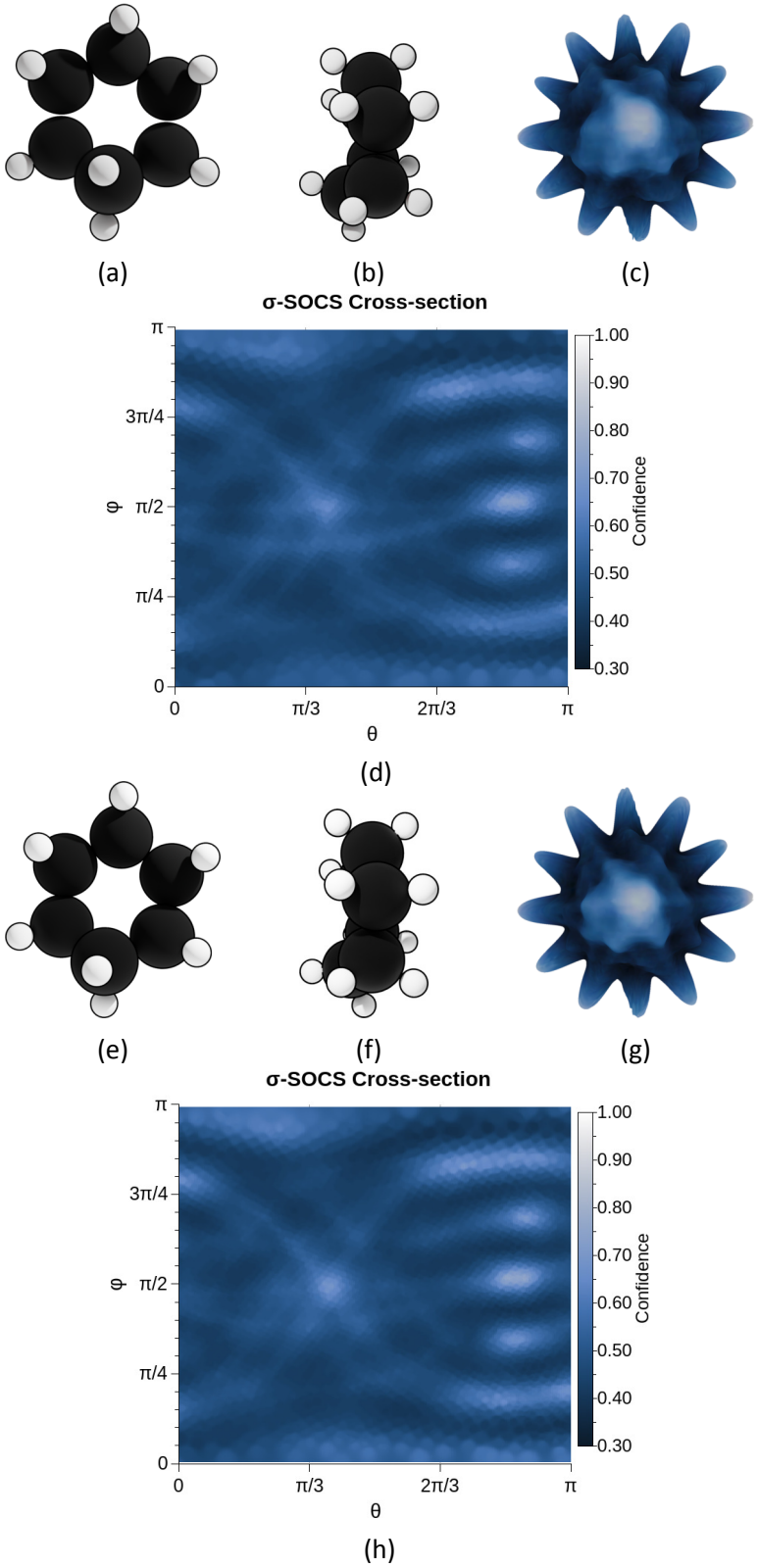

Figure 5.23: Cyclohexane geometry for step 2738, front, (a) and side, (b), and, for step 2739, front, (e), and side, (f). The 3D σ-SOCS of the 2738 and 2739 steps are shown as figures (c) and (g) respectively. The σ-SOCS map for steps 2738 and 2739 are, respectively, labelled as (d) and (h).

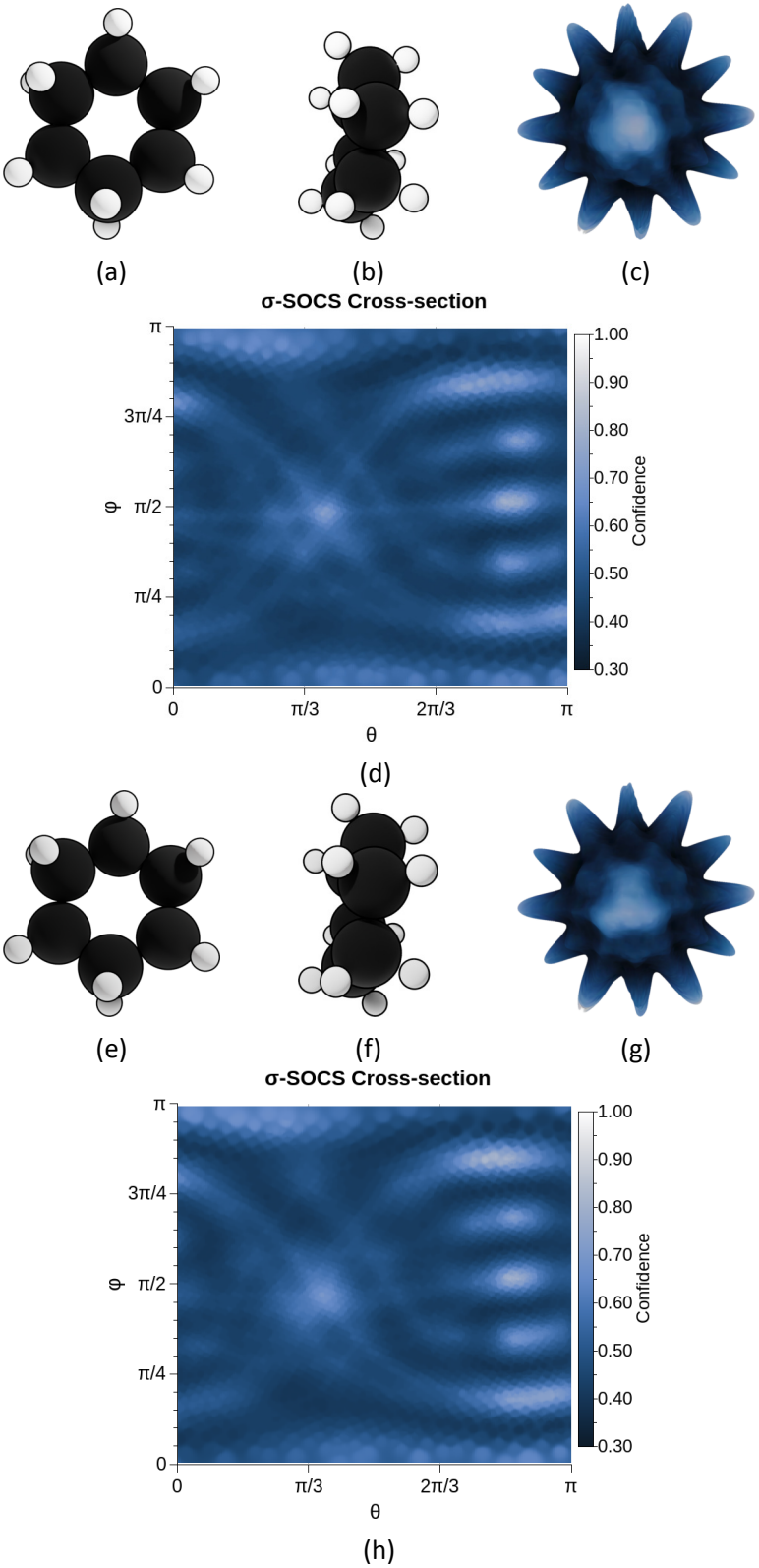

Figure 5.24: Cyclohexane geometry for step 2740, front, (a) and side, (b), and, for step 2741, front, (e), and side, (f). The 3D σ-SOCS of the 2740 and 2741 steps are shown as figures (c) and (g) respectively. The σ-SOCS map for steps 2740 and 2741 are, respectively, labelled as (d) and (h).

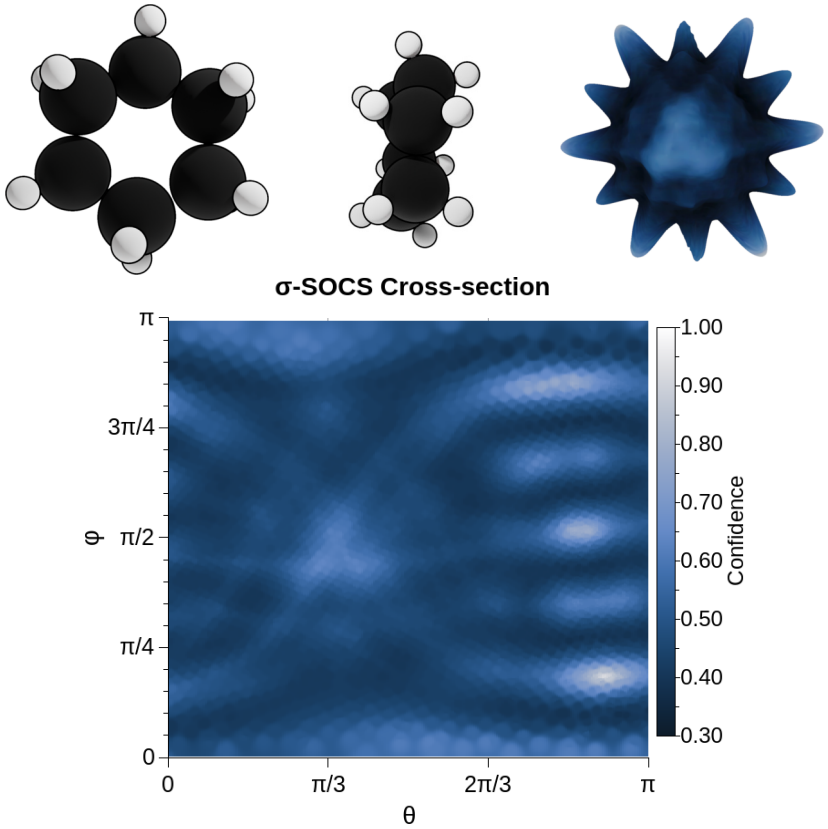

Figure 5.25: Thermally excited cyclohexane from molecular dynamics trajectory, geometry 2742 shown top left and top middle. The 3D σ-SOCS of the geometry and σ-SOCS map are respectively shown at the top right and bottom middle.

5.4 Conclusions

This chapter presents a symmetry analysis tool, IPSA, and demonstrates the capability of this software to characterise systems up to the size of small nanoparticles. It also introduces several novel measures of symmetry, which include a Continuous Symmetry Measurement, Single Atom Symmetry comparisons, Symmetry Orientation Cross-Sections and Soft Tolerance Point-Group Assignment. It also discusses how these measures can be considered compatible with group theory and also how they present unique insights into an aspect of chemistry that, whilst being foundational to many areas, is often overlooked. This work also introduces a new conceptualisation of symmetry, the vector representation. This, to the best of the author's knowledge is an entirely unique way of understanding group theory and continuous symmetry within one framework that opens up the exploration of symmetry using tools such as geometric algebra.

The measures were also used in the examination of a thermally excited cyclohexane molecule, which demonstrated that, through the application of the novel symmetry analysis techniques introduced in this chapter, distinct states can be easily characterised and the changes in geometry of the molecule or the equivalence and behaviour of individual atoms can be examined during dynamic processes. This is suggested to have particular relevance to the study of transition states and specific conformations during time periodic or dependent phenomena. Nanoparticle time-crystals or symmetry changes that occur during reactions can be readily identified and separated from other thermal fluctuations, which presents continuous symmetry measurement as advantageous to other geometric comparison measures for the analysis of long-duration trajectories.

The applications of these techniques are not limited solely to chemistry and it is expected that these may prove useful in other fields such as biology, physics, and mathematics. This provides a unique tool for automated characterisation, analysis of symmetry, and also as tool for gaining greater insight into other techniques, such as molecular dynamics, signatures within protein structures, and the interpretation of experimental techniques such as polarised spectroscopy.

Future work upon this topic will expand the applications to tiling and frieze symmetries such that space groups, periodic systems, and infinite crystal structures may also

be included in the analysis. A methodology for examining densities is also being considered based upon characterising equivalence within the gradients of the electronic structure similar to the work of Bader upon atoms in molecules theory.

Chapter 6

Conclusions

This study examines aspects of noble metal nanocrystallites from seeding through to characterisation of the concerted properties of the small nanoparticles. It demonstrates the importance of capping agents and chemical environment to the structure and morphology of nanoparticles, as these can remain bound to the reactants and exert a directing effect upon the growth processes. Strongly bound capping agents can significantly alter the geometries of the formed nanoparticles despite exerting little effect in terms of oxidation and reduction upon the molecular precursors.

The experimentally observed differences between the O- and N-containing ligands were interpreted through theoretical modelling and it was further determined that 1,3-aminopropanol reacts with the molecular precursors to form a $Pd(II)Cl_3AP$ complex prior to nanoparticle formation. The strength of this interaction is such that the aminopropanol ligand is able to direct the growth processes during the subsequent reduction by stabilisation of the Pd(100) facets. This creates a directing influence upon the shape of the resultant metal nanoparticles. The application of DFT, and TD-DFT modelling allowed for the determination of the coordination structures and also provided insight into the potential species that could be formed following reduction to form the nanoparticles. These model systems provide an insight into the interaction of the larger capping agents containing these moieties and also provides a furthered understanding of how capping agents do not just stabilise nanoparticles but can exert significant influence upon their resulting morphologies.

The importance of the alteration of surface phenomena is further emphasised in the analysis of the van de Waals surface of the Au_{19} nanoparticle. This indicated that

small gold nanoparticles present unique differences to the smaller molecular species, showing a greater degree of surface lability and metallicity. This indicates the size dependent properties of small nanoparticles do distinguish them from smaller gold species and also that their electronic structure is potentially uniquely suited to catalytic activity, through the creation of distinct sites upon the van de Waals surface that can interact with a diverse range of reactant molecules.

Analysis of the descriptors of bonding environment as described at the critical points of the gradient of the electron density also indicates that there are three distinct types of bonding within the Au_{19} particle which can be understood to correspond with Edge, Facet, and Internal bonds. This characterisation of the differing bonding environments was also found to be consistent with the number of environments predicted by determining the coordination of the atoms at either end of a specific bond.

The method introduced for analysing and predicting stress using a bond aligned elastic tensor proved to be able to converge the values of the tensor to a high accuracy and produce predicted forces that were consistent with the experimental data. This machine-learning derived methodology utilised a neural network for the purposes of error-gradient descent in an approach that has broad applicability, reducing the complexity of analysing other concerted properties based upon density functional theory calculations. The only necessary changes being alteration of the custom loss function to suit the property in question and a sufficient set of training data.

As a further study upon the concerted properties within molecular and nanoparticle systems, a tool for symmetry analysis was developed and found to be consistent with group theory, namely the Irregular Particle Symmetry Analysis software, IPSA. This was built upon a novel method of symmetry analysis that, unlike current alternative measures, is capable of characterising large systems and providing significant insight into the continuous symmetry within these systems. As part of this, four measures of symmetry were introduced:

- Continuous Symmetry Measurement (CSM_l^n),
- Single Atom Symmetry (SAS_l),
- Symmetry-Orientation Space Cross-sections ($SOCS$),
- Soft Tolerance Point Group Assignment ($STоPA_l^n$).

As a part of the $SOCS$ measure, a vector representation of symmetry was also formulated that allows for continuous symmetry measures and group theory to be described under a coherent analysis framework.

The applications of these techniques, both symmetry analysis and machine learning assisted tensor approximation, are not limited solely to chemistry and it is expected that these may prove useful in other fields such as biology, physics, and mathematics. These tools can be used as extensions to existing automated analysis methodologies or as unique characterisation and analysis tools in their own right. As such, whilst this thesis uses small nanoparticles as a vehicle for the analysis and interpretation, it is the hope of the author that these methodologies can be added to existing processes and provide utility beyond the scope of this particular study.

6.1 Future work

The directions of future work for these projects that are currently being explored are the application of the elastic tensor calculation to other systems, as well as using the machine-learning methodology for predicting other tensor properties. Other potential applications of the IPSA measurements are also being examined, particularly with the purpose of looking for patterns of symmetry favourability in nanocrystallite geometries which can then be utilised to assist with crystal structure prediction. Expansion of the methodology to include analysis of symmetries relevant to space-groups by inclusion of translational symmetry is also being explored. If achieved, this would allow the methodology to better examine local protein-folding and the symmetries of periodic materials. As well as this, development of the processes to allow for examination of the symmetry of volumetric data is being considered.

Another direction for future work that expands upon this thesis would be in the characterisation of the reaction mechanism for the Pd(II) precursor reduction to form the Pd(0) seeds that grow into nanoparticles. This would provide a great deal of insight into the behaviour of capping agents during the formation of palladium nanoparticles and is a natural continuation from the work presented in this study. Further characterisation of the bonding in small nanoparticle species is also suggested, as this can provide significant insight into developing processes for stabilisation of catalytically active species that are currently only formed as minority products during synthesis.

References

(1) C. M. Aikens, *Molecular Simulation*, 2012, **38**, 607–614.

(2) W. A. de Heer, *Reviews of Modern Physics*, 1993, **65**, 611–676.

(3) A. Desireddy, B. E. Conn, J. Guo, B. Yoon, R. N. Barnett, B. M. Monahan, K. Kirschbaum, W. P. Griffith, R. L. Whetten, U. Landman and T. P. Bigioni, *Nature*, 2013, **501**, 399–402.

(4) E. Roduner, *Nanoscopic materials: size-dependent phenomena*, in collab. with R. S. of Chemistry (Great Britain), OCLC: ocm71346503, RSC Pub, Cambridge, 2006, 285 pp.

(5) H. Nishioka, K. Hansen and B. R. Mottelson, *Physical Review B*, 1990, **42**, 9377–9386.

(6) C. P. Joshi, M. S. Bootharaju, M. J. Alhilaly and O. M. Bakr, *Journal of the American Chemical Society*, 2015, **137**, 11578–11581.

(7) A. Sanchez, S. Abbet, U. Heiz, W.-D. Schneider, H. Häkkinen, R. N. Barnett and U. Landman, *The Journal of Physical Chemistry A*, 1999, **103**, 9573–9578.

(8) *Nanocatalysis*, ed. U. Heiz and U. Landman, Springer, Berlin ; New York, 2007, 503 pp.

(9) J. R. Reimers, Y. Wang, B. O. Cankurtaran and M. J. Ford, *Journal of the American Chemical Society*, 2010, **132**, 8378–8384.

(10) W. W. Xu, Y. Li, Y. Gao and X. C. Zeng, *Nanoscale*, 2016, **8**, 1299–1304.

(11) X.-B. Li, H.-Y. Wang, X.-D. Yang, Z.-H. Zhu and Y.-J. Tang, *The Journal of Chemical Physics*, 2007, **126**, 084505.

(12) N. R. Jana and T. Pal, *Langmuir*, 1999, **15**, 3458–3463.

(13) N. R. Jana, T. K. Sau and T. Pal, *The Journal of Physical Chemistry B*, 1999, **103**, 115–121.

(14) T. K. Sau, A. Pal and T. Pal, *The Journal of Physical Chemistry B*, 2001, **105**, 9266–9272.

(15) L. Guczi, G. Petö, A. Beck, K. Frey, O. Geszti, G. Molnár and C. Daróczi, *Journal of the American Chemical Society*, 2003, **125**, Publisher: American Chemical Society, 4332–4337.

(16) M. Rahaman, A. Dutta and P. Broekmann, *ChemSusChem*, 2017, **10**, _eprint: https://chemistry-europe.onlinelibrary.wiley.com/doi/pdf/10.1002/cssc.201601778, 1733–1741.

(17) S. Ozkar and R. G. Finke, *Langmuir*, 2016, **32**, 3699–3716.

(18) Y. Li, X. M. Hong, D. M. Collard and M. A. El-Sayed, *Organic Letters*, 2000, **2**, 2385–2388.

(19) R. Chinchilla and C. Nájera, *Chemical Reviews*, 2014, **114**, 1783–1826.

(20) J. E. Baeckvall, *Accounts of Chemical Research*, 8.

(21) J. Cookson, *Platinum Metals Review*, 2012, **56**, 83–98.

(22) S. Cheong, J. D. Watt and R. D. Tilley, *Nanoscale*, 2010, **2**, 2045.

(23) B. Karimi, A. Zamani, S. Abedi and J. H. Clark, *Green Chem.*, 2009, **11**, 109–119.

(24) *Metallic nanoparticles*, ed. J. A. Blackman, OCLC: ocn261123173, Elsevier, Amsterdam ; New York, 1st ed, 2009, 385 pp.

(25) P. Pyykkö, *Angewandte Chemie International Edition*, 2004, **43**, 4412–4456.

(26) P. Pyykkö, *Chemical Society Reviews*, 2008, **37**, 1967.

(27) L. A. Cole and J. P. Perdew, *Physical Review A*, 1982, **25**, 1265–1271.

(28) W. Huang, M. Ji, C.-D. Dong, X. Gu, L.-M. Wang, X. G. Gong and L.-S. Wang, *ACS Nano*, 2008, **2**, 897–904.

(29) P. Guo, D. Liu, K. Subramanyam, B. Wang, J. Yang, J. Huang, D. T. Auguste and M. A. Moses, *Nature Communications*, 2018, **9**, 130.

(30) A. C. Anselmo, M. Zhang, S. Kumar, D. R. Vogus, S. Menegatti, M. E. Helgeson and S. Mitragotri, *ACS nano*, 2015, **9**, 3169–3177.

(31) V. M. Huxter, A. Lee, S. S. Lo and G. D. Scholes, *Nano Letters*, 2009, **9**, 405–409.

(32) W. G. Wolfer, *Acta Materialia*, 2011, **59**, 7736–7743.

(33) D. Willock, *Molecular Symmetry*, John Wiley & Sons, 2009, 441 pp.

(34) C. M. Widdifield and R. W. Schurko, *Concepts in Magnetic Resonance, Part A: Bridging Education and Research*, 2009, **34A**, 91–123.

(35) A. T. Balaban, *Computers & Mathematics with Applications*, 1986, **12**, 999–1020.

(36) A. J. Coleman, *Reviews of Modern Physics*, 1963, **35**, 668–686.

(37) L. P. Bouckaert, R. Smoluchowski and E. Wigner, *Physical Review*, 1936, **50**, Publisher: American Physical Society, 58–67.

(38) W. B. Jensen, in *Symmetry*, ed. I. Hargittai, Pergamon, 1986, pp. 487–510.

(39) H. Zabrodsky, S. Peleg and D. Avnir, *IEEE Transactions on Pattern Analysis and Machine Intelligence*, 1995, **17**, Conference Name: IEEE Transactions on Pattern Analysis and Machine Intelligence, 1154–1166.

(40) P. Alemany, D. Casanova and S. Álvarez, *Physical Chemistry Chemical Physics*, 2012, **14**, 11816.

(41) M. Pinsky, D. Casanova, P. Alemany, S. Alvarez, D. Avnir, C. Dryzun, Z. Kizner and A. Sterkin, *Journal of Computational Chemistry*, 2008, **29**, 190–197.

(42) P. Hohenberg and W. Kohn, *Physical Review*, 1964, **136**, B864–B871.

(43) W. Koch and M. C. Holthausen, *A chemist's guide to density functional theory*, OCLC: 553727271, Wiley-VCH, Weinheim, 2nd ed., 5. reprint, 2008, 300 pp.

(44) R. M. Dreizler and E. K. Gross, *Density functional theory: an approach to the quantum many body problem*, OCLC: 256760395, Springer, Berlin, 1995, 302 pp.

(45) W. Kohn and L. J. Sham, *Physical Review*, 1965, **140**, A1133–A1138.

(46) J. P. Perdew, K. Burke and M. Ernzerhof, *Phys. Rev. Lett.*, 1996, **77**, 3865–3868.

(47) J. P. Perdew and K. Schmidt, *AIP Conference Proceedings*, 2001, **577**, Publisher: American Institute of Physics, 1–20.

(48) N. E. Schultz, Y. Zhao and D. G. Truhlar, *The Journal of Physical Chemistry A*, 2005, **109**, 4388–4403.

(49) J. N. Harvey, *Annual Reports Section 'C' (Physical Chemistry)*, 2006, **102**, 203–226.

(50) M. Bühl, C. Reimann, D. A. Pantazis, T. Bredow and F. Neese, *Journal of Chemical Theory and Computation*, 2008, **4**, 1449–1459.

(51) F. Neese, *Wiley Interdisciplinary Reviews: Computational Molecular Science*, 2012, **2**, 73–78.

(52) G. Kresse and J. Hafner, *Physical Review B*, 1993, **47**, 558–561.

(53) G. Kresse and J. Furthmüller, *Physical Review B*, 1996, **54**, 11169–11186.

(54) G. Kresse and J. Hafner, *Physical Review B*, 1994, **49**, 14251–14269.

(55) G. Kresse and J. Furthmüller, *Computational Materials Science*, 1996, **6**, 15–50.

(56) P. A. M. Dirac, *Proceedings of the Royal Society of London. Series A, Containing Papers of a Mathematical and Physical Character*, 1928, **117**, 610–624.

(57) J. .-L. Heully, I. Lindgren, E. Lindroth, S. Lundqvist and A. .-M. Martensson-Pendrill, *Journal of Physics B: Atomic and Molecular Physics*, 1986, **19**, 2799–2815.

(58) E. v. Lenthe, E. J. Baerends and J. G. Snijders, *The Journal of Chemical Physics*, 1993, **99**, 4597–4610.

(59) R. van Leeuwen, E. van Lenthe, E. J. Baerends and J. G. Snijders, *The Journal of Chemical Physics*, 1994, **101**, 1272–1281.

(60) T. Nakajima and K. Hirao, *Chemical Reviews*, 2012, **112**, 385–402.

(61) D. A. Pantazis, X.-Y. Chen, C. R. Landis and F. Neese, *Journal of Chemical Theory and Computation*, 2008, **4**, 908–919.

(62) F. Weigend and R. Ahlrichs, *Phys. Chem. Chem. Phys.*, 2005, **7**, 3297–3305.

(63) C. Ullrich, *Time-dependent density-functional theory: concepts and applications*, OCLC: ocn751833811, Oxford University Press, Oxford ; New York, 2012, 526 pp.

(64) R. F. W. Bader, *Accounts of Chemical Research*, 1985, **18**, 7.

(65) R. F. W. Bader and T. T. Nguyen-Dang, in *Advances in Quantum Chemistry*, ed. P.-O. Löwdin, Academic Press, 1981, vol. 14, pp. 63–124.

(66) P. S. V. Kumar, V. Raghavendra and V. Subramanian, *Journal of Chemical Sciences*, 2016, **128**, 1527–1536.

(67) S. Grimme, J. Antony, S. Ehrlich and H. Krieg, *The Journal of Chemical Physics*, 2010, **132**, 154104.

(68) S. Grimme, S. Ehrlich and L. Goerigk, *Journal of Computational Chemistry*, 2011, **32**, 1456–1465.

(69) E. Caldeweyher, C. Bannwarth and S. Grimme, *The Journal of Chemical Physics*, 2017, **147**, 034112.

(70) T. Lu and F. Chen, *Journal of Computational Chemistry*, 2012, **33**, 580–592.

(71) D. M. Wood and A. Zunger, *Journal of Physics A: Mathematical and General*, 1985, **18**, 1343–1359.

(72) P. Pulay, *Chemical Physics Letters*, 1980, **73**, 393–398.

(73) S. Campisi, C. Beevers, A. Nasrallah, C. R. A. Catlow, C. E. Chan-Thaw, M. Manzoli, N. Dimitratos, D. J. Willock, A. Roldan and A. Villa, *J. Phys. Chem. C*, 2020, DOI: 10.1021/acs.jpcc.9b09791.

(74) F. Weigend, *Phys. Chem. Chem. Phys.*, 2006, **8**, 1057.

(75) C. Lee, W. Yang and R. G. Parr, *Phys. Rev. B*, 1988, **37**, 785–789.

(76) P. J. Stephens, F. J. Devlin, C. F. Chabalowski and M. J. Frisch, *J. Phys. Chem.*, 1994, **98**, 11623–11627.

(77) A. D. Becke, *The Journal of Chemical Physics*, 1993, **98**, 5648–5652.

(78) S. H. Vosko, L. Wilk and M. Nusair, *Can. J. Phys.*, 1980, **58**, 1200–1211.

(79) A. D. Becke, *The Journal of Chemical Physics*, 1993, **98**, 1372–1377.

(80) A. D. Becke, *Phys. Rev. A*, 1988, **38**, 3098–3100.

(81) M. P. Waller, H. Braun, N. Hojdis and M. Bühl, *Journal of Chemical Theory and Computation*, 2007, **3**, 2234–2242.

(82) S. Grimme, *Journal of Computational Chemistry*, **27**, 1787–1799.

(83) E. F. Valeev, *Libint: A Library for the Evaluation of Molecular Integrals of Many-Body Operators over Gaussian Functions*, 2018.

(84) S. Grimme, *The Journal of Chemical Physics*, 2013, **138**, 244104.

(85) F.-W. C. Tian Lu, *Acta Chimica Sinica*, 2011, **69**, 2393.

(86) P. Vidossich and A. Lledós, *Dalton Transactions*, 2014, **43**, 11145–11151.

(87) J. Pipek and P. G. Mezey, *The Journal of Chemical Physics*, 1989, **90**, 4916–4926.

(88) P. H.-L. Sit, F. Zipoli, J. Chen, R. Car, M. H. Cohen and A. Selloni, *Chemistry - A European Journal*, 2011, **17**, 12136–12143.

(89) H. J. Monkhorst and J. D. Pack, *Physical Review B*, 1976, **13**, 5188–5192.

(90) F. Klasovsky, P. Claus and D. Wolf, *Topics in Catalysis*, 2009, **52**, 412–423.

(91) H.-F. Wang, W. E. Kaden, R. Dowler, M. Sterrer and H.-J. Freund, *Physical Chemistry Chemical Physics*, 2012, **14**, 11525.

(92) L. Elding, *Inorganica Chimica Acta*, 1972, **6**, 683–688.

(93) M. J. Grogan and K. Nakamoto, *Journal of the American Chemical Society*, 1966, **88**, 5454–5460.

(94) J.-F. Boily, T. M. Seward and J. M. Charnock, *Geochimica et Cosmochimica Acta*, 2007, **71**, 4834–4845.

(95) E. Groppo, G. Agostini, E. Borfecchia, L. Wei, F. Giannici, G. Portale, A. Longo and C. Lamberti, *The Journal of Physical Chemistry C*, 2014, **118**, 8406–8415.

(96) R. E. Newnham, *Properties of materials: anisotropy, symmetry, structure*, OCLC: ocm56639853, Oxford University Press, Oxford ; New York, 2005, 378 pp.

(97) A. R. West, *Solid state chemistry and its applications*, Wiley, Chichester [West Sussex] ; New York, 1984, 734 pp.

(98) S. Patala, L. D. Marks and M. Olvera de la Cruz, *The Journal of Physical Chemistry C*, 2013, **117**, 1485–1494.

(99) Y. Hui, X. Yi, D. Wibowo, G. Yang, A. P. J. Middelberg, H. Gao and C.-X. Zhao, *Science Advances*, 2020, **6**, eaaz4316.

(100) D. N. Theodorou and U. W. Suter, *Macromolecules*, 1986, **19**, 139–154.

(101) G. M. Odegard, T. C. Clancy and T. S. Gates, *Polymer*, 2005, **46**, 553–562.

(102) M. Parrinello and A. Rahman, *The Journal of Chemical Physics*, 1998, **76**, Publisher: American Institute of PhysicsAIP, 2662.

(103) A. A. Gusev, M. M. Zehnder and U. W. Suter, *Physical Review B*, 1996, **54**, Publisher: American Physical Society, 1–4.

(104) S. Grigoras, A. A. Gusev, S. Santos and U. W. Suter, *Polymer*, 2002, **43**, 489–494.

(105) M. Meyers, J. Rickman and T. Delph, *Journal of Applied Physics*, 2005, **98**, 066106–066106.

(106) E. Voyiatzis, *Computer Physics Communications*, 2013, **184**, 27–33.

(107) R. Maranganti and P. Sharma, *Physical Review Letters*, 2007, **98**, Publisher: American Physical Society, 195504.

(108) Z. Cui, S. Yang and L. C. Brinson, *Physical Review B*, 2015, **91**, Publisher: American Physical Society, 184104.

(109) E. Riccardi, M. C. Böhm and F. Müller-Plathe, *Physical Review E*, 2012, **86**, Publisher: American Physical Society, 036704.

(110) T. Delph, *Proceedings of the Royal Society A: Mathematical, Physical and Engineering Sciences*, 2005, **461**, Publisher: Royal Society, 1869–1888.

(111) M. Marsman, J. Paier, A. Stroppa and G. Kresse, *Journal of Physics: Condensed Matter*, 2008, **20**, Publisher: IOP Publishing, 064201.

(112) P. Politzer, J. S. Murray and F. A. Bulat, *Journal of Molecular Modeling*, 2010, **16**, 1731–1742.

(113) J. H. Stenlid and T. Brinck, *Journal of the American Chemical Society*, 2017, **139**, 11012–11015.

(114) S. Jenkins, P. Ayers, S. Kirk, P. Mori-Sánchez and A. Martín Pendás, *Chemical Physics Letters*, 2009, **471**, 174–177.

(115) P. W. Ayers and S. Jenkins, *Computational and Theoretical Chemistry*, 2015, **1053**, 112–122.

(116) H. L. Schmider and A. D. Becke, *The Journal of Chemical Physics*, 2002, **116**, 3184–3193.

(117) H. Jacobsen, *Chemical Physics Letters*, 2013, **582**, 144–147.

(118) E. R. Johnson, S. Keinan, P. Mori-Sánchez, J. Contreras-García, A. J. Cohen and W. Yang, *Journal of the American Chemical Society*, 2010, **132**, 6498–6506.

(119) N. Joel and W. A. Wooster, *Nature*, 1957, **180**, 430–431.

(120) H. Zabrodsky, S. Peleg and D. Avnir, *Journal of the American Chemical Society*, 1992, **114**, 7843–7851.

(121) M. G. Katz and D. M. Sherry, *Notices of the American Mathematical Society*, 2012, **59**, 1550.

(122) C. Dryzun, A. Zait and D. Avnir, *Journal of Computational Chemistry*, 2011, **32**, _eprint: https://onlinelibrary.wiley.com/doi/pdf/10.1002/jcc.21828, 2526–2538.

(123) R. J. Largent, W. F. Polik and J. R. Schmidt, *Journal of Computational Chemistry*, 2012, **33**, 1637–1642.

(124) M. Pinsky and D. Avnir, *Inorganic Chemistry*, 1998, **37**, 5575–5582.

(125) H. Zabrodsky, S. Peleg and D. Avnir, Computer Vision and Pattern Recognition, 1992. Proceedings CVPR'92., 1992 IEEE Computer Society Conference on, IEEE, 1992, pp. 703–706.

(126) N. D. Matsakis and F. S. Klock II, ACM SIGAda Ada Letters, 2014, vol. 34, pp. 103–104.

(127) G. Van Rossum and F. L. Drake, *Python 3 Reference Manual*, Scotts Valley, CA, 2009.

(128) B. D. Sharma, *Journal of Chemical Education*, 1982, **59**, 554.

(129) F. Crameri, G. E. Shephard and P. J. Heron, *Nature Communications*, 2020, **11**, 5444.

(130) B. O. Community, *Blender - a 3D modelling and rendering package*, Blender Foundation, Stichting Blender Foundation, Amsterdam, 2018.

(131) W. Voigt, *Lehrbuch der Kristallphysik: mit Ausschluß der Kristalloptik*, OCLC: 913701611, 1966.

Appendix A

Appendices

A.1 Symmetry measure derivation

Let there be two points, P and Q, defined by equation A.1.

$$P = \begin{pmatrix} p_x \\ p_y \\ p_z \end{pmatrix} Q = \begin{pmatrix} q_x \\ q_y \\ q_z \end{pmatrix} \tag{A.1}$$

The symmetry transformed image of P, T, is defined by equation A.2

$$T = MP \tag{A.2}$$

Where M is a symmetry transform about the z-axis.

A measure of symmetry, $f(\theta, O, p_x, q_x, p_y, q_y, p_z, q_z)$, between those points can be defined as a function of the distance, d, between the image of P, T, and Q, defined by equation A.3.

$$f(\theta, O, p_x, q_x, p_y, q_y, p_z, q_z) = \frac{1}{1 + d(\theta, O, p_x, q_x, p_y, q_y, p_z, q_z)} \tag{A.3}$$

Where d is given by equation A.4.

$$d(\theta, O, p_x, q_x, p_y, q_y, p_z, q_z) = \sqrt{C_z(\theta, O, p_z, q_z) + C_{xy}(\theta, O, p_x, q_x, p_y, q_y)} \tag{A.4}$$

With $C_z(\theta, O, p_z, q_z)$ being the component of distance aligned with the axis of sym-

metry, the distance q_z to t_z, and $C_{xy}(\theta, O, p_x, q_x, p_y, q_y)$ being the component in the plane orthogonal to the axis of symmetry, the distance Q_{xy} to T_{xy}.

$$C_z = (t_z - q_z)^2 \tag{A.5}$$

With C_z, as the symmetry operation is defined as being about the z-axis, the term for transformation of the p_z to t_z must be restricted to a binary of either -1 or 1.

For proper rotations the t_z term must be equal to p_z. For reflections t_z must be equal to $-p_z$, and, generalising this to improper rotations, the transformation of p_z to give t_z must be a periodic step function, with the period determined by the order of the rotation. This allows for t_z to be expressed in terms of p_z and a coefficient that depends upon the periodicity of the symmetry operation, O, and the angle, θ, between Q and P, which gives the sign-determining coefficient $\epsilon(O, \theta)$.

$$C_z = (\epsilon(O, \theta)p_z - q_z)^2 = (p_z + \epsilon(O, \theta)q_z)^2 \tag{A.6}$$

Where $\epsilon(O, \theta)$ is a sign determining coefficient that varies based upon the operation, as shown in equation A.7.

$$\epsilon(O, \theta) = \begin{cases} -1 & \text{Proper rotation} \\ 1 & \text{Reflection} \\ \begin{cases} 1 & \epsilon_z(O, \theta) \geq 0 \\ -1 & \epsilon_z(O, \theta) \leq 0 \end{cases} & \text{Inversion, Improper rotation} \end{cases} \tag{A.7}$$

$$\text{Where: } \epsilon_z(O, \theta) = \frac{2}{\pi} \arccos\left(cos\left(\frac{1}{2} O \arccos\left(cos\left(\frac{2\pi}{O}\right)\right) \lfloor \frac{O\theta}{2\pi} + 0.5 \rfloor\right)\right) - 1 \tag{A.8}$$

The form of $\epsilon_z(O, \theta)$ is constructed to give a periodic step function, the values of this function for $O = 4$ are shown plotted in figure A.1.

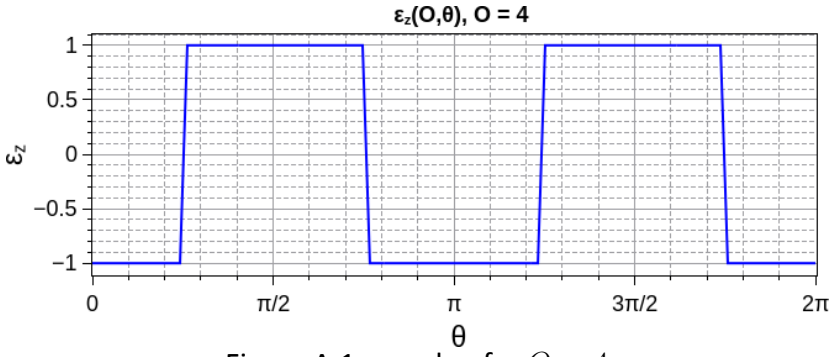

Figure A.1: ϵ_z value for $O = 4$

The distance from Q_{xy} to T_{xy}, equation A.9, can be expressed in terms of the cosine rule, as is shown in equation A.10, where γ is the angle between Q_{xy} and T_{xy}.

$$C_{xy} = (t_x - q_x)^2 + (t_y - q_y)^2 \tag{A.9}$$

$$C_{xy} = t_x^2 + t_y^2 + q_x^2 + q_y^2 - 2\sqrt{t_x^2 + t_y^2}\sqrt{q_x^2 + q_y^2}cos(\gamma) \tag{A.10}$$

Where γ is the angle between T_{xy} and Q_{xy}.

Similarly to the treatment of C_z, the terms of T_{xy} are expanded in terms of P_{xy}, such that t_x and t_y are expressed as functions of p_x and p_y.

$$t_x = p_x cos(c) - p_y sin(c) \tag{A.11}$$

$$t_y = p_x sin(c) + p_y cos(c) \tag{A.12}$$

Where c is the angle between P_{xy} and the image T_{xy} which is closest to Q_{xy}, an integer multiple of $\frac{2\pi}{O}$, shown in equation A.13.

$$c = m\frac{2\pi}{O} \tag{A.13}$$

The value of c that gives the image T_{xy} closest to Q_{xy} is determined by the domain of a periodic step function and, due to this, c can be expressed in terms of a floor function of the angle between Q_{xy} and P_{xy}.

$$c = \frac{2\pi}{O}\lfloor\frac{O\theta}{2\pi} + 0.5\rfloor \tag{A.14}$$

By utilising the known periodicity of the symmetry operation to determine the image, T_{xy}, closest to the point Q_{xy}, the angle γ, shown in equations A.11 and A.12, between T_{xy} and Q_{xy} can be expressed in terms of the c and θ angles, equation A.15.

$$\gamma = \theta - \frac{2\pi}{O}\lfloor\frac{O\theta}{2\pi} + 0.5\rfloor \tag{A.15}$$

As θ can itself be expressed in terms of P_{xy} and Q_{xy}, shown in equation A.16, γ can, therefore, be expressed in terms of P_{xy}, θ, and O.

$$\theta = \arccos\left(\frac{(p_x q_x) + (p_y q_y)}{\sqrt{p_x^2 + p_y^2}\sqrt{q_x^2 + q_y^2}}\right) \tag{A.16}$$

$$\gamma = \arccos\left(\frac{(p_x q_x) + (p_y q_y)}{\sqrt{p_x^2 + p_y^2}\sqrt{q_x^2 + q_y^2}}\right) - \frac{2\pi}{O}\lfloor\frac{O\theta}{2\pi} + 0.5\rfloor \tag{A.17}$$

Substitution of equations A.11, A.12, A.17, A.14, and A.16 into equation A.10, followed by simplification through application of the trigonometric identities, gives equation A.18. Floor functions were left in terms of theta to assist with computation.

$$C_{xy}(\theta, O, p_x, q_x, p_y, q_y) = \begin{pmatrix} -2\sqrt{a^2 + b^2} \times \sqrt{2(a^2 + b^2) - 2d\cos(c)} \\ \cos\left(\arccos\left(\dfrac{p_y a + p_x b}{\sqrt{d}\sqrt{a^2 + b^2}}\right) - \dfrac{\pi - c}{2}\right) \\ -2d\cos(c) + a^2 + 2d + b^2 \end{pmatrix} \tag{A.18}$$

Where: $a = (p_y - q_y)^2$, $b = (p_x - q_x)^2$, $c = \dfrac{2\pi}{O}\lfloor\dfrac{O\theta}{2\pi} + 0.5\rfloor$, $d = (p_x^2 + p_y^2)$

A.2 Elasticity tensor calculation script

```
import os
import math
import numpy as np
from numpy import cross, eye, dot
from scipy.linalg import expm, norm
import tensorflow as tf
from numpy import loadtxt
from tensorflow import keras
from keras.models import Sequential, save_model, load_model
from keras.layers import Dense, Dropout, Activation,
LeakyReLU, Lambda
from numpy import genfromtxt
from ase import io
from ase import neighborlist
from ase.geometry.analysis import Analysis

import kerastuner as kt

import matplotlib.pyplot as plt

#from ase.visualize import view

########################----Notes----#########################
#                                                            #
# Script is divided into geometry and strain determination   #
# and a neural network that then predicts the elasticity     #
# tensors based upon the forces upon a molecule and the      #
# strain vectors found by the first section. The parameters  #
# the strain space can be altered to allow for non-xyz       #
# components of the distortions that contribute to the       #
# forces.                                                    #
#                                                            #
##############################################################

################----Input information----####################

FORCE_DIMENSION = 3
SPACE_DIMENSION = 3


###################----Parameters----#########################
# Parameters for the neural network

# Leaky Relu alpha term (Gradient below zero)
alpha = 0.9

# Proportion of nodes dropped in the dropout layer
dropout = 0.1

#Set learning rates for the fitting steps
initial_learning_rate = 0.001
second_learning_rate = 0.0001
tertiary_learning_rate = 0.00001

```

```
53              #Define exponentially decreasing learning rate (Not used at
    the moment)
54              lr_schedule = tf.keras.optimizers.schedules.ExponentialDecay(
55              second_learning_rate,
56              decay_steps=10000,
57              decay_rate=0.96,
58              staircase=False)
59
60              # Set epochs and batch sizes
61              epochs_1 = 40000
62              batch_size_1 = 6
63
64              epochs_2 = 200000
65              batch_size_2 = 2
66
67              epochs_3 = 500000
68              batch_size_3 = 3
69
70              ###################----Structure
    Coord----####################
71              # Define the Cartesian axes for each structure
72              X_AXIS = np.array([1, 0, 0])
73              Y_AXIS = np.array([0, 1, 0])
74              Z_AXIS = np.array([0, 0, 1])
75
76              #Set this value to the number of linearly independant
    strain/force directions.
77              # VERY IMPORTANT!
78
79              STRUCTURE_FORCE_VECS = []
80              STRUCTURE_ROTATION_MATRICES = []
81              STRUCTURE_STRAIN_VECS = []
82
83              struct_count = 0
84
85              MAX_NON_ZERO_V_COUNT = 0
86              NUM_COORD_ENV = 0
87
88              # Set the local directory as the place to look for subdirs
89              subdirs = next(os.walk('.'))[1]
90
91              print(subdirs)
92
93              #Iterate over the subdirectories of "."
94              for DIR in subdirs:
95              ##### Load the structures ####
96              print("Loading geometries from {} directory.".format(dir))
97              #Path to the starting geometry
98              INITIAL_GEOM_PATH = "./"+DIR+"/Original/CONTCAR"
99              #Path to the strained geometry
100             STRAINED_GEOM_PATH = "./"+DIR+"/Distorted/CONTCAR"
101
102             # Script expects the forces as a csv in the subdirectory of
    "."
103             # This could potentially be automater to read from a contcar
104             FORCE_PATH = "./"+DIR+"/forces.csv"
105             Force_xyz = genfromtxt(FORCE_PATH, delimiter=',')
```

```
106
107                 #Load the geometries
108                 STRUCTURE = io.read(INITIAL_GEOM_PATH)
109                 STRAINED_STRUCTURE = io.read(STRAINED_GEOM_PATH)
110
111                 #View it to check it is sensible
112                 #view(STRUCTURE)
113                 #view(STRAINED_STRUCTURE)
114                 ################################
115
116                 #### Process Neighbours and bonding ####
117                 #Get coordination numbers for atoms using natural cutoffs
118                 i = neighborlist.neighbor_list('i', STRUCTURE, 3)
119                 COORDINATION = np.bincount(i)
120                 # print(COORDINATION)
121
122                 print("Analysing the unstrained structure:")
123
124                 #Print coordination numbers of all atoms in order of CONTCAR
125                 print("Number of coordination environments:
    {}".format(len(set(COORDINATION))))
126                 # Store the number of coordination environments
127                 NUM_COORD_ENV = len(set(COORDINATION))
128
129                 #Run analysis on the structure to get bonding information
130                 UNSTRAINED_ANALYTICS = Analysis(STRUCTURE)
131                 STRAINED_ANALYTICS = Analysis(STRAINED_STRUCTURE)
132
133                 #Get unique Au-Au bonds
134                 AU_AU_BONDS = UNSTRAINED_ANALYTICS.get_bonds('Au', 'Au',
    unique=True)
135
136                 print("There are {} Au-Au bonds in
    structure.".format(len(AU_AU_BONDS[0])))
137
138                 #Get bond lengths
139                 AU_AU_BOND_LENGTHS =
    UNSTRAINED_ANALYTICS.get_values(AU_AU_BONDS)
140
141
142                 # Prepare some empty arrays
143                 COORD_ENVIROMENTS = []
144                 COORD_ENV_VALUES = []
145                 BOND_VECTORS = []
146                 ROTATION_MATRICES = []
147                 ENV_ORDER = []
148
149                 #Characterise bonds by coordination to produce 4d vector
150                 # The coordination environment is determined here to allow
    for quick lookup in the next loop.
151                 # print(AU_AU_BONDS[0])
152                 #Iterate over the various bonds
153                 for bi in AU_AU_BONDS[0]:
154                 #Get indices of atoms involved in bond
155                 p0index = bi[0]
156                 p1index = bi[1]
157                 #Get coordination of atoms
```

```
158                 BOND_COORD_ENV = [COORDINATION[p0index],
    COORDINATION[p1index]]
159                 #Store the pair of coordination values
160                 COORD_ENVIROMENTS.append(BOND_COORD_ENV)
161
162                 #Determine which atom is of lower coordination
163                 if COORDINATION[p0index] < COORDINATION[p1index]:
164                 envcoef = 1
165                 else:
166                 envcoef = -1
167
168                 #Store this information
169                 ENV_ORDER.append(envcoef)
170
171                 #calculate a coordination value that characterises bond and
    store it
172                 coval = COORDINATION[p0index]*COORDINATION[p1index]
173                 COORD_ENV_VALUES.append(coval)
174
175                 #append bond coordination value to cartesian vector
176                 print("Coordination environments")
177                 print(COORD_ENVIROMENTS)
178                 print("Coordination values")
179                 print(COORD_ENV_VALUES)
180
181                 BOND_INDEX = 0
182
183                 # Repeat the loop again
184                 for bi in AU_AU_BONDS[0]:
185                 #Get indices of atoms involved in bond
186                 p0index = bi[0]
187                 p1index = bi[1]
188
189                 # get cart. coords. of atom
190                 p0 = STRUCTURE[p0index].position
191                 p1 = STRUCTURE[p1index].position
192
193                 #Determine vector between atom p0 and atom p1
194                 #(Direction depends upon the coordination enivronment)
195                 envcoef = ENV_ORDER[BOND_INDEX]
196                 bondvec = np.array(envcoef * p1 -envcoef * p0)
197
198                 if envcoef == 1:
199                 origin = 0
200                 else:
201                 origin = 1
202
203                 #Calculate the length of the bond vector
204                 bondlength = np.linalg.norm(bondvec)
205
206                 #Normalise bond length
207                 normalised_bond = bondvec / bondlength
208
209                 #Find axis for z alignment rotation
210                 rotation_axis = np.cross(Z_AXIS, normalised_bond)
211
212                 #Normalise the axis
```

```
213                 rotation_axis = rotation_axis/ np.linalg.norm(rotation_axis)
214
215                 #calculate dot product between z axis and bond
216                 dotproduct = np.dot(Z_AXIS, normalised_bond)
217
218                 #Calculate the cosine of the angle
219                 costheta = dotproduct / (np.linalg.norm(normalised_bond) *
    np.linalg.norm(Z_AXIS))
220
221                 #Calculate angle between bond and z axis
222                 theta = math.acos(costheta)
223
224                 # Define a function to calculate the rotation matrix
225                 def M(axis, theta):
226                 return expm(cross(eye(3), axis/norm(axis)*theta))
227
228                 z_rotation_matrix = M(rotation_axis, theta)
229
230                 #Generate x,y alignment rotation matrix
231                 # This is essentially a 2d problem so the last column and
    row are zero except for b33
232                 #Need to find the lowest coordinate bond (Apart from current
    bond)
233                 # print("Origin atom bonds")
234
235                 xynewbond = np.array([0,0,0])
236                 # xyalignbondindex = BOND_INDEX
237                 for bond_index in range(len(AU_AU_BONDS[0])):
238                 if AU_AU_BONDS[0][bond_index][0] == bi[origin] or \
239                 AU_AU_BONDS[0][bond_index][1] == bi[origin]:
240                 # print(bond_index, ": ", AU_AU_BONDS[0][bond_index], "
    Coord env: ",
241                 #COORD_ENVIROMENTS[bond_index], "   Coord value: ",
    COORD_ENV_VALUES[bond_index])
242                 if bond_index != BOND_INDEX:
243                 if AU_AU_BONDS[0][bond_index][0] == bi[origin]:
244                 newbondvec =
    np.array(STRUCTURE[AU_AU_BONDS[0][bond_index][1]]
245                 .position - STRUCTURE[AU_AU_BONDS[0][bond_index][0]]
246                 .position)
247                 else:
248                 newbondvec =
    np.array(STRUCTURE[AU_AU_BONDS[0][bond_index][0]]
249                 .position - STRUCTURE[AU_AU_BONDS[0][bond_index][1]]
250                 .position)
251                 xynewbond = np.add(newbondvec, xynewbond)
252
253                 print("New bond vector: ", xynewbond)
254
255                 xynewbond = np.dot(z_rotation_matrix, xynewbond)
256                 #This problem can be reduced to two dimensions with z axis
    being the known rotation axis
257                 twodvec = np.array([xynewbond[0], xynewbond[1]])
258                 if np.linalg.norm(twodvec) >= 0.05:
259                 print(twodvec)
260                 two_x = np.array([1, 0])
261                 dotproduct = np.dot(two_x, twodvec)
```

```
262
263                 #Calculate the cosine of the angle
264                 costheta = dotproduct / (np.linalg.norm(twodvec) *
    np.linalg.norm(two_x))
265                 #Calculate angle between bond and xz-plane
266                 theta = math.acos(costheta)
267
268                 xy_rotation_matrix = M(Z_AXIS, theta)
269                 #Combine the matrices
270                 # rotation_matrix = xy_rotation_matrix @ z_rotation_matrix
271                 rotation_matrix = np.dot(xy_rotation_matrix,
    z_rotation_matrix)
272
273                 else:
274                 rotation_matrix = z_rotation_matrix
275
276                 #Store the rotation matrices in order to recall later
277                 ROTATION_MATRICES.append(rotation_matrix)
278
279                 # print(rotation_matrix)
280                 # Determine the z-alignment rotation matrix for this bond
281
282                 #calculate a coordination value that characterises bond and
    store it
283                 coval = COORD_ENV_VALUES[BOND_INDEX]
284                 # print("Coordination value: ", coval)
285
286                 #append bond coordination value to cartesian vector
287                 bv = np.append(np.dot(rotation_matrix, bondvec), coval)
288                 #print(bv)
289
290                 #store the extended  rotated bond vector
291                 BOND_VECTORS.append(bv)
292                 BOND_INDEX += 1
293
294                 # print(BOND_VECTORS)
295
296                 #Generate n dimensional strain vector and then expand the
    strain space
297                 #to n*number of coordination environments
298                 STRAIN_SPACE_VECTOR = [[0.0]]
299
300                 for n in range(0, SPACE_DIMENSION-1):
301                 STRAIN_SPACE_VECTOR = np.append(STRAIN_SPACE_VECTOR, [0.0])
302
303                 for n in range(0, len(np.unique(COORD_ENV_VALUES))-1):
304                 for m in range(0, SPACE_DIMENSION):
305                 #print("{}, {}".format(n,m))
306                 STRAIN_SPACE_VECTOR = np.append(STRAIN_SPACE_VECTOR, [0.0])
307
308                 #Print empty strain vector
309                 print("Strain vector:\n{}".format(STRAIN_SPACE_VECTOR))
310
311                 STRAIN_SPACE_VECTOR_LENGTH = len(STRAIN_SPACE_VECTOR)
312                 print(STRAIN_SPACE_VECTOR_LENGTH)
313
314                 # #Determine unique coordenation environments
```

```
315                 UNIQUE_COORD_ENV_VAL = np.unique(COORD_ENV_VALUES)
316
317                 print("{} unique bond coordination environments: 
    ".format(len(UNIQUE_COORD_ENV_VAL)))
318                 print(UNIQUE_COORD_ENV_VAL)
319
320                 #Characterise bonds in terms of strain space
321                 STRAIN_SPACE_BOND_VECTORS = []
322
323                 STRAIN_SPACE_BOND_INSTANCE = STRAIN_SPACE_VECTOR
324
325                 OFFSET_LIST = []
326
327                 for bond in BOND_VECTORS:
328                 offset = 0
329                 STRAIN_SPACE_BOND_INSTANCE = 
    np.zeros_like(STRAIN_SPACE_BOND_INSTANCE)
330                 for env in UNIQUE_COORD_ENV_VAL:
331                 if bond[3] == env:
332                 for n in range(0, SPACE_DIMENSION):
333                 STRAIN_SPACE_BOND_INSTANCE[offset+n] = bond[n]
334                 #            print(bond)
335                 #           print(STRAIN_SPACE_BOND_INSTANCE)
336                 #          print("--------")
337
338                 #This would also be the point to add in any other components
    of the strain space like
339                 #xy yz xz that are derived from x, y, z. This would require
    changing the above loop to
340                 #just iterate over x,y,z and then adding functions to
    calculate the combined values and
341                 #position them appropriately relative to the offset
342
343                 STRAIN_SPACE_BOND_VECTORS.append(STRAIN_SPACE_BOND_INSTANCE)
344                 OFFSET_LIST.append(offset)
345                 #Break from the env loop if the bond has been characterised
346                 break
347                 #Iterate the offset
348                 offset = (offset+SPACE_DIMENSION)
349
350
351                 print("Bond strain space offsets:")
352                 print(OFFSET_LIST)
353                 #These offsets, when combined with the bond indices can be
    used to determine the strain space of the
354                 #deformed structure without having to fiddle about with the
    neighbour stuff
355
356                 print("Bonds expressed in {} dimensional strain 
    space.".format(len(STRAIN_SPACE_VECTOR)))
357
358                 # for vector in STRAIN_SPACE_BOND_VECTORS:
359                 # print("{}, {}, {}, {}, {}, {}, {}, {},
    {}".format(vector[0], vector[1], vector[2],
360                 # vector[3], vector[4], vector[5],
361                 # vector[6], vector[7], vector[8]))
362
```

```
363                 print("Finished analysising the unstrained geometry...")
364                 #Analyse the strained geom
365                 print("")
366                 print("Analysing the strained geometry:")
367 
368                 BOND_VECTORS_STRAINED = []
369                 BOND_INDEX = 0
370                 for bi in AU_AU_BONDS[0]:
371                 #print(bi)
372                 #Get indices of atoms involved in bond
373                 p0index = bi[0]
374                 p1index = bi[1]
375                 # get cart. coords. of atom
376                 p0 = STRAINED_STRUCTURE[p0index].position
377                 p1 = STRAINED_STRUCTURE[p1index].position
378                 #print("Bond 1 =
    {},{}".format(AuAuBonds[0][0][0],AuAuBonds[0][0][1]))
379                 #Determine vector between atom p0 and atom p1
380                 envcoef = ENV_ORDER[BOND_INDEX]
381                 bondvec = np.array(envcoef * p1 -envcoef * p0)
382                 #calculate a coordination value that characterises bond and
    store it
383                 coval = COORD_ENV_VALUES[BOND_INDEX]
384                 #append bond coordination value to cartesian vector
385                 bv = np.append(np.dot(ROTATION_MATRICES[BOND_INDEX],
    bondvec), coval)
386                 #store the extended bond vector
387                 BOND_VECTORS_STRAINED.append(bv)
388                 BOND_INDEX += 1
389 
390                 STRAINED_STRAIN_SPACE_BOND_VECTORS = []
391 
392                 #offset: moves the values to next coordination environment
    to expand the vector
393                 for bond in BOND_VECTORS_STRAINED:
394                 offset = 0
395                 STRAIN_SPACE_BOND_INSTANCE =
    np.zeros_like(STRAIN_SPACE_BOND_INSTANCE)
396                 for env in UNIQUE_COORD_ENV_VAL:
397                 if bond[3] == env:
398                 for n in range(0, SPACE_DIMENSION):
399                 STRAIN_SPACE_BOND_INSTANCE[offset+n] = bond[n]
400 
    STRAINED_STRAIN_SPACE_BOND_VECTORS.append(STRAIN_SPACE_BOND_INSTANCE)
401                 #Break from the env loop if the bond has been characterised
402                 break
403                 #Iterate the offset
404                 offset = (offset+SPACE_DIMENSION)
405 
406                 # print("Strained bonds expressed in {} dimensional strain
    space.".format(len(STRAIN_SPACE_VECTOR)))
407                 # for vector in STRAINED_STRAIN_SPACE_BOND_VECTORS:
408                 # print("{}, {}, {}, {}, {}, {}, {}, {},
    {}".format(vector[0], vector[1], vector[2], vector[3], vector[4],
    vector[5], vector[6], vector[7], vector[8]))
409 
410                 # print("")
```

```
411                 #print("Pair of bonds")
412                 # print("Strain vectors")
413                 COUNT_STRAIN_SPACE_VECTORS =
    len(STRAINED_STRAIN_SPACE_BOND_VECTORS)
414                 STRAIN_VECTORS = []
415                 for pair in range(0, COUNT_STRAIN_SPACE_VECTORS):
416                 #print(strain_space_strained_bonds[pair])
417                 #print(strain_space_bonds[pair])
418
    #print(strain_space_strained_bonds[pair]-strain_space_bonds[pair])
419                 temp_sv =
    STRAINED_STRAIN_SPACE_BOND_VECTORS[pair]-STRAIN_SPACE_BOND_VECTORS[pair]
420                 #print("")
421                 STRAIN_VECTORS.append(temp_sv)
422
423                 print("{} Bond coordinate aligned strain vectors
    examined.".format(len(STRAIN_VECTORS)))
424                 strained_bond_index = 0
425
426                 #Create a list of the non-zero vectors
427                 non_zero_vectors = []
428                 nonz_v_rotation_matrices = []
429
430                 for vector in STRAIN_VECTORS:
431                 magnitude = np.linalg.norm(vector)
432                 #    print("{}: ({}, {}, {}, {}, {}, {}, {}, {}, {}) - Atoms
    {}".format(strained_bond_index, vector[0], vector[1], vector[2],
    vector[3], vector[4], vector[5], vector[6], vector[7], vector[8],
    AU_AU_BONDS[0][strained_bond_index]))
433                 if magnitude > 0:
434                 non_zero_vectors.append(vector)
435
    nonz_v_rotation_matrices.append(np.transpose(ROTATION_MATRICES[strained_bond_index]))
436                 # print(ROTATION_MATRICES[strained_bond_index])
437                 strained_bond_index += 1
438
439                 # print("Non zero rotation matrices")
440                 # print(nonz_v_rotation_matrices)
441
442                 strained_bond_index = 0
443                 # print("Nonzero vectors:")
444                 for vector in non_zero_vectors:
445                 # print("{}: ({}, {}, {}, {}, {}, {}, {}, {}, {}) - Atoms
    {}".format(strained_bond_index, vector[0], vector[1], vector[2],
    vector[3], vector[4], vector[5], vector[6], vector[7], vector[8],
    AU_AU_BONDS[0][strained_bond_index]))
446                 #print("Rotation matrix:")
447                 #print(nonz_v_rotation_matrices[strained_bond_index])
448                 strained_bond_index += 1
449
450                 print("Successfully converted structures to strain space!")
451
452                 NON_ZERO_V_COUNT = len(non_zero_vectors)
453                 if NON_ZERO_V_COUNT > MAX_NON_ZERO_V_COUNT:
454                 MAX_NON_ZERO_V_COUNT = NON_ZERO_V_COUNT
455
```

```
456                 print("Found {} non-zero strain
    vectors.".format(NON_ZERO_V_COUNT))
457                 #Convert strain space bonds to 1 by n*dim vector
458                 # split into input (x) and output (y) variables (Which are
    the same really)
459                 #Convert forces into 1d array
460                 Force = np.array(Force_xyz)
461                 Force_dim = len(np.atleast_1d(Force))
462
463                 #Store the forces, rotation matrices, and strain vectors for
    this geometry
464                 STRUCTURE_FORCE_VECS.append(Force)
465                 STRUCTURE_STRAIN_VECS.append(non_zero_vectors)
466                 STRUCTURE_ROTATION_MATRICES.append(nonz_v_rotation_matrices)
467
468                 NUM_STRUCTURES = len(STRUCTURE_STRAIN_VECS)
469
470                 # Equalise lengths with zero vectors and rotation matrices
471
472                 # Equalise the numbers of strain vectors for each structure
473                 # by adding zero vectors to reach the max
474                 STRAIN_VEC_COUNT = 0
475                 for SS_Vec in STRUCTURE_STRAIN_VECS:
476                 length = len(SS_Vec)
477                 if length > STRAIN_VEC_COUNT:
478                 STRAIN_VEC_COUNT = length
479
480                 for SS_Vec in STRUCTURE_STRAIN_VECS:
481                 while len(SS_Vec) < STRAIN_VEC_COUNT:
482                 SS_Vec.append(STRAIN_SPACE_VECTOR)
483
484
485                 print("Rotation matrices vecs shape:")
486
487                 # Equalise the numbers of rotation matrices for each
    structure
488                 # by adding identity matrices to reach the max
489
490                 #Declare identity transformation
491                 UNIT_ROTATION = np.eye(SPACE_DIMENSION)
492
493                 for ROT_MAT in STRUCTURE_ROTATION_MATRICES:
494                 while len(ROT_MAT) < STRAIN_VEC_COUNT:
495                 ROT_MAT.append(UNIT_ROTATION)
496
497                 print("Final shapes:")
498                 print("Force vecs shape:")
499                 STRUCTURE_FORCE_VECS = np.array(STRUCTURE_FORCE_VECS)
500                 print(STRUCTURE_FORCE_VECS.shape)
501
502                 print("Strain space vec shape:")
503                 STRUCTURE_STRAIN_VECS = np.array(STRUCTURE_STRAIN_VECS)
504                 print(STRUCTURE_STRAIN_VECS.shape)
505
506                 print("Rotation matrices shape:")
507                 STRUCTURE_ROTATION_MATRICES =
    np.array(STRUCTURE_ROTATION_MATRICES)
```

```
508                 print(STRUCTURE_ROTATION_MATRICES.shape)
509
510                 ##############----Prepare the data for the
    network----#####################
511
512                 # Convet to tf tensors
513                 SFV_tens = tf.constant(STRUCTURE_FORCE_VECS, dtype="float32")
514                 SSV_tens = tf.constant(STRUCTURE_STRAIN_VECS,
    dtype="float32")
515                 RM_tens = tf.constant(STRUCTURE_ROTATION_MATRICES,
    dtype="float32")
516
517                 #Flatten the tensors
518
519                 flat_SFV_tens = tf.reshape(SFV_tens, [NUM_STRUCTURES, -1])
520                 len_flat_force = len(flat_SFV_tens[0])
521
522                 flat_SSV_tens = tf.reshape(SSV_tens, [NUM_STRUCTURES, -1])
523                 len_flat_strain = len(flat_SSV_tens[0])
524
525                 flat_RM_tens = tf.reshape(RM_tens, [NUM_STRUCTURES, -1])
526                 len_flat_rm = len(flat_RM_tens[0])
527
528                 # print(flat_SFV_tens)
529                 # print(flat_SSV_tens)
530                 # print(flat_RM_tens)
531
532                 # print(len_flat_strain)
533                 # print(len_flat_force)
534                 # print(len_flat_rm)
535
536                 print("Strain length {}; Force length {}; Rotation matrices
    length {}".format(len_flat_strain, len_flat_force, len_flat_rm))
537
538                 # Concatenate tensors
539
540                 SSV_SFV_ten = tf.concat([flat_SSV_tens, flat_SFV_tens], 1)
541                 # print(SSV_SFV_ten)
542                 SSV_SFV_RM_ten = tf.concat([SSV_SFV_ten, flat_RM_tens], 1)
543                 # print(SSV_SFV_RM_ten)
544
545
546                 X = SSV_SFV_ten
547                 print("X shape: {}".format(np.shape(X)))
548
549                 Y = SSV_SFV_RM_ten
550                 print("Y shape: {}".format(np.shape(Y)))
551
552                 print("Prepared {} structures".format(NUM_STRUCTURES))
553
554                 print("Data successfully prepared for tensor calculation")
555
556                 ####################------ANN------#########################
557
558
559
560                 STRAIN_SPACE_INPUT_LENGTH = len_flat_strain + len_flat_force
```

```
561
562             def custom_loss_function(strain_force, tensor):
563             strain = strain_force[0:, 0:len_flat_strain]
564             force = strain_force[0:, len_flat_strain: len_flat_strain +
    len_flat_force]
565             num_structs = len(strain)
566             strain = tf.reshape(strain, [num_structs, STRAIN_VEC_COUNT,
    STRAIN_SPACE_VECTOR_LENGTH])
567             rotation = strain_force[0:, len_flat_strain +
    len_flat_force:]
568             rotation = tf.reshape(rotation, [num_structs,
    STRAIN_VEC_COUNT, SPACE_DIMENSION, SPACE_DIMENSION])
569             tensor_2 = keras.backend.reshape(tensor, [num_structs,
    SPACE_DIMENSION, SPACE_DIMENSION * NUM_COORD_ENV])
570             tensor_3 = tf.expand_dims(tensor_2, axis=1)
571             tensor_3 = tf.repeat(tensor_3, STRAIN_VEC_COUNT, axis=1)
572             y_guess = tf.linalg.matvec(tensor_3, strain)
573             rot_force = tf.linalg.matvec(rotation, y_guess)
574             sum_rot_force = keras.backend.sum(rot_force, axis=1,
    keepdims=False)
575             losses = keras.backend.square(force - sum_rot_force)
576             loss = keras.backend.mean(losses, axis=0)
577             loss = keras.backend.sum(loss, axis=0)
578             return loss
579
580             print("Training␣Neural␣Network␣based␣upon␣Tensor␣size")
581             # define the keras model using leaky relu
582
583             n = 1
584             m = 1
585
586             model = Sequential()
587             model.add(Dense((n*STRAIN_SPACE_INPUT_LENGTH),
    input_dim=(STRAIN_SPACE_INPUT_LENGTH)))
588             model.add(LeakyReLU(alpha=alpha))
589             model.add(Dropout(dropout))
590             model.add(Dense((m * NUM_COORD_ENV * SPACE_DIMENSION *
    SPACE_DIMENSION)))
591             model.add(LeakyReLU(alpha=alpha))
592             model.add(Dropout(dropout))
593             model.add(Dense((NUM_COORD_ENV * SPACE_DIMENSION *
    SPACE_DIMENSION)))
594             model.add(LeakyReLU(alpha=alpha))
595
596             #Use constant learning rate
597             optimizer =
    keras.optimizers.Adam(learning_rate=initial_learning_rate,
    epsilon=0.00000001)
598             # optimizer =
    keras.optimizers.Adamax(learning_rate=initial_learning_rate,
    epsilon=0.0000000001)
599             # optimizer =
    keras.optimizers.Adamax(learning_rate=lr_schedule, epsilon=0.0000000001)
600             # optimizer =
    keras.optimizers.Adam(learning_rate=lr_schedule)
601             # optimizer2 =
    keras.optimizers.Adam(learning_rate=initial_learning_rate)
```

```
602             # optimizer3 =
    keras.optimizers.Adam(learning_rate=initial_learning_rate)
603             optimizer2 =
    keras.optimizers.Adamax(learning_rate=second_learning_rate, epsilon =
    0.000000000001)
604             optimizer3 =
    keras.optimizers.Adamax(learning_rate=tertiary_learning_rate, epsilon =
    0.000000000001)
605             # optimizer2 =
    keras.optimizers.Adamax(learning_rate=lr_schedule, epsilon =
    0.000000000001)
606             # optimizer2 =
    keras.optimizers.Adam(learning_rate=lr_schedule, epsilon = 0.00000000001)
607             # optimizer =
    keras.optimizers.Adagrad(learning_rate=initial_learning_rate,
    initial_accumulator_value=0.1, epsilon=1e-07, name="Adagrad")
608             # optimizer2 =
    keras.optimizers.Adagrad(learning_rate=lr_schedule,
    initial_accumulator_value=0.9, epsilon=1e-07, name="Adagrad")
609             # optimizer =
    tf.keras.optimizers.Nadam(learning_rate=initial_learning_rate,
    beta_1=0.9, beta_2=0.999, epsilon=1e-09, name="Nadam")
610             # optimizer2 =
    tf.keras.optimizers.Nadam(learning_rate=initial_learning_rate,
    beta_1=0.9, beta_2=0.999, epsilon=1e-09, name="Nadam")
611             # optimizer3 =
    tf.keras.optimizers.Nadam(learning_rate=initial_learning_rate,
    beta_1=0.9, beta_2=0.999, epsilon=1e-09, name="Nadam")
612             # optimizer2 =
    tf.keras.optimizers.SGD(learning_rate=initial_learning_rate,
    momentum=0.01, nesterov=False, name="SGD")
613             # optimizer2 =
    tf.keras.optimizers.SGD(learning_rate=lr_schedule, momentum=0.9,
    nesterov=True, name="SGD")
614             # optimizer3 =
    tf.keras.optimizers.SGD(learning_rate=initial_learning_rate,
    momentum=0.8, nesterov=False, name="SGD")
615
616             #Or use exponentially decreasing learning rate
617             #optimizer = keras.optimizers.Adam(learning_rate=lr_schedule)
618
619             class new_callback(tf.keras.callbacks.Callback):
620             def on_epoch_end(self, epoch, logs={}):
621             if(logs.get('loss')< 0.00000000000001): # select the accuracy
622             print("\n!!!Loss is low enough, no further training!!!")
623             self.model.stop_training = True
624
625             callback_1 = new_callback()
626
627             second_model = model;
628             tertiary_model = model;
629
630             # compile the keras model
631             model.compile(loss=custom_loss_function,
    optimizer=optimizer, metrics=['accuracy'])
632
633
```

```
634
635             # fit the keras model on the dataset
636             history = model.fit(X, Y, epochs=epochs_1,
    batch_size=batch_size_1, shuffle=True)
637
638             # print(history.history['loss'][-1])
639
640             old_weights = model.get_weights()
641
642             second_model.compile(loss=custom_loss_function,
    optimizer=optimizer2, metrics=['accuracy'])
643
644             second_model.set_weights(old_weights)
645
646
647             def lr_schedule_e(epoch, lr):
648             if epoch < 1000:
649             return lr
650             else:
651             return lr / epoch
652             # return lr * tf.math.exp(-0.1)
653
654             lr_callback =
    tf.keras.callbacks.LearningRateScheduler(lr_schedule_e)
655
656
657             history2 = second_model.fit(X, Y, epochs=epochs_2,
    batch_size=batch_size_2, shuffle=True, callbacks=[callback_1])
658
659             old_weights = second_model.get_weights()
660
661
662             tertiary_model.compile(loss=custom_loss_function,
    optimizer=optimizer3, metrics=['accuracy'])
663
664             tertiary_model.set_weights(old_weights)
665
666             history3 = tertiary_model.fit(X, Y, epochs=epochs_3,
    batch_size=batch_size_3, shuffle=True, callbacks=[callback_1])
667
668             # Run the final version of the model against each piece of
    data
669             predictions = tertiary_model.predict(X)
670
671             # print(predictions)
672             #Take the mean of those final values
673             tensor_predicted = tf.reduce_mean(predictions, axis=0)
674
675             #Shape the values into a tensor
676             tensor_2 = keras.backend.reshape(tensor_predicted,
    [SPACE_DIMENSION, NUM_COORD_ENV * SPACE_DIMENSION])
677
678             #Output the raw tensor
679             print(tensor_2)
680
681
```

Python Code Snippet A.1: Artificial Neural Network Structure